# UNIVERSITY OF SOUTHAMPTON

FACULTY OF NATURAL AND ENVIROMENTAL SCIENCES

SCHOOL OF OCEAN AND EARTH SCIENCE


**An Annual Cycle of Open-Ocean Submesoscale Dynamics in the Northeast Atlantic from Observations**

by


**Xiaolong Yu**


Thesis for the degree of Doctor of Philosophy

January 2018

**UNIVERSITY OF SOUTHAMPTON**

# ABSTRACT

FACULTY OF NATURAL AND ENVIRONMENTAL SCIENCES

SCHOOL OF OCEAN AND EARTH SCIENCE

Doctor of Philosophy

AN ANNUAL CYCLE OF OPEN-OCEAN SUBMESOSCALE DYNAMICS IN THE NORTHEAST ATLANTIC FROM OBSERVATIONS

by Xiaolong Yu

This thesis presents an investigation of the annual cycle of the submesoscale dynamics from two nested clusters of meso- and submesoscale-resolving moorings, deployed in a typical mid-ocean area of the Northeast Atlantic. Vertical velocities inferred using the non-diffusive density equation are substantially stronger at submesoscales (horizontal scales of 1-10 km) than at mesoscales (horizontal scales of 10-100 km). Submesoscale vertical flows are found to drive significant upper-ocean restratificaiton in response to the enhancement of submesoscale lateral fronts in the presence of intense mesoscale frontogenesis, indicating that mesoscale frontogenesis is a regular precursor of the submesoscale turbulence in the study region. The integrated upper-ocean restratification induced by submesoscale flows over the annual cycle is comparable in magnitude to the net destratification driven by local atmospheric cooling. Further investigation of the upper-ocean potential vorticity budget and its relationship to the occurrence of submesoscale frontal instabilities reveals that wind forcing of fronts is centrally involved in symmetric and gravitational instabilities. In spite of persistent atmospheric cooling during wintertime, conditions favorable to symmetric instability are often observed when surface winds have a downfront (i.e., oriented in the direction of the geostrophic shear) component. The forced symmetric instability is dominant in the part of the mixed layer where potential vorticity takes the opposite sign to the Coriolis parameter, below a near-surface convective layer where gravitational instability dominates. Another common outcome of the interaction between winds and mixed-layer currents is the occurrence of near-inertial waves. The annual cycle of downward propagation of wind-generated near-inertial waves is examined from the

mooring observations and a mixed-layer slab model. Near-inertial kinetic energy is found to dominate the internal wave band, and to radiate predominantly downward in a few strong resonant wind events throughout the year. Near-inertial waves are mostly enhanced during wintertime when submesoscale flows are also active, suggesting that these energetic waves may interact with submesoscale fronts and lead to elevated dissipation.

# Contents

# List of Tables

# List of Figures

# DECLARATION OF AUTHORSHIP

I, Xiaolong Yu, declare that this thesis entitled ‘An Annual Cycle of Open-Ocean Submesoscale Dynamics in the Northeast Atlantic from Observations” and the work presented in the thesis are both my own, and have been generated by me as the result of my own original research. I confirm that:

- This work was done wholly or mainly while in candidature for a research degree at this University.

- Where any part of this thesis has previously been submitted for a degree or any other qualification at this University or any other institution, this has been clearly stated.

- Where I have consulted the published work of others, this is always clearly attributed.

- Where I have quoted from the work of others, the source is always given. With the exception of such quotations, this thesis is entirely my own work.

- I have acknowledged all main sources of help.

- Where the thesis is based on work done by myself jointly with others, I have made clear exactly what was done by others and what I have contributed myself.

- None of this work has been published before submission.

Signed: ……..

Date:…….

# Acknowledgements

First and foremost, I would like to thank my wonderful supervisors, Alberto Naveira-Garabato and Adrian Martin, for their inspiration, enthusiasm and positive attitude through the four-year period of my PhD research. I am very grateful to Alberto for introducing me to this research field, and for continuously supporting me for scientific conferences around the world and a fantastic research cruise experience in the Southern Ocean. I thank Adrian for being very thoughtful in my scientific education, and for many suggestions to my research career. Without their guidance and support, this thesis would not have been possible.

I would also like to thank a number of people who had helped me along the way. Special thanks are due to Christian Buckingham and Liam Brannigan for so many long and sometimes late/remote meetings and discussions. I thank Andrew Thompson, Gillian Damerell, Dafydd Gwyn Evans, Victoria Hemsley, Jeff Polton and Alexander Forryan for sharing their work with me and the associated scientific discussions. Thank you to Anna Rumyantseva who has been great company during my first scientific meeting in Bangor. Thanks also to Jesse Cusack for insightful discussions on ocean mixing, and more importantly for his friendship.

I am grateful to Katsia Pabortsava for helping me and giving me suggestions at various stages of my PhD study, and for countless basketball nights of course. Thank you also for providing entertainment to my father at Mayflower Park.

I want to give my thanks to my office mates too: Konstantina Rizopoulou, Rafael Jaume Catany, Daniela Vendettuoli, Elena Cerdán, Ryan Gallacher, and Colette Couves, for their encouragement and friendship.

Huge thanks to all my Chinese friends at NOCS, my PhD would not have been as enjoyable without you, especially Zongpei Jiang, Pin-ru Huang (Taiwan), Chongyuan Mao, Ming-Tsung Chung (Taiwan), Chuang Xuan, Yuxi Jin, Xiangbo Feng, Kuidong Zhao, Gaowei Hu, Tianya Yin, Xiaodong Yang, Chen Chen, Yingxu Wu, Shenjie Zhou, Yunyi Li. Special thanks to Pin-ru and Ming-Tsung for their company when I visited Taiwan for a holiday.

Being sports a fun motivation and a stress-relief hobby for me, I would like to thank the basketball community at Highfield Campus, including everyone who has ever played with me and/or come along to my gym sessions. These workouts helped me

release my energy, have some fun meeting new people and enjoy my life as a PhD student.

My parents, Xueping Yu and Liping Chu, thank you for their continued support and understanding. I can still remember when my father told me my birthday is the most important day of the year for him, that means a lot to me. I feel very sorry that I could not spend any Chinese New Year with them during my PhD study. To them, I owe so much.

Above all others, I would like to express my special thanks to my girlfriend, Lu Wang, for her love and self-sacrifice, and for always being there for me.

# Abbreviations

| | |
|---|---|
| ACM: | **A**coustic **C**urrent **M**eter |
| ADCP: | **A**coustic **D**oppler **C**urrent **P**rofiler |
| APE: | **A**vailable **P**otential **E**nergy |
| BCI: | **B**aro**C**linic **I**nstability |
| CCW: | **C**ounter-**C**lock**W**ise |
| CI: | **C**entrifugal **I**nstability |
| CLD: | **C**onvective **L**ayer **D**epth |
| CTD: | **C**onductivity-**T**emperature-**D**epth |
| CW: | **C**lock**W**ise |
| EBF: | **E**kman **B**uoyancy **F**lux |
| ECMWF: | **E**uropean **C**entre for **M**edium-range **W**eather **F**orecasts |
| EKE: | **E**ddy **K**inetic **E**nergy |
| GI: | **G**ravitational **I**nstability |
| KE: | **K**inetic **E**nergy |
| KPP: | **K**-**P**rofile **P**arameterization |
| ML: | **M**ixed **L**ayer |
| MLD: | **M**ixed **L**ayer **D**epth |
| NEMO: | **N**ucleus for **E**uropean **M**odelling of the **O**cean |
| NERC: | **N**atural **E**nvironment **R**esearch **C**ouncil |
| NIWs: | **N**ear-**I**nertial **W**aves |
| NOCS: | **N**ational **O**ceanography **C**entre, **S**outhampton |
| MODIS: | **MOD**erate resolution **I**maging **S**pectroradiometer |
| OSBL: | **O**cean **S**urface **B**oundary **L**ayer |
| OSMOSIS: | **O**cean **S**urface **M**ixing, **O**cean **S**ubmesoscale **I**nteraction **S**tudy |
| PAP: | **P**orcupine **A**byssal **P**lain |
| PDF: | **P**robability **D**istribution **F**unction |
| PSI: | **P**arametric **S**ubharmonic **I**nstability |
| PV: | **P**otential **V**orticity |
| PWP: | **P**rice-**W**eller-**P**inkel |
| QG: | **Q**uasi-**G**eostrophic |
| RMS: | **R**oot **M**ean **S**quare |

| | |
|---|---|
| SBF: | **S**urface **B**uoyancy **F**lux |
| SI: | **S**ymmetric **I**nstability |
| SLA: | **S**ea **L**evel **A**nomaly |
| SSH: | **S**ea **S**urface **H**eight |
| SWOT: | **S**urface **W**ater and **O**cean **T**opography |
| TKE: | **T**urbulent **K**inetic **E**nergy |
| WKB: | **W**entzel-**K**ramers-**B**rillouin |

# Symbols

| | |
|---|---|
| $g$ | gravity |
| $\rho$ | potential density |
| $f$ | Coriolis coefficient |
| $\zeta$ | relative vorticity |
| $\alpha$ | thermal expansion coefficient |
| $\beta$ | haline contraction coefficient |
| $b$ | buoyancy |
| $\tau$ | surface wind stress |
| $q$ | potential vorticity |
| $h$ | convective layer depth |
| $H$ | mixed layer depth |
| $\mathcal{H}$ | vertical scale of the main pycnocline |
| $Q$ | equivalent heat flux |
| $U$ | current speed |
| $F$ | frictional body force |
| $\Omega$ | Earth's angular velocity |
| $\phi$ | latitude |
| $Fs$ | frontogenesis function |
| $N^2$ | buoyancy frequency |
| $C_p$ | specific heat |
| $Q_{\mathrm{net}}$ | air&sea heat flux |
| $\delta_e$ | Ekman layer depth |
| $\phi_{Ri_B}$ | balanced Richardson number angle |
| $\phi_C$ | critical angle |
| $KE_{in}$ | near-inertial kinetic energy |
| $\Pi_{wind}$ | wind work |
| $Z_{in}$ | inertial velocity (complex format) |
| $\omega_h$ | horizontal component of vorticity |
| $R_1$ | local first baroclinic Rossby radius |
| $R_{ML}$ | mixed layer deformation radius |

| | |
|---|---|
| $B_0$ | Surface buoyancy flux |
| $B_e$ | Ekman buoyancy flux |
| $J_z^D$ | diabatic PV flux |
| $J_z^F$ | frictional PV flux |

For a better man.

# Chapter 1: Introduction

This Chapter begins with a research background of submesoscale processes in the ocean surface boundary layer, followed by a review of the upper-ocean submesoscale dynamics, including general characterization of submesoscale processes, submesoscale vertical motions and the associated restratification, and symmetric instability. Wind-generated near-inertial waves are also introduced. The objectives and outline of this thesis are described at the end of this Chapter.

## 1.1 Research background

The ocean surface boundary layer (OSBL) is a fundamental component of the global climate system, and plays a critical role in mediating the vertical exchange of both physical and biogeochemical tracers such as heat, momentum, and carbon dioxide between the atmospheric and the ocean interior. A broad definition of the OSBL is a layer with active turbulent mixing in the upper ocean. The OSBL is a turbulent environment accommodating a wide range of scales from millimetres to over 1000 km, and so its evolution can be affected by a vast range of behaviours and interactions via many different mechanisms (e.g., Gerbi et al. 2009; Taylor and Ferrari 2010; Badin et al. 2011; Belcher et al. 2012; Alford et al. 2015; Pearson et al. 2015; Thomas et al. 2016). Simply put, the OSBL deepens in response to atmospheric cooling, destabilizing wind and surface wave forcing, which produce small-scale three-dimensional turbulence that entrains dense water, deepening the layer. The OSBL shoals in response to solar heating and to meso- and submesoscale processes that transform lateral buoyancy gradients into vertical stratification, restratifying the layer. Therefore, an accurate and detailed understanding of the key physical features and processes within the OSBL is of essential importance to understand how the ocean and atmosphere interact and influence the climate system.

The evolution of the OSBL has significant ramifications for a variety of climate, weather and biogeochemical phenomena (Ferrari 2011). For decades, great efforts have been made by oceanographers and climatologists for improving the physical parameterizations and reducing systematic errors in climate models (e.g., Large et al. 1997; Pope et al. 1999; Murphy et al. 2004). Nevertheless, global-scale numerical models are still limited by computational restrictions, incomplete representation of fine-scale turbulent processes, and boundary condition errors. Oceanic submesoscale flows, a relatively unexplored transition from marginal rotational control to non-rotating dynamics and from stratified anisotropy to three-dimensional isotropy (McWilliams 2008), have come into focus in recent years but are not currently recognized in parameterization schemes for most of the climate models. Currently, ocean models used for climate studies are based on grids that are coarser than the typical horizontal scales of submesoscale flows because of computer speed limitations. The missing parameterization of submesoscale processes might be the main reason for big errors in mixed layer depth (MLD) estimation in global-scale climate models, especially in the Southern Ocean (Sallée et al. 2013). We need to develop a better understanding of the

submesoscale dynamics in a wide range of circumstances in order to improve weather and climate predictions.

Submesoscale processes are ubiquitous features of the OSBL and dynamically important. Submesoscale processes have been shown, both through numerical simulations and *in situ* observations, to have an important contribution to vertical transport of buoyancy and nutrients (Taylor and Ferrari 2011; Lévy and Martin 2013; Smith et al. 2016), and to transfer energy downscale from mesoscale eddies to small-scale turbulence (D'Asaro et al. 2011; Thomas et al. 2016; Qiu et al. 2017). The generation of submesoscale structures and their associated effects have been extensively documented in regions of strong fronts with persistent atmospheric forcing such as the Gulf Stream, the Kuroshio and the Antarctic Circumpolar Current. In contrast, submesoscale dynamics in the open ocean region remains relatively understudied. This thesis is an effort to expand our understanding of the upper-ocean submesoscale dynamics in the open ocean region.

This Chapter presents a review of recent theoretical, numerical and observational research of the upper-ocean submesoscale processes. It is worth noting that submesoscale processes can also be generated at the ocean bottom boundary layer, but my focus is on the dynamics of submesoscale flows in the upper ocean. Therefore, the literature on submesoscale dynamics influenced or generated by the bottom topography and the associated elevated local dissipation and mixing (e.g., McWilliams 1985; Gula et al. 2015; Rosso et al. 2015; Gula et al. 2016) will not be reviewed here.

## 1.2 Submesoscale dynamics in the upper ocean

### 1.2.1 Upper-ocean submesoscale processes

The oceanic submesoscale processes have recently become a hot topic in the physical oceanographic research, and their diagnoses are facilitated through advances in high-resolution modeling, *in situ* and remotely sensed observations. Surface chlorophyll inferred from NASA's MODIS satellite provides a direct evidence of the common occurrence of submesoscale filaments and fronts at the ocean surface (Figure 1.1). The large chlorophyll concentrations are mostly localized at the mesoscale fronts and eddies on scales ranging from 10-100 km, particularly in the range of 60-62°E, where the mesoscale fronts and eddies exhibit many fine-scale (i.e., a few kilometers) bends and wrinkles. The satellite-observed elevated chlorophyll concentrations at the submesoscale range are reproduced by numerical simulations from Taylor and Ferrari

(2011), which reveal that phytoplankton blooms are triggered by submesoscale upwelling and restratification at fronts.

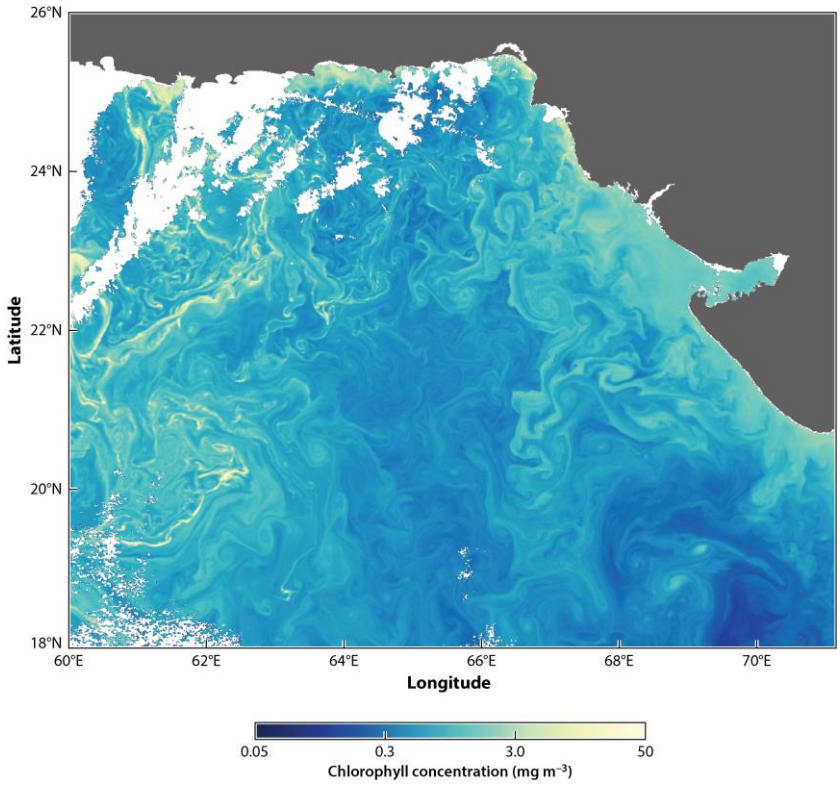


Figure 1.1: Sea surface chlorophyll concentration in the Arabian Sea as viewed by the Moderate Resolution Imaging Spectroradiometer (MODIS) from NASA's Aqua satellite on February 22, 2005. The approximate resolution of the data is 1 km. White spaces are where data were flagged or missing because of cloud cover. Figure from Mahadevan (2016).

Mesoscale eddies in the ocean are generated by barotropic and baroclinic instabilities from the mean flows, with spatial scales of 10-100 km and temporal scales of a few days to several months (Wyrtki et al. 1976; Chelton et al. 1998). In the traditional view of mesoscale eddies, it has been assumed that the basic cross-frontal momentum balance is geostrophic, meaning that the cross-front pressure gradients are in balance with Coriolis force associated with the along-front velocity.

In comparison with mesoscale eddies, submesoscale processes arise at smaller spatial scales (1-10 km) and have shorter temporal scales (several hours to several days). More dynamically, submesoscale flows are characterized by the Rossby number $Ro = U/fL$ and bulk Richardson number $Ri = N^2H^2/U^2$ on the order of O(1) (Thomas et al. 2008), where $U$ is a characteristic velocity, $L$ is a characteristic length scale, $H$ is a

characteristic vertical scale, and $N$ and $f$ are the buoyancy and inertial frequencies. Submesoscale processes are more preferentially generated in the mixed layer, where the vertical stratification is weak, and usually occur in the vicinity of mesoscale eddies, through nonlinear interaction between mesoscale eddies and stirring of the mesoscale currents (Capet et al. 2008b; Ferrari and Wunsch 2009).

In order for the ocean to achieve a state of statistical equilibrium, a dynamical route to dissipation is required. The winds are the main energy source for the general circulations of the ocean, and then the associated available potential energy (APE) and kinetic energy (KE) are largely transferred to mesoscale eddies through hydrodynamic instabilities. However, KE contained in the mesoscale eddies primarily undergo an inverse energy cascade because turbulence on the mesoscale is strongly constrained by the Earth's rotation (Charney 1971). In this scenario, other direct routes to dissipation are needed for energy budget in equilibrium in the ocean. Recent studies suggest submesoscale overturning instabilities are key to bridging the gap between mesoscale eddies which are known as a massive reserve of KE and APE of the ocean and small scales where energy can be dissipated due to viscous effects (Capet et al. 2008c; McWilliams 2008; Molemaker et al. 2010; Zhang et al. 2016). One direct route is that submesoscale fronts with large Rossby number lead to the breakdown of quasi-geostrophy and allow unbalanced motions emerge. These unbalanced motions are essential to the forward energy cascade *en route* to dissipation (Molemaker et al. 2010).

### 1.2.2 Seasonal cycle of submesoscale flows

The investigation of the seasonal cycle of submesoscale flows has been found particularly useful to understand the relevant mechanisms that energize submesoscale flows and the involved energy pathways in the OSBL. Mesoscale-driven frontogenesis and mixed-layer baroclinic instability (BCI) are proposed as the two main mechanisms.

The formation of fronts is driven by frontogenetic processes. Frontogenesis develops near the ocean surface, where the absence of vertical velocities allows straining from mesoscale eddies to increase density variance, therefore leading to a very effective sharpening of existing density fronts (Hoskins and Bretherton 1972; Hoskins 1982). Frontogenesis can be forced by either mesoscale straining deformation (e.g., Lapeyre et al. 2006) or by vertical momentum mixing (e.g., McWilliams et al. 2015).

Mixed-layer BCI, which is mostly balanced in geostrophy (Stone 1966; Stone 1970), usually accelerates the slumping of fronts with large vertical velocities and effective

restratification processes through the release of APE by an eddy-driven overturning circulation (Boccaletti et al. 2007; Fox-Kemper et al. 2008). Thereby, mixed-layer BCI is expected to vary seasonally, because MLD and the associated mixed-layer potential energy usually undergo a strong seasonal cycle. The vertical and horizontal scales and growth rates of baroclinically unstable mixed-layer modes are similar to those of submesoscale processes (Boccaletti et al. 2007).

Sasaki et al. (2014) demonstrate a strong seasonality of submesoscales in the North Pacific Ocean through a 2-year analysis of a high-resolution realistic simulation, with winter being much more energetic than summer (Figure 1.2). Mixed-layer BCI is highlighted as the dominant mechanism in energizing submesoscale flows in the wintertime when the mixed layer is deep and vertical mixing is vigorous. They also suggest an energy pathway involving the transformation of APE into KE enhanced at submesoscales and an inverse KE cascade from the submesoscale towards larger scales. These results indicate that the KE produced by mixed-layer BCI might be an energy source for mesoscale eddies.

Callies et al. (2015) further provide observational evidence that the seasonal cycle of submesoscale energy levels is consistent with the mixed-layer BCI mechanism. The observed submesoscale flow is to leading order in geostrophic balance, suggestive of the inverse cascade of KE. They also conclude that mesoscale-driven frontogenesis appears to be weak in the western subtropical North Atlantic as the submesoscale spectra roll off like $k^{-3}$ (with $k$ as the along-track wavenumber) in summer, which is consistent with interior QG turbulence. Similar seasonally varying behaviors of submesoscale frontal dynamics have also been observed in the Kuroshio region (Qiu et al. 2017), where the balanced eddy variability is controlled by combined interior QG dynamics and mixed-layer BCI in winter, and interior QG dynamics alone in summer. du Plessis et al. (2017) also highlight the importance of submesoscale mixed-layered eddies enhancing seasonal restratification and mixing using glider data in the Subantarctic Zone of the Southern Ocean, where winter mixed layers can reach as deep as 500 m.

Apart from the strong seasonal cycle of submesoscale fronts attributed to mixed-layer BCI set by atmospheric forcing, Rocha et al. (2016) point out that submesoscale inertia-gravity waves are strongly modulated by the seasonally changing upper-ocean stratification, and undergo a near-surface seasonal cycle in the vicinity of the Kuroshio Extension region.

The aforementioned studies have focused on strong frontal regions that are characterized by strong surface forcing and interior potential vorticity (PV) gradients reversing sign at depth, while in other regions, where surface forcing is more intermittent and deep PV gradients weaker, mesoscale-driven frontogenesis may play a major role in generating submesoscale turbulence in the upper ocean (Roullet et al. 2012).

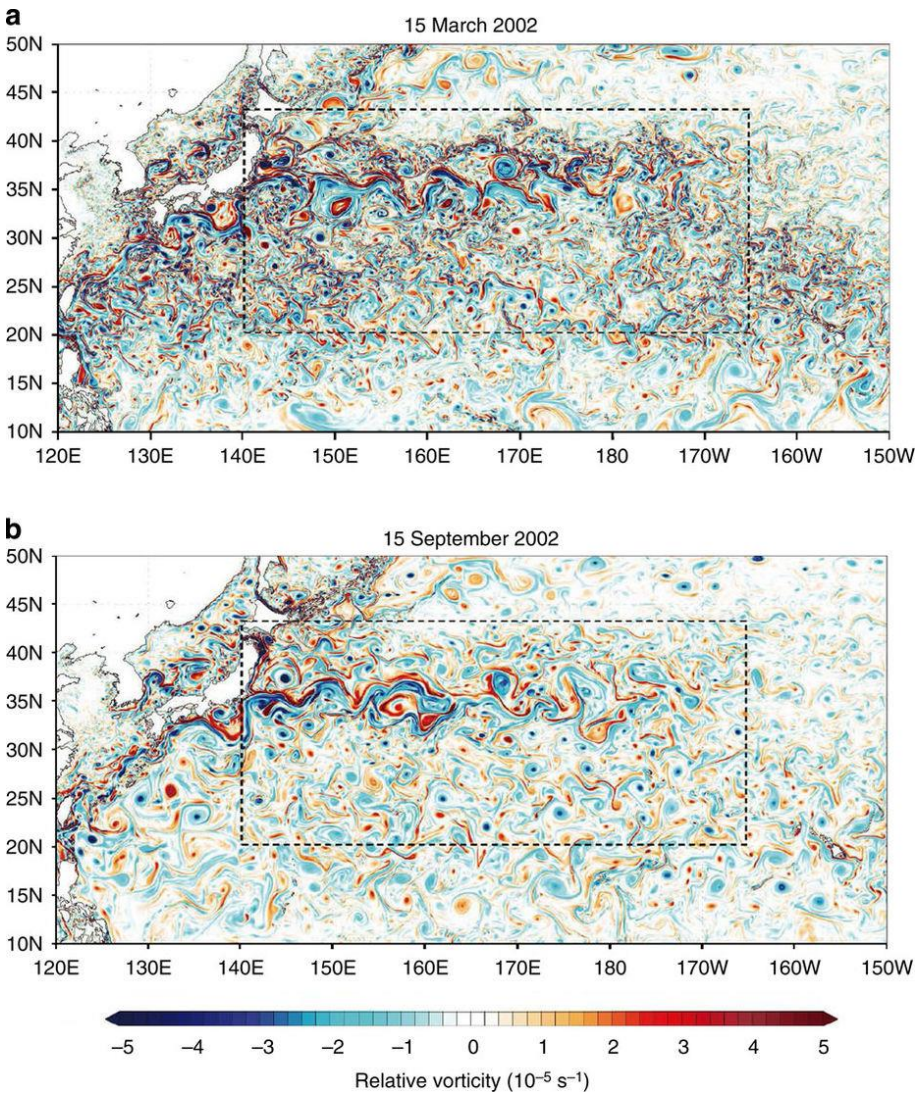


Figure 1.2: Surface relative vorticity in the Northwestern Pacific from a high-resolution (1/30º in the horizontal and 100 vertical levels) hindcast simulation using the Ocean General Circulation Model. (a) On 15 March and (b) on 15 September in 2002. Figure from Sasaki et al. (2014).

### 1.2.3 Enhanced vertical velocity and restratification at submesoscale fronts

It has long been recognized that vertical flow plays an important role in the ocean circulation, and a variety of processes acting on different spatial scales can drive

vertical flow in the ocean (Wang 1993; Martin and Richards 2001; McGillicuddy et al. 2007; Frajka-Williams et al. 2011; Mazzini and Barth 2013; Thomas et al. 2013; Gaube et al. 2015).

Mesoscale eddies were previously considered to be exclusively responsible for the exchange of properties and tracers between the upper ocean and the ocean interior with typical vertical velocity on the order of 1 to 10 m/day (Rudnick 1996; McGillicuddy et al. 2007; Chelton et al. 2011; Pascual et al. 2015). However, more recent studies reveal that submesoscale effects are particularly effective at inducing intense vertical velocities in the OSBL, and the strength of the submesoscale vertical velocity is typically larger than mesoscale processes by one order of magnitude (Mahadevan and Tandon 2006; Capet et al. 2008b; Zhong and Bracco 2013; Rosso et al. 2014).

Submesoscale fronts can induce ageostrophic overturning circulation via surface frontogenesis in the absence of mixed-layer BCI, and one typically observes is downwelling (upwelling) on the dense (light) side of fronts with a restratifying horizontal flow (Lapeyre et al. 2006). In addition to forcing by frontogenesis, vertical flows associated with submesoscale processes can also be generated by forced instabilities. For example, surface cooling can intensify submesoscale motion by triggering symmetric instability (SI) of fronts and enhancing frontal vertical circulation (Yoshikawa et al. 2001). Amplified frontogenetic strain combined with the cooling-induced low PV in the mixed layer enhances the strength of the frontal vertical circulation. Furthermore, due to the opposite relative vorticity in an eddy interior compared to the periphery of an eddy, intense vertical velocities of 10-100 m/day may be induced along the eddy periphery by non-linear Ekman transport (Mahadevan et al. 2008).

Mahadevan (2006) and Mahadevan and Tandon (2006) using numerical simulations show that wind plays a critical role in inducing submesoscale structure and large vertical motion. They find that the instantaneous vertical velocity structure is very sensitive to grid resolution, and both hydrostatic and non-hydrostatic numerical models can resolve submesoscale dynamics well. Rosso et al. (2014) compare and contrast a pair of regional numerical experiments, and demonstrate that an increase in horizontal resolution from mesoscale-resolving (1/20º) to submesoscale-resolving (1/80º) leads to dramatically higher vertical velocities at submesoscale filamentary frontal structures (Figure 1.3). The enhanced vertical velocity by an increase of horizontal resolution is also illustrated by other numerical studies (Capet et al. 2008b; Lévy et al. 2012).

Observationally, Adams et al. (2017) developed a mathematical framework to estimate vertical velocity at the submesoscale O (1-10 km) from co-located drifter and horizontal water velocity time series, and upwelling or downwelling rates of O (100 m/day) are found in the Scotia Sea.

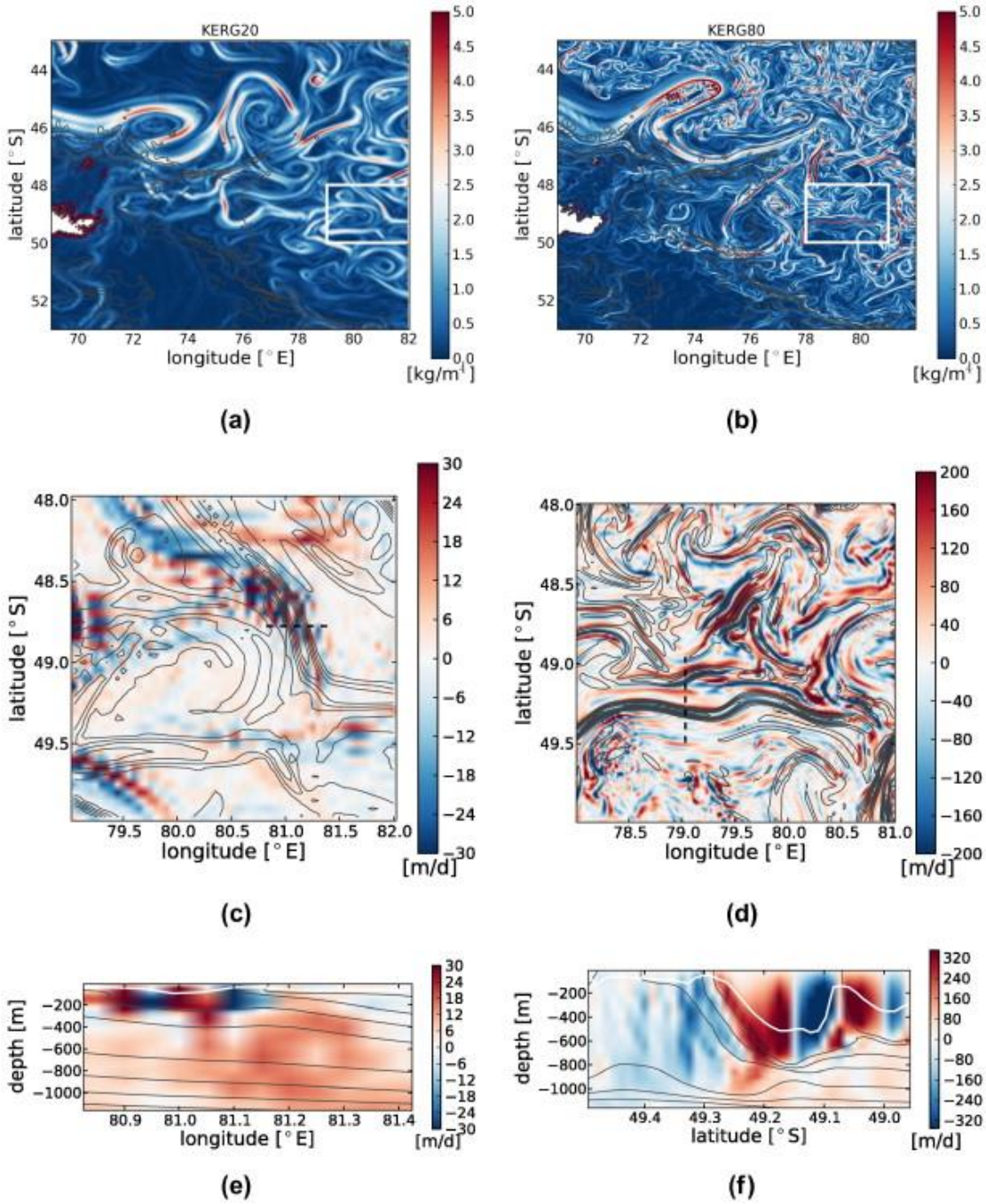


Figure 1.3: Frontal structures at 50 m depth, for KERG20 (horizontal resolution 1/20º) and KERG80 (horizontal resolution 1/80º) cases. (a) and (b) $|\nabla_H \rho|$( kg/m$^4$) and in black the topography contours for the first 3000 m, with an interval of 600 m. (c) and (d) $w(x, y)$ for the subdomains indicated by the white boxes in (a) and (b). In (c) and

(d) contours represent $|\nabla_H \rho|$ with an interval of 1 $\times 10^{-5}$ kg/m$^4$ and the dashed black lines indicate the location of the vertical slices of $w(x,z)$ (e) and $w(y,z)$ (f). White lines in (e) and (f) indicate the mixed layer depths, while grey lines are isopycnals, with an interval of 0.1 kg/m$^3$. Figure from Rosso et al. (2014).

### 1.2.4 Symmetric instability

The generation of SI must satisfy the conditions that Ertel PV $q$ has the opposite sign to the local Coriolis parameter $f$ (Hoskins 1974). It is worth noting that Hoskins (1974) used a different definition of SI, which refers to any instabilities that arise when $fq < 0$, and so also include gravitational instability (GI) and centrifugal instability (CI). In this thesis, SI is defined as the growing perturbations of a flow that are independent of the along-front direction. The energy source for SI is the mean KE from the geostrophic shear (Thomas et al. 2013). In essence, it is the strong baroclinicity in the weakly stratified fluid driving its Ertel PV to take the opposite sign of the Coriolis parameter that is its defining feature.

Hence, the generation of SI relies on the formation of sharp fronts and the creation of low-PV waters. A critical constraint of the material invariance of PV is the impermeability theorem (Haynes and Mcintyre 1987), under which the sources of PV are only through boundaries by interactions with the surface forcing or bottom topography. Therefore, destabilizing atmospheric forcing, such as surface cooling and downfront winds, is needed to generate SI in a stable flow and rotating system. In particular, downfront winds (i.e., oriented in the direction of the geostrophic shear) can induce Ekman transport that moves dense water towards the light side of a front (Thomas and Lee 2005). This process reduces the stratification of a surface layer, and makes the front susceptible to SI (Figure 1.4).

SI is a shear instability and can draw KE from the geostrophic currents (Bennetts and Hoskins 1979; Thomas and Taylor 2010). The influence of the baroclinicity (i.e., a horizontal buoyancy gradient) on convection near the ocean surface forced by either a surface buoyancy loss or a downfront wind stress is examined by Taylor and Ferrari (2010). They propose two distinct dynamical layers of slantwise convection in the OSBL based on the relative dominant source of turbulent kinetic energy (TKE): near the surface a convective layer with buoyancy flux as the dominant source while the layer below that with geostrophic shear production as the dominant source.

SI provides an energy pathway for balanced flows downscale to turbulence (Taylor

and Ferrari 2009; D'Asaro et al. 2011; Thomas et al. 2016). While geostrophic flows might be fueled by mixed-layer BCI in the wintertime, SI extracts KE from baroclinic, geostrophic currents, and transfers KE to small-scale turbulence through a secondary Kelvin-Helmholtz shear instability and ultimately dissipated at small scales (Taylor and Ferrari 2009).

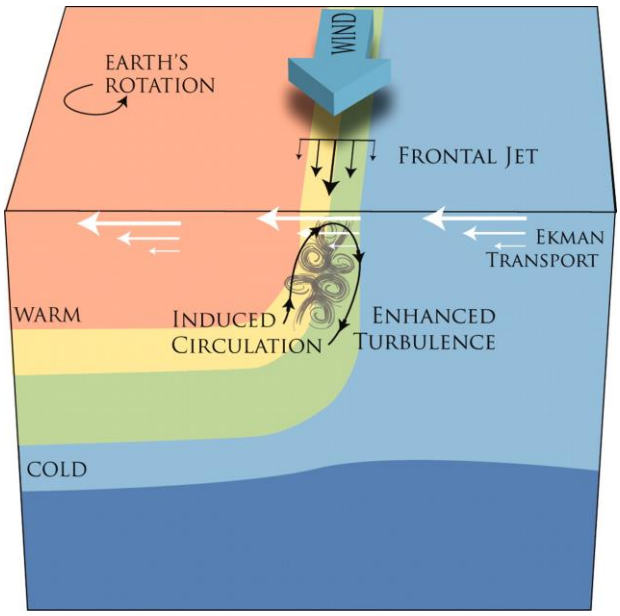


Figure 1.4: Structure of the symmetrically unstable front. A wind blowing down the frontal boundary between warm and cold water induces an Ekman transport perpendicular to the wind and to the front. This carries heavy water from the cold side of the front over light water from the warm side, which, in the presence of the frontal jet and lateral density gradient, acts to reduce the stratification near the surface and makes the front unstable to SI. The instability draws energy from the frontal jet, leading to enhanced turbulence, and induces a circulation acting to bring warm water to the surface and cold water to depth, thus counteracting the effect of the Ekman transport and keeping the near-surface stably stratified, with warm water over cold water. Figure from D'Asaro et al. (2011).

### 1.2.5 Near-inertial waves

The dynamic complexity of the OSBL makes it particularly difficult to isolate the effects by submesoscales. Near-inertial waves (NIWs) largely intersect with the time scales of submesoscales in the mid-ocean, but the propagation dynamics of NIWs are different from the more advective dynamics of submesoscale currents.

NIWs are oscillatory, unbalanced motions with frequencies close to the local inertial frequency, and are ubiquitous in the ocean. In the western boundary current regions,

energetic frontal flows interact significantly with NIWs due to strong geostrophic vorticity (Mooers 1975; Kunze 1985; Young and Ben Jelloul 1997; Whitt and Thomas 2015). Enhanced turbulent mixing and elevated internal wave energy are often seen in these areas via energy loss from balanced to unbalanced flows (Polzin 2010; Alford et al. 2013). Furthermore, near-inertial motions can be trapped in regions of negative vorticity where the effective inertial frequency is reduced (Kunze 1985).

Wind stress impulses or fluctuations with frequencies in the near-inertial band can resonantly force inertial motions in the OSBL (Figure 1.5). Resonant wind forcing events can be considered in two phases, the initial period wind resonance that generates mixed-layer inertial currents, and the subsequent transport and decay of those currents (Gill 1984). The downward-propagating wind-generated NIWs are usually identified by clockwise (CW) rotation of horizontal velocity vector with depth (Leaman and Sanford 1975), and downward progression of KE maxima over time (Rossby and Sanford 1976). Furthermore, wind-generated NIWs often show a pronounced seasonal cycle featuring a wintertime maximum (Silverthorne and Toole 2009), and this seasonality can exist at all depths (Alford and Whitmont 2007). Thus, the energy injected from the surface winds into NIWs, and then the following downward propagation from the mixed layer into the ocean interior transferred to small-scale turbulence are important for a better understanding of the energetics of ocean circulation and diapycnal mixing in the deep ocean. The degree of deep propagation varies substantially and the dependence of near-inertial propagation on lateral structures.

Another well-known characterization of NIWs is the spectral peak at and slightly above the local inertial frequency, the so-called blue shift (Fu 1981; Sun et al. 2011; Alford et al. 2016). This blue shift of inertial peak in frequency spectrum preferentially occurs at depths with increasing mode number (Garrett 2001), and depends on many factors, such as Doppler shift by the mean flow (White 1972), background vorticity field (Kunze 1985), and storm track shifts (Zhai 2015). For instance, Fu (1981) examine the frequency of the peak of the internal wave spectrum using moored current meters in the North Atlantic, and find a considerable scatter but a definite tendency for the peak frequency to increase with depth. Fomin (1973) and Mooers (1975) also point out that the principal effect of vorticity is to shift the lower bound of the internal waveband.

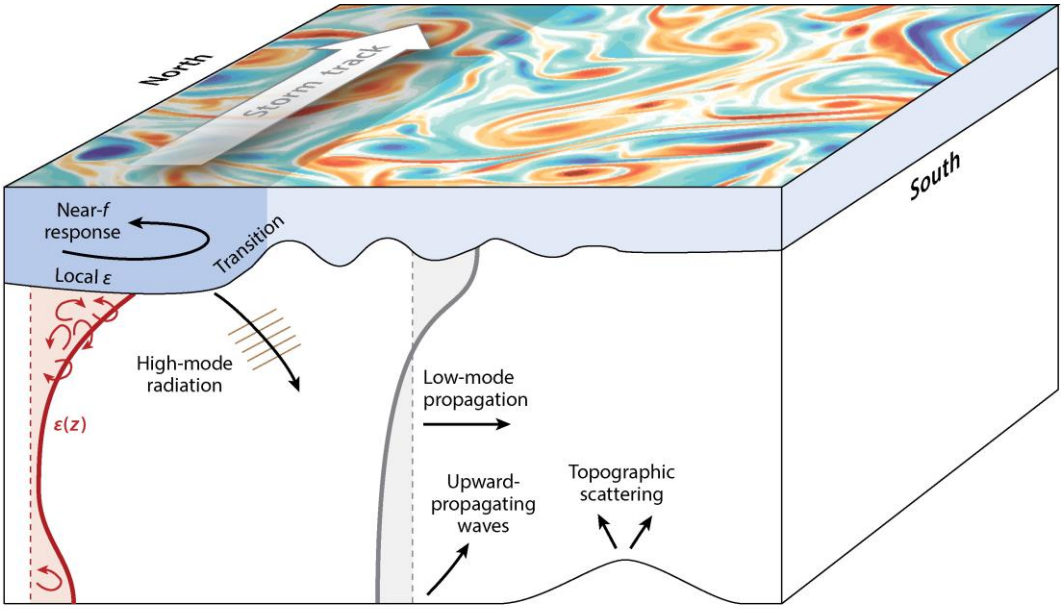


Figure 1.5: Schematic showing processes associated with near-inertial generation, dissipation, and propagation. As storms move along the storm track (thick white arrow), a local response occurs with frequencies near the local Coriolis frequency. Both high- and low-mode internal gravity waves are excited. High modes propagate along curving characteristics downward and equatorward. The higher modes have strong shear that results in mixing. Low-mode wave radiation (indicated in gray) takes the form of oscillations that propagate equatorward. Figure from Alford et al. (2016).

### 1.2.6 Summary

To summarize, oceanic submesoscale processes are manifested at horizontal scales O (1-10 km), small enough for the constraints of the Earth's rotation and oceanic vertical stratification to be overcome, but larger than that of three-dimensional turbulence. Rossby and Richardson numbers of O (1) lead to a range of dynamical instabilities in the OSBL that respond to atmospheric forcing, and interact with the mesoscale eddy field and unbalanced motions such as NIWs. These dynamics result in enhanced vertical velocities, rates of restratification and turbulent mixing, on time scales that range from a few days to the inertial period.

### 1.3 Thesis objectives

The small size of submesoscale flows and their rapidly evolving features combined with complex flow conditions in the upper ocean make measurements a considerable challenge. The Ocean Surface Mixing, Ocean Submesoscale Interaction Study (OSMOSIS) project combines observational and modeling components aiming to improve our understanding of the OSBL dynamics. In particular, a meso- and submesoscale resolving mooring array was successfully deployed and recovered during the OSMOSIS project, with cables anchored in the about 4.8 km deep water but instruments placed just about 1.5 km apart horizontally. In this thesis, I will investigate the physics underlying the annual evolution of the OSBL, with a key focus on the impact from submesoscale processes, using measurements from the OSMOSIS moorings complemented by glider, reanalysis and satellite data.

The main objectives of this thesis include:

(i) To diagnose and describe the vertical velocities at both mesoscale and submesoscale resolutions from the OSMOSIS moorings, and to quantify the contribution of upper-ocean submesoscale dynamics to the overall restratification in the open ocean over an annual cycle (Chapter 3).

(ii) To quantify competing processes in deepening and shoaling of the OSBL through closing the PV budget in the OSBL, particularly the role of submesoscale instabilities in determining the evolution of the OSBL (Chapter 4).

(iii) To investigate the respective roles of diabatic and frictional forcings in regulating the vertical stratification and circulation of the OSBL and the ocean interior (Chapter 4).

(iv) To test Taylor and Ferrari (2010)'s hypothesis for the influence of lateral buoyancy gradients on the turbulent convection in the ocean, and to investigate the dependence of SI on the destabilizing surface forcing (Chapter 4).

(v) To examine the downward propagation of NIWs and seasonality at the PAP site by using velocity measurements with different vertical resolutions. To identify the possible interactions between NIWs and submesoscale fronts (Chapter 5).

### 1.4 Thesis outline

Chapter 2: OSMOSIS moorings in the Northeast Atlantic

This chapter mainly describes the OSMOSIS moorings and the associated dataset. The OSMOSIS project, data pre-processing and some ancillary data such as satellite, reanalysis data used throughout the thesis are also outlined. Lastly, a summary characterization of the mooring site is given.

Chapter 3: The annual cycle of submesoscale vertical flow and restratification in the upper ocean

This chapter presents a record of vertical velocity and vertical buoyancy flux inferred from the OSMOSIS mooring array. The technique involves estimating vertical velocity as a residual of a density budget. Data from moorings at different separations are used to produce separate estimates for the submesoscale and mesoscale contributions. The results are discussed in context of the annual cycle and the effect on upper-ocean restratification.

Chapter 4: The annual cycle of upper-ocean potential vorticity and its relationship to submesoscale instabilities

This chapter investigates attributing processes for the evolution of the OSBL from the PV budget perspective. A mathematical framework is developed to closing the PV budget from measurements with a horizontal resolution of about 10 km, under certain simplifying assumptions appropriate for the current dataset. The submesoscale instabilities are discussed focusing on the role of SI in upper-ocean turbulent convection and its dependence with atmospheric forcing.

Chapter 5: The annual cycle of wind-generated near-inertial waves at the PAP site in the Northeast Atlantic

This chapter examines the annual cycle of wind-generated NIWs in the mooring site. In particular, a slab mixed layer model and intense measurements from one of the OSMOSIS moorings are used to study the downward propagation of the NIWs. The seasonal variability of near-inertial horizontal KE is also examined.

Chapter 6: Conclusions and future work

This chapter summarizes the main findings of this PhD research, the outstanding questions, and the recommendations for future work.

# Chapter 2: OSMOSIS moorings at the PAP site in the Northeast Atlantic

---

This chapter mainly describes the OSMOSIS moorings and the associated dataset. The OSMOSIS project, data pre-processing and some ancillary data such as satellite, reanalysis data used throughout the thesis are also outlined. Lastly, a summary characterization of the mooring site is given.

## 2.1 Introduction

Submesoscale processes have recently come into focus as an important element of upper-ocean dynamics. However, there are few observations of submesoscale processes in the upper ocean due to the difficulty in measuring such ephemeral phenomena in the ocean, particularly over periods of months to years. Submesoscales are difficult to observe as they are too small and rapidly evolving for most of the current satellites. It is also challenging to use instruments deployed in the ocean, as the instruments must be deployed close enough together to be able to observe their small-scale structure. Most of the previous observations have been made exploring either the phenomenology of selected submesoscale processes during short-term surveys (e.g., Joyce et al. 2009; Hosegood et al. 2013), or the long-term evolution of the OSBL properties at a spatial resolution unable to resolve submesoscales (e.g., Fischer et al. 2002; Weller et al. 2002; Rivas et al. 2008). The instruments on the OSMOSIS mooring array returned a unique full annual cycle of the upper-ocean properties, which have higher temporal variability compared to the snapshot of the ocean dynamics usually obtained by research surveys, and higher spatial variability compared to the long-term observations from a single mooring.

The aim of this Chapter is to set out in more detail the OSMOSIS mooring data used in Chapters 3-5. The OSMOSIS project is introduced in Section 2.2. The mooring data and preliminary data processing are described in Section 2.3. Section 2.4 summarizes the characterization of the mooring site based on the available dataset.

## 2.2 The OSMOSIS project

OSMOSIS is a UK National Environmental Research Council (NERC) research consortium aimed to improve understanding of the physical dynamics of the OSBL across multiple scales, and as a whole is expected to deliver improved parameterizations of turbulent mixing and submesoscale restratification in the NEMO (Nucleus for European Modelling of the Ocean). A large portion of the project was a comprehensive observational campaign conducted in the Northeast Atlantic from September 2012 to September 2013, which included a meso- and submesoscale-resolving mooring array of instruments combined pairs of ocean glider observations through the mooring region, and three research cruises.

The mooring observation site is approximately at the Porcupine Abyssal Plain (PAP, 48.63-48.75ºN, 16.09-16.27ºW) in the Northeast Atlantic (Figure 2.1a). The PAP site

is an abyssal plain of depth close to 4800 m, and is analogous to many open ocean areas, far away from complex topography where energetic internal waves can be generated. The PAP site lies at the eastern edge of the North Atlantic subtropical gyre, a region of weak mean flow and relatively low eddy kinetic energy (EKE), characteristic of a substantial fraction of the global ocean (Allen et al. 2013). Nevertheless, the area still has considerable mesoscale eddy activity. Coherent mesoscale vortices frequently form in or propagate through this region, penetrating as deep as several thousand meters into the ocean (Painter et al. 2010; Buckingham et al. 2016; Damerell et al. 2016). Furthermore, the location of the OSMOSIS observation site was also chosen due to the valuable historical context provided by a multidisciplinary observing system hosted by National Oceanography Centre, Southampton (NOCS; information on the PAP site observing system can be found at http://noc.ac.uk/pap), and cost-effective reasons (the PAP site is about 300 miles southwest of UK and accessible to many UK/EU ports).

## 2.3 OSMOSIS Moorings

### 2.3.1 Mooring-array design and instrumentation

One of the aims of the OSMOSIS moorings was to measure the detailed evolution of the OSBL, and then enable closure of the upper-ocean PV budget over a small patch of an oceanic gyre throughout a complete annual cycle. To accomplish this aim, nine bottom-anchored subsurface moorings were deployed over the PAP site for the period September 2012 – September 2013 (Figure 2.1a).

The array, arranged in two concentric quadrilaterals with a centrally located single mooring, is designed to obtain hydrographic and horizontal velocity measurements linked to meso- and submesoscale flows with relatively high (30-100 m) vertical resolution. The four outer moorings were clustered in a 13 km by 13 km box, and thereby resolve mesoscale flows with horizontal scales as small as the local first baroclinic Rossby radius $R_1 = \frac{N\mathcal{H}}{f}$, where $\mathcal{H}$ denotes the vertical scale of the main pycnocline, $f$ is the Coriolis frequency, and $N^2 = -\frac{g}{\rho_0}\frac{\partial \rho}{\partial z}$ is the square of the buoyancy frequency (with $g$ as gravity, $\rho$ as potential density, and $\rho_0$= 1025 kg m$^{-3}$ as a reference density). Here I will take $\mathcal{H}$ = 1 km for simplicity. The value of $R_1$ is in the range of 15-32 km throughout the year, consistent with Chelton et al. (1998). The four inner moorings are clustered more closely, in a 2.5 km by 2.5 km box, and can thus capture submesoscale flows. The ML deformation radius is defined as $R_{ML} = \frac{NH}{f}$ (with

*H* as the MLD), and lies in the range of 1-4 km with smallest values in summer and largest in winter.

Mooring sensors comprised a series of paired Nortek Aquadopp acoustic current meters (ACMs) and Seabird MicroCAT conductivity-temperature-depth (CTD) sensors at different depths, spanning the approximate depth interval 30-530 m (Figure 2.1b). The central mooring is the most heavily instrumented, having 13 CTD/ACM pairs. The inner and outer moorings have seven and five such pairs, respectively. The two nested mooring arrays return temperature, salinity, horizontal velocity and pressure observations at respective horizontal resolutions of approximately 1.5 km and 10 km for the inner and outer moorings. Mooring measurements captured most of the pycnocline plus part of the ocean interior throughout the year, and most of the ML during winter months. The vertical spacing between CTD/ACM pairs is finer above the base of the deepest winter ML (about 350 m) than below; see also Table 2.1 for detailed information on mooring instruments. ACMs and CTDs sampled every 10 and 5 minutes, respectively. Note that the cross shape of each of the mooring clusters is well suited to obtaining the lateral gradients of buoyancy and horizontal velocity required for quantifying the frontogenesis function (Chapter 3) and PV (Chapter 4). Moorings were complemented by measurements from two oceanic gliders that navigated in a bow-tie pattern across the mooring array.

Finally, the central and inner moorings were deployed with 75 kHz RDI Long Ranger ADCP (Acoustic Doppler Current Profiler) units. The objective for these ADCP units is to measure the upper-ocean horizontal velocity structure across a range of depths. As such they were deployed close to 450 m depth and pointing upwards. In Chapter 5, ACMs are complemented by measurements from the ADCP on the central mooring that provided high vertical-resolution velocity profiles to resolve vertical wavenumber spectra.

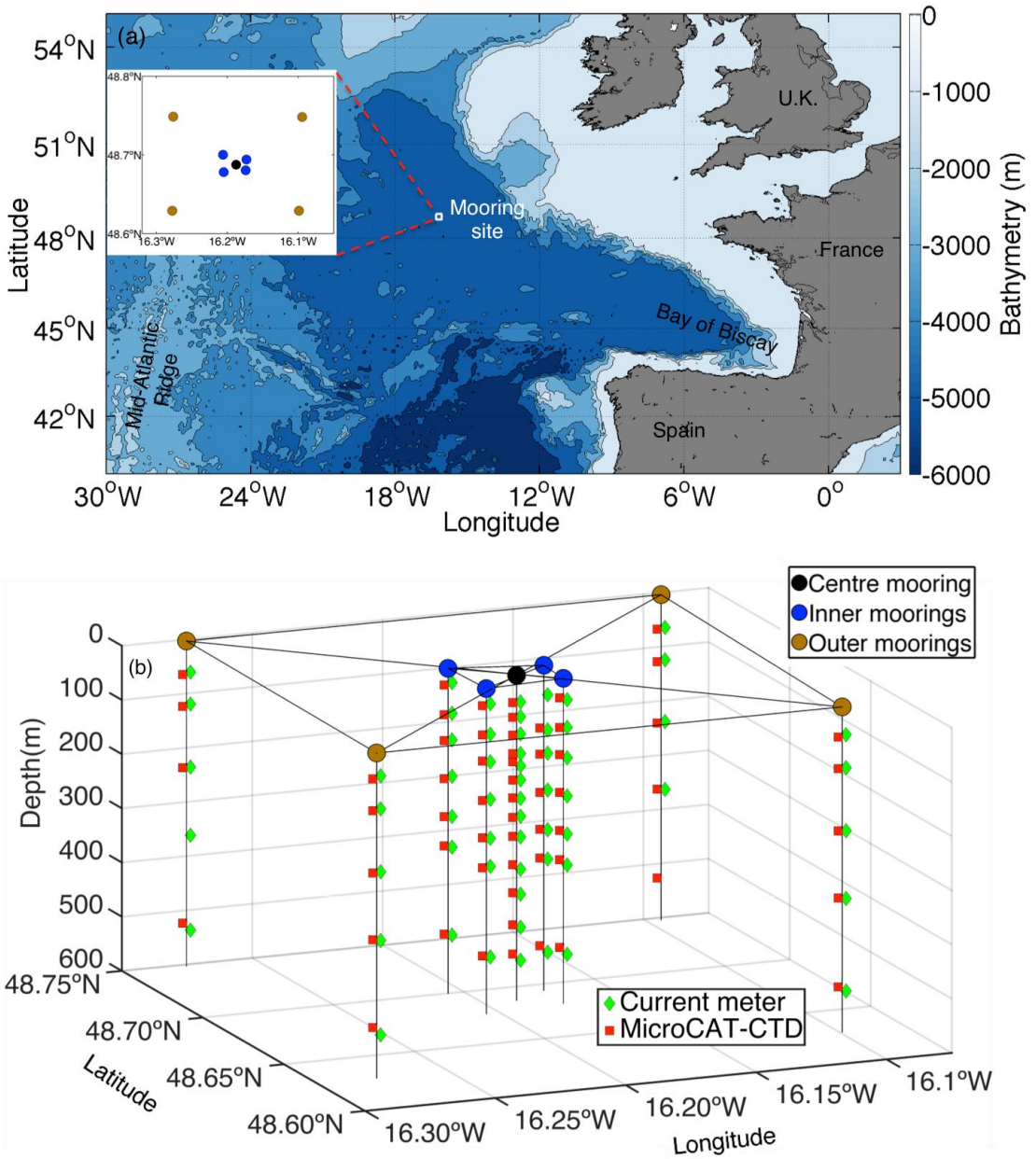


Figure 2.1: (a) Geographical location of the OSMOSIS mooring array. Land on the European continent is shaded gray, and bathymetry is shown in the colormap on the right. Inset map shows a magnification of the mooring site. The mooring array includes one central mooring (black), four inner moorings (blue) and four outer moorings (dark yellow). (b) Vertical sections of the OSMOSIS array. Current meters are shown as green diamonds and MicroCAT-CTDs are shown as red squares.

Table 2.1: Detailed configuration of the OSMOSIS moorings. * represents data loss due to sensor problem.

| Mooring | Observation period | Longitude (ºW), Latitude (ºN) | Instrument (Looking) | ACMs and CTDs pair Depth (m) | Sample Interval (min) |
|---|---|---|---|---|---|
| Central | 5 Sep 2012 – 5 Sep 2013 | 48.6875, -16.1875 | ACMs,<br><br>CTDs | 50, 77, 109, 145,168, 194, 228, 261, 299, 359, 405, 466, 527<br>50, 77, 110, 144,159, 193, 226, 262, 297*, 349, 401, 460, 514 | 10<br><br>5 |
| NE-Inner | 6 Sep 2012 – 5 Sep 2013 | 48.6940, -16.1740 | ACMs,<br>CTDs | 55, 120, 163, 231, 304, 358, 530<br>54*, 115, 163, 234, 302, 355, 517 | 10<br>5 |
| NW-Inner | 5 Sep 2012 – 5 Sep 2013 | 48.7000, -16.2060 | ACMs,<br>CTDs | 27, 84, 133, 200, 274, 331, 493<br>30, 85, 133, 203, 273, 327, 490 | 10<br>5 |
| SE-Inner | 6 Sep 2012 – 5 Sep 2013 | 48.6803, -16.1740 | ACMs,<br>CTDs | 40, 91, 147, 218, 288, 345, 510<br>35, 90, 140, 210, 280, 334, 496 | 10<br>5 |
| SW-Inner | 5 Sep 2012 – 5 Sep 2013 | 48.6780 -16.2050 | ACMs,<br>CTDs | 29, 85, 136, 205, 277, 329, 496<br>31, 85, 133, 206, 275, 330, 493 | 10<br>5 |
| NE-Outer | 8 Sep 2012 – 4 Sep 2013 | 48.7480, -16.0945 | ACMs,<br>CTDs | 61, 121, 235, 360, 511*<br>63, 123, 236, 358, 522 | 10<br>5 |
| NW-Outer | 8 Sep 2012 – 5 Sep 2013 | 48.7485, -16.2762 | ACMs,<br>CTDs | 58, 117, 233, 359, 534<br>61, 120, 233, 348*, 520 | 10<br>5 |
| SE-Outer | 18 Sep 2012 – 4 Sep 2013 | 48.6290, -16.0990 | ACMs,<br>CTDs | 52, 113, 229, 354, 525<br>55, 113, 228, 352, 516 | 10<br>5 |
| SW-Outer | 5 Sep 2012 – 5 Sep 2013 | 48.6290, -16.2775 | ACMs,<br>CTDs | 43, 104, 220, 347, 521<br>47, 106, 221, 344, 506 | 10<br>5 |

### 2.3.2 Mooring data quality control and pre-processing

The present study predominantly uses data from the moored CTD/ACM pairs and ADCP units. No breaks or losses during the mooring deployment and recovery, although several instrument failures resulted in missing CTD data at 297 m on the central mooring, 54 m on the NE-Inner mooring and 348 m on the NW-Outer mooring. Further, one ACM sensor failure resulted in missing data below 360 m on the NE-Outer mooring (also see Table 2.1). For the available measurements, missing values occurred occasionally, especially for salinity measurements. These missing data were reconstructed via linear interpolation. Year-long time series of each property were checked and obviously erroneous values were deleted. Another issue associated with the data set was noted after looking at time series of pressure. The time series of pressure of the CTD sensor at 262 m on the central mooring contained one distinct downward shift (~30 m) from July to September 2013. These values were corrected to original sensor depth.

Raw output from the ADCP units contained missing values and extremely high values outside of the realistic range, due to sound absorption, instrumental noise and mooring motion. For the whole water column, bins and profiles with a 'total percent good data' value smaller than 25 is replaced with NaN (not-a-number). The velocity error can be large near sea surface, so velocities greater than 1 m $s^{-1}$ or larger were excluded. Horizontal velocity measured by the ACMs is relatively more reliable (checked by visualization including time series representations, vector stick and contour plots), and therefore can be used as a proxy for ADCP measurements.

For each mooring, I linearly interpolate measurements of temperature, salinity and horizontal velocity onto surfaces of constant depth at 10 m intervals between depths of 50 m and 520 m, and onto uniform 10 minute intervals between 5 September 2012 and 5 September 2013 (Figure 2.2, and Figures A1-A4 in Appendix). Potential density (referenced to the ocean surface) and depth are calculated from interpolated temperature, salinity and pressure using the Gibbs Seawater Oceanographic Toolbox (McDougall and Barker 2011). Compressibility effects are considered to be negligible over the top 520 m. These unfiltered versions of data time series are indicated by the subscript *'raw'*. Subsequently, the 10-minute potential density and horizontal velocity data are averaged onto hourly intervals.

In this thesis, the conventional definition of seasons is adopted: fall (21 September to 20 December), winter (21 December to 20 March), spring (21 March to 20 June) and summer (21 June to 20 September).

### 2.3.3 Additional datasets

*OSMOSIS glider data* (Chapters 3-5): The depth of the surface ML is calculated from the glider data using a threshold value of density ($\Delta\rho = 0.03\ kg\ m^{-3}$) from a near-surface value at 10 m depth (Damerell et al. 2016). These data were kindly processed and given to me by Dr. Gillian Damerell at University of East Anglia. Additionally, the dissipation rate estimates are derived from high-frequency fluctuations in the glider vertical velocity using a generalization of the large eddy method of Beaird et al. (2012) developed by Evans et al. (2018, manuscript submitted to *Geophys. Res. Lett.*), and these data were kindly processed and given to me by Dr. Dafydd Gwyn Evans at University of Southampton.

*Wind data* (Chapter 5): The observed wind speed is taken from the PAP Met. Buoy (Figure 5.1) with a time interval of 1 hour from 5 September to 28 December 2012.

*Reanalysis data* (Chapters 3-5): The surface heat flux, freshwater flux and the surface wind stress are taken from the ECMWF (European Centre for Medium-Range Weather Forecasts) ERA-Interim reanalysis product (with a time interval of 3 hours from 5 September 2012 to 5 September 2013, available from http://data-portal.ecmwf.int/) at the point closest to the central mooring site (Dee et al. 2011). The net heat flux was calculated as the sum of shortwave radiation, long wave radiation, latent heat flux and sensible heat flux.

*Satellite data* (Chapters 3-4): Geostrophic velocities ($u_g, v_g$) are obtained from the delayed-time gridded $0.25^o \times 0.25^o$ AVISO product at the gridpoints nearest to the OSMOSIS site, and interpolated to the central mooring site. Furthermore, in order to identify and track mesoscale eddies, AVISO merged satellite altimeter sea level anomaly (SLA) during the experiment period is also used.

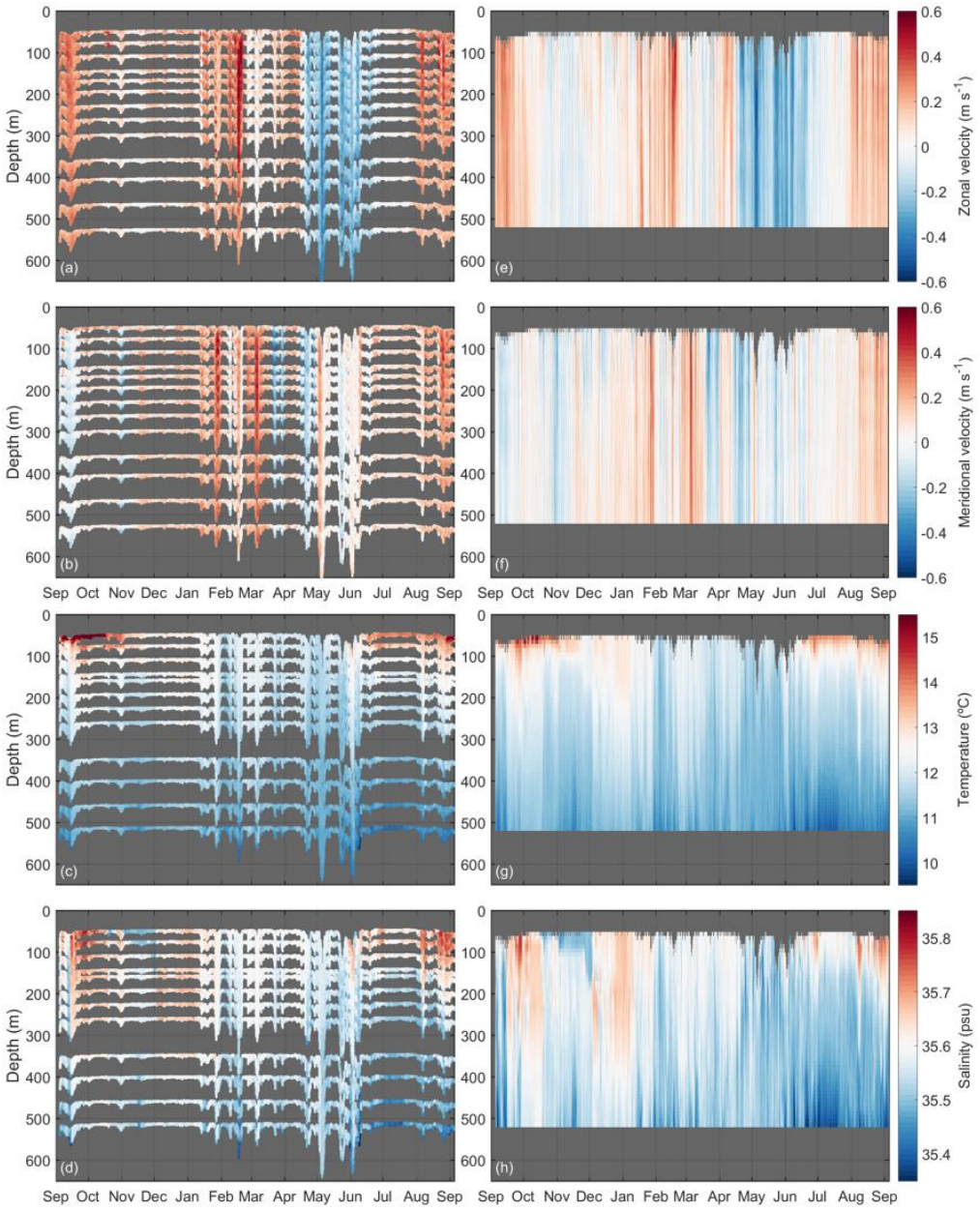


Figure 2.2: Observations of (a) zonal velocity, (b) meridional velocity, (c) temperature and (d) salinity as a function of time (months) and depth (m) on sensors on the central mooring. (e) Zonal velocity, (f) meridional velocity, (g) temperature and (h) salinity linearly interpolated onto a 10-min and 10-m grid. Depths not sampled by the deployed instrumentation are colored in dark grey.

### 2.4 Overview of the in situ observation

The OSMOSIS moorings provide, for the first time, estimates of the small-scale turbulence deepening and the meso- and submesoscale processes shoaling the OSBL simultaneously in the mid-latitude ocean over a complete annual cycle. The availability

of high-fidelity time series from the OSMOSIS moorings allows me to characterize the annual cycles in upper ocean properties at the PAP site.

Figure 2.2 shows the full record of horizontal velocity, temperature and salinity at the central mooring, both from the mooring sensors themselves and the interpolated values for comparison. The zonal and meridional velocity both reveal variability covering a wide range of processes, such as semidiurnal tides, NIWs, submesoscale flows, mesoscale eddies, and large-scale mean flows. The magnitude of the zonal and meridional velocity is in the range of -0.6 - 0.6 m $s^{-1}$. The year-mean zonal velocity is westward above 400 m, slightly transitioning to eastward below that (Figure 2.3a). The year-mean meridional velocity also exhibits a transitioning, from northward above about 100 m to southward below that (Figure 2.3b). The year-mean current is fairly weak, less than 0.05 m $s^{-1}$.

Measured temperature at the central mooring is highly variable over time, and partially compensates salinity. Temperatures are more variable near the ocean surface. The near-surface temperature (~50 m, the top CTD sensor at the central mooring) shows a pronounced seasonal cycle, which is largely governed by the seasonal variability of surface heat flux. Near-surface temperature steadily decreases from early September (about 15 ºC) to the end of December, after which SST remains relatively cool, between 10 and 12 ºC. These cool temperatures persist throughout the winter, abruptly warming in June with the temperature back to about 15 ºC. Temperature in the ocean interior is consistently lower than the near-surface temperature, and dominated by changes associated with slowly-evolving baroclinic eddies advected through the mooring array. Salinity acts more like a passive tracer at the study region, varying between 35.4 and 35.8 psu. Furthermore, year-mean temperature decreases with depth from about 13 ºC at 60 m to 10.8 ºC at 500 m (Figure 2.3c). A similar trend can be found in salinity, of which the mean value decreases from 35.60 psu to 35.48 psu from 60 m to 500 m (Figure 2.3d).

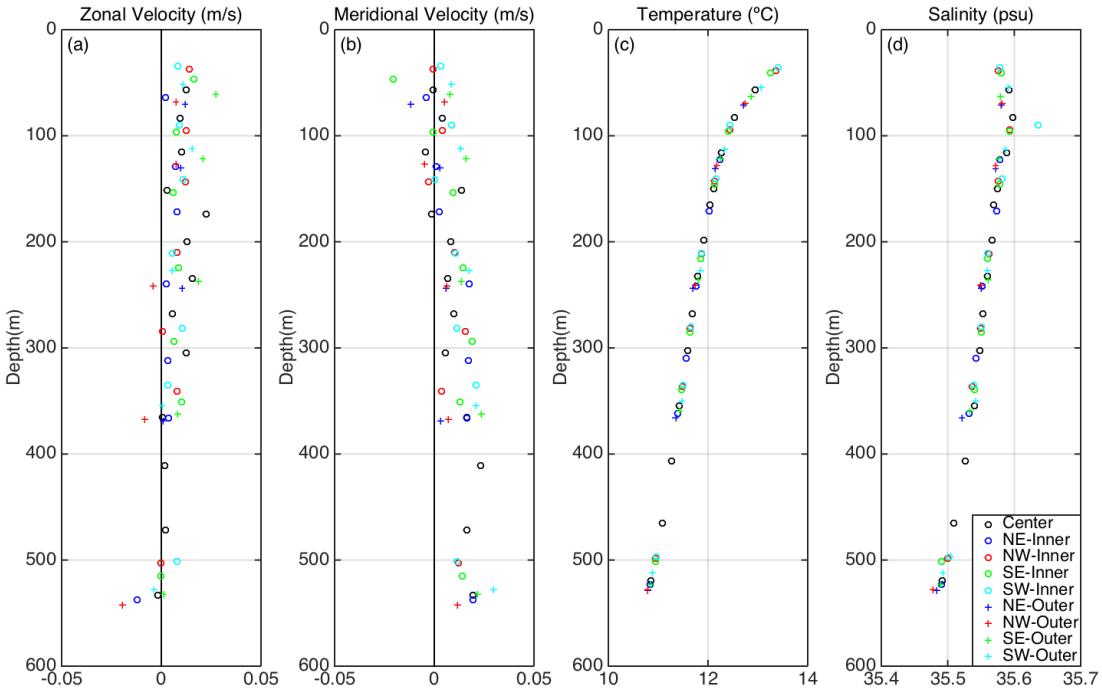


Figure 2.3: Year mean of (a) zonal velocity (m $s^{-1}$), (b) meridional velocity (m $s^{-1}$), (c) temperature (ºC) and (d) salinity (psu) at the OSMOSIS site.

The year-long surface heat flux, freshwater flux and wind stress at the OSMOSIS site are shown in Figure 2.4. Surface heat flux exhibits a significant seasonal cycle, swing from sizeable surface cooling (negative values) periods in fall and winter to surface heating (positive values) in spring and summer. Intense cooling exceeds -400 W $m^{-2}$, and the year-mean value reaches about -42 W $m^{-2}$, indicating a net destabilizing of buoyancy to the surface of the ML from the atmospheric forcing. In contrast, the surface freshwater flux is more intermittent, and negligible compared to the surface heat flux.

Wind stress is highly variable with a mean value of 0.18 N $m^{-2}$. Several events of large wind stress approaching 1 N $m^{-2}$ occurred mostly during winter and early spring (e.g., late-December, late-January and mid-April). The orientation of the wind speed is also highly variable over the entire year with a decorrelation time scale approximately 1.3 days.

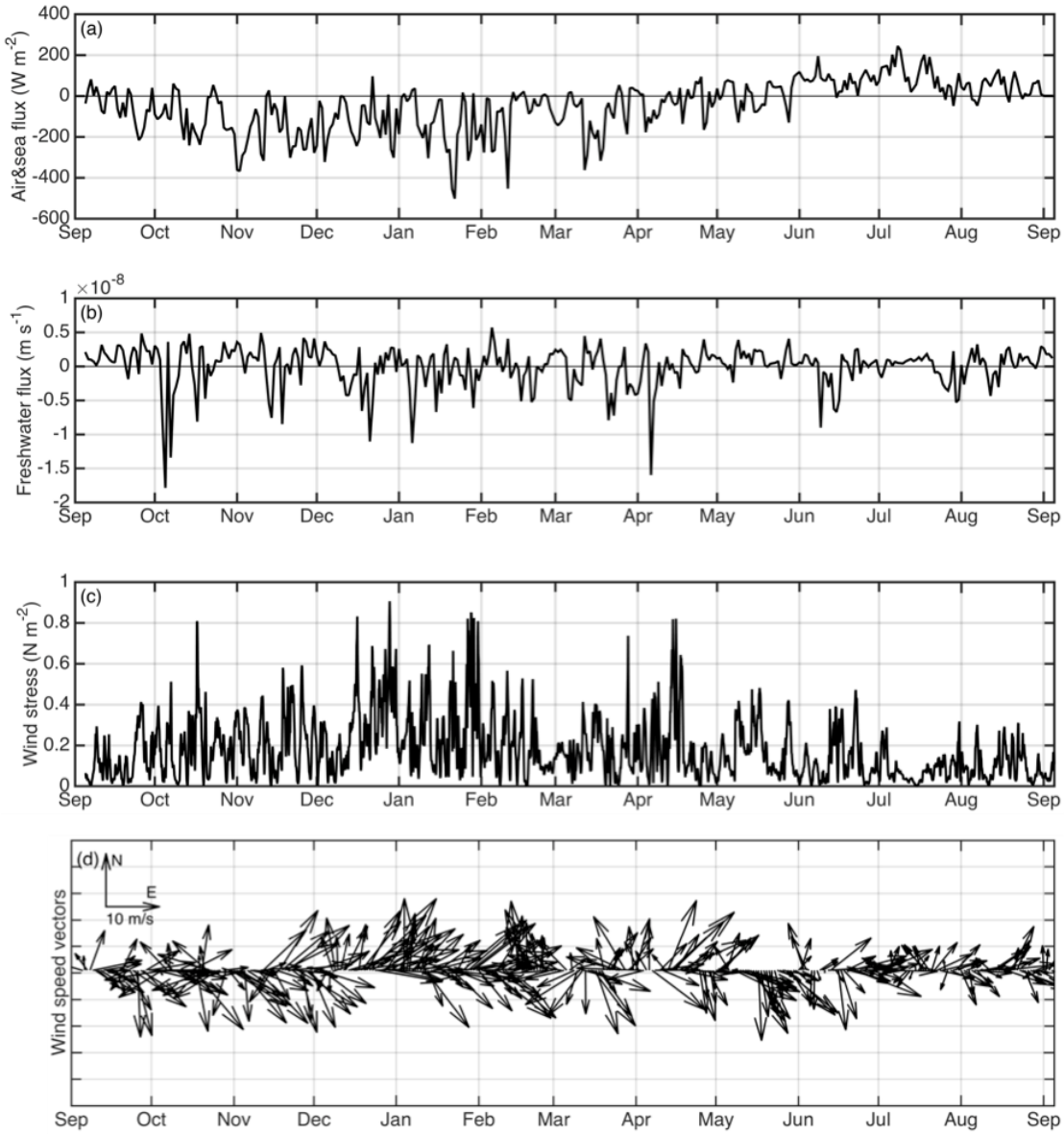


Figure 2.4: Year-long time series of (a) surface heat flux (W $m^{-2}$), (b) freshwater flux (m $s^{-1}$), (c) wind stress magnitude (N $m^{-2}$) and (d) daily-averaged wind speed vectors (m $s^{-1}$) at the OSMOSIS site from September 2012 to September 2013.

# Chapter 3: The annual cycle of submesoscale vertical flow and restratification in the upper ocean

---

This chapter presents a record of vertical velocity and vertical buoyancy flux inferred from the OSMOSIS mooring array. The technique involves estimating vertical velocity as a residual of a density budget. Data from moorings at different separations are used to produce separate estimates for the submesoscale and mesoscale contributions. The results are discussed in context of the annual cycle and the effect on upper-ocean restratification.

## 3.1 Abstract

Numerical simulations suggest that submesoscale turbulence may transform lateral buoyancy gradients into vertical stratification, and thus restratify the upper ocean via vertical flow (Capet et al. 2008b; Mensa et al. 2013; Rosso et al. 2014; Callies et al. 2016). However, the observational evidence for this restratifying process has been lacking due to the difficulty in measuring such ephemeral phenomena, particularly over periods of months to years. This study presents an annual cycle of the vertical velocity and associated restratification estimated from two nested clusters of meso- and submesoscale-resolving moorings, deployed in a typical mid-ocean area of the Northeast Atlantic. Vertical velocities inferred using the non-diffusive density equation are substantially stronger at submesoscales (horizontal scales of 1-10 km) than at mesoscales (horizontal scales of 10-100 km), with respective root mean square values of $20.7 \pm 10.9$ m/day and $9.8 \pm 6.3$ m/day. The largest submesoscale vertical velocities and rates of restratification occur in events of a few days duration in winter and spring. These events commonly coincide with the enhancement of submesoscale lateral buoyancy gradients, which is itself associated with persistent mesoscale frontogenesis. This suggests that mesoscale frontogenesis is a regular precursor of the submesoscale turbulence that restratifies the upper ocean. The upper-ocean restratification induced by submesoscale motions integrated over the annual cycle is comparable in magnitude to the net destratification driven by local atmospheric cooling, indicating that submesoscale flows play a significant role in determining the climatological upper-ocean stratification in the study area.

## 3.2 Introduction

Vertical flows in the OSBL play a key role in shaping upper-ocean stratification, and in exchanging mass and tracers within and across the mixed layer (Klein and Lapeyre 2009; Rosso et al. 2014; Mahadevan 2016; McWilliams 2016). Oceanic submesoscale processes (defined here as those linked to subinertial flows with horizontal scales of 1-10 km) have been shown, mostly through numerical simulations, to be effective at inducing strong vertical velocities in the upper ocean (Mahadevan and Tandon 2006; Capet et al. 2008a). The occurrence of vertical motion at submesoscales is associated with a wide range of mechanisms characterised by distinct dynamics, such as surface frontogenesis (Lapeyre et al. 2006; Capet et al. 2008b; Gula et al. 2014), mixed-layer BCI (Boccaletti et al. 2007; Fox-Kemper et al. 2008), wind-driven

frictional effects at fronts (Thomas and Lee 2005; Thomas and Ferrari 2008), nonlinear Ekman pumping (i.e., an extended classic Ekman theory to include the tilting of vertical relative vorticity; Thomas and Rhines 2002; Mahadevan et al. 2008), symmetric instability (Taylor and Ferrari 2010; Thomas et al. 2013; Brannigan 2016) and mesoscale-submesoscale coupling (Ramachandran et al. 2014). Most of the aforementioned studies have focused on regions of strong frontal currents or have made use of idealised simulations, while less attention has been devoted to investigating submesoscale vertical flows in the open ocean - which constitutes the majority of the marine environment.

The generation of submesoscale motions has been extensively documented in the mixed layer, where the weak local stratification permits the rapid amplification of baroclinically unstable modes (Haine and Marshall 1998). In contrast, balanced flow in the ocean interior is commonly considered to follow QG dynamics, characterized by mesoscale motions with horizontal scales of 10-100 km (approaching or exceeding the first baroclinic deformation radius) and vertical scales of O (1 km). These balanced interior flows are often generated by mesoscale BCI (Gill et al. 1974), whereby slumping of isopycnals unfolds over relatively long time scales on the order of weeks to months (Charney 1971). Compared to mesoscale BCI in the interior, BCI in the mixed layer develops over substantially smaller horizontal scales (1-10 km) and shorter time scales of order 1 day (Boccaletti et al. 2007). Both numerical simulations and observations indicate that variations in the intensity of mixed-layer BCI play a significant role in the seasonal modulation of submesoscale flows in the upper ocean, specifically in terms of submesoscale KE (Capet et al. 2008b; Brannigan et al. 2015; Callies et al. 2015), vorticity (Sasaki et al. 2014; Buckingham et al. 2016) and instabilities (Mensa et al. 2013; Thompson et al. 2016). Mixed-layer BCI has been parameterised as an overturning streamfunction confined to the mixed layer (Fox-Kemper et al. 2008), acting to rapidly restratify the upper ocean by releasing APE. Simulations by Callies et al. (2016) indicate that mixed-layer BCI may energise the entire mixed layer and produce intense vertical velocities. In contrast, the impact of balanced submesoscale motions with characteristic horizontal scales of 1-10 km on interior vertical flows remains relatively understudied, although several recent numerical investigations suggest that these flows may play an important role in vertical exchanges across and below the mixed layer base (e.g., Brannigan 2016).

A common outcome of the unfolding of mesoscale BCI is the occurrence of

frontogenesis, which is associated with large vertical velocities (Spall 1995; McWilliams et al. 2009). The connection between frontogenesis and restratification was established in the classical work of Hoskins and Bretherton (1972), who show that, in the presence of a larger-scale strain flow, an ageostrophic secondary circulation leads to buoyancy and momentum transports that maintain thermal wind balance. In the frontogenetic scenario, this ageostrophic secondary circulation gradually slumps isopycnals and restratifies the upper ocean (i.e. it elicits an upward buoyancy flux). Thomas and Ferrari (2008) suggest that frontogenesis can penetrate from the ocean surface to depths beyond the mixed layer base in the presence of deep fronts. While there is evidence of mesoscale-driven frontogenesis leading to upper-ocean restratification (Lapeyre et al. 2006; Klein et al. 2011), its role in generating submesoscale flows remains an open question, and observational evidence has been lacking.

A key step in advancing our understanding of submesoscale turbulence and its associated restratification is to obtain representative observations of these phenomena in the upper ocean. However, due to the small magnitude of the vertical flows involved, the effects of submesoscale motions on stratification are difficult to measure directly. For several decades, the QG omega equation has been widely used to estimate the vertical velocity for mesoscale flows (Pollard and Regier 1992; Martin and Richards 2001; Naveira Garabato et al. 2001; Thomas and Joyce 2010). At the submesoscale, ageostrophic motions are increasingly important, and the QG approximation provides a sub-optimal representation of the dynamics governing the vertical flow (Mahadevan 2016). Further, the traditional SeaSoar surveys, to which the QG omega equation is usually applied, often suffer from a spatio-temporal resolution too coarse to resolve submesoscale flows (Klein and Lapeyre 2009). However, the OSMOSIS mooring measurements are unable to provide sufficient spatial resolution to solve the QG omega equation or its variants (e.g. semi-geostrophic omega equation). An inverse formulation recently developed by Thomas et al. (2010) provides a dynamically comprehensive diagnostic of submesoscale vertical velocity from Seasoar data, but relies on the measurement of an assortment of spatial gradients and on specific assumptions about the character of temporal variability.

An alternative approach, based on the density conservation equation, has been successfully applied to oceanographic mooring observations. Previous research has pursued this method to estimate vertical velocity from individual moorings under the

assumption of geostrophy (Bryden 1980; Lindstrom and Watts 1994; Phillips and Rintoul 2000; Sévellec et al. 2015). My study follows in the footsteps of this body of work, yet applies the density conservation equation without assuming geostrophy to hold (see Section 3.3.3).

In this Chapter, I document an annual cycle of the vertical velocity and buoyancy flux (i.e. the rate of restratification by the vertical flow) associated with balanced motions with horizontal scales characteristic of the mesoscale and submesoscale. These diagnostics are based on measurements obtained with a mooring array, deployed in a typical mid-ocean area of the Northeast Atlantic as part of the OSMOSIS experiment. The outline of Chapter is as follows. Data and methods are introduced in Section 3.3. Section 3.4 describes the mooring site and outlines the annual cycle of meso- and submesoscale vertical velocities and buoyancy fluxes. Section 3.5 provides a discussion of the role of mesoscale-driven frontogenesis in forcing submesoscale turbulence. Section 3.6 demonstrates the robustness of my approach to calculating vertical velocity with a numerical model. Conclusions are given in Section 3.7.

## 3.3 Data and Methods

### 3.3.1 Mooring data

Note that, in this Chapter, my definition of submesoscale refers to subinertial motions of a specific horizontal scale (1-10 km), and thus excludes internal gravity waves and other superinertial phenomena. Previous analyses of the OSMOSIS mooring (Buckingham et al. 2016) and glider (Thompson et al. 2016) observations reveal that these subinertial motions exhibit some of the characteristics of active submesoscale dynamics (McWilliams 2016), e.g., skewness in the vertical component of relative vorticity and occurrence of mixed-layer BCI within and below the base of the mixed layer.

### 3.3.2 Data processing and filtering

My approach is to distinguish meso- and submesoscale processes, not only by spatial scale as determined by the design of the outer and inner moorings, but also by temporal scale. To do this, I first apply different low-pass filters to outer and inner mooring measurements. Our initial consideration in defining the filter cut-offs is the characteristic advective time scale of each mooring array, i.e. the time typically required for a water parcel to cross the full lateral extent of each array. As the root mean

square (RMS) upper-ocean horizontal velocity at the OSMOSIS site is 0.19 m/s, advective time scales of 30 hours and 6 hours may be respectively estimated for the outer and inner mooring domains. All (hourly) potential density and horizontal velocity data from the outer mooring array are low-pass filtered with a fourth-order Butterworth filter (whose power decreases by 24 dB per octave), with a cut-off determined by the outer-array advective time scale (30 hours). In turn, data from the inner mooring array are filtered with a cut-off of one inertial period (16 hours), so as to comply with our definition of submesoscale flow by removing all variability in the internal wave band. In all calculations of lateral gradients, data from the central mooring are low-pass filtered with the same cut-off as the data from the (outer or inner) mooring array domain from which the gradients are computed.

In the following, I refer to parameters (e.g., vertical velocity or lateral buoyancy gradient) estimated from the outer and inner moorings as *outer* and *inner* quantities, respectively. Outer quantities are representative of meso- and larger-scale flows. In contrast, inner quantities include all dynamically balanced motions with horizontal scales larger than $R_{ML}$ and temporal scales longer than one inertial period, including (sub-)mesoscale and larger-scale flows. Unbalanced motions, such as internal tides, near-inertial flows and other high-frequency motions, are removed by the low-pass filtering (16 hours). For simplicity, I use the subscripts *'C'*, *'I'* and *'O'* to represent data from the central, inner and outer moorings, respectively. Further, I use the subscripts *'16h'* and *'30h'* to denote data filtered over 16 hours and 30 hours, respectively (e.g., $w_{CI,16h}$ denotes vertical velocity calculated from 6-hour low-pass filtered data from the central and inner moorings). Daily-averaged vertical velocity and buoyancy flux are displayed in Figures 3.4-3.6, denoted as $<\cdot>$. A further 30-hour low-pass filter is applied to inner quantities when compared or related to outer quantities in Section 3.5. Finally, annual means are denoted by an overbar ($\bar{\cdot}$), and fluctuations ($'$) are defined as departures from the annual mean.

Finally, the decorrelation time scale is estimated from the e-folding scale of the autocorrelation function. A bootstrap method is employed for confidence interval estimates by randomly sampling 90% of the data 10,000 times and selecting the 250$^{th}$ largest and smallest values.

### 3.3.3 Vertical velocity and buoyancy flux calculation

The density conservation equation is used to determine vertical velocity, neglecting the diffusion term,

$$D_t\rho = \partial_t\rho + u\partial_x\rho + v\partial_y\rho + w\partial_z\rho = 0, \quad (3.1)$$

where $D_t$ is the material derivative; $t$ is time; $u$,$v$,$w$ denote the velocity components in the $x$,$y$,$z$ coordinate system; and $\partial_t$, $\partial_x$, $\partial_y$and $\partial_z$ are the temporal, zonal, meridional, and vertical partial derivatives. Note that vertical velocity in the mixed layer is not calculated, as the neglected diffusion term becomes important there. The vertical velocity is estimated from the sum of a local isopycnal displacement term and a horizontal advection term, by rearranging Equation 3.1 as

$$w = -\frac{\partial_t\rho}{\partial_z\rho} - \frac{u\partial_x\rho + v\partial_y\rho}{\partial_z\rho}. \quad (3.2)$$

The first term on the RHS of Equation 3.2, defined as

$$w_t = -\frac{\partial_t\rho}{\partial_z\rho}, \quad (3.3)$$

denotes the Eulerian change in the position of isopycnals and is associated with vertical migration of isopycnals or isopycnal heave. The second term on the RHS of Equation 3.2 is the vertical velocity associated with flow along sloping isopycnals, and is defined as

$$w_h = -\frac{u\partial_x\rho + v\partial_y\rho}{\partial_z\rho}. \quad (3.4)$$

The vertical derivative of $\rho$ (i.e. $\partial_z\rho$) is calculated as a centered finite difference in depth, and used to compute $N^2$. The temporal derivative of $\rho$ (i.e. $\partial_t\rho$) is calculated as a second-order centered finite difference in time. These two terms ($\partial_z\rho$ and $\partial_t\rho$) and horizontal velocity ($u$ and $v$) are computed from measurements at the central mooring, whereas lateral density gradients ($\partial_x\rho$ and $\partial_y\rho$) are respectively derived from outer and inner mooring measurements for outer and inner vertical velocities ($w_{CO,30h}$ and $w_{CI,16h}$). Horizontal velocities in the upper ocean are coherent for time scales greater than 12 h (Buckingham et al. 2016). As indicated in Section 3.3.2, the two components of $w_{CO,30h}$ and $w_{CI,16h}$ can be expressed as $(w_t)_{C,30h}$, $(w_h)_{CO,30h}$ and $(w_t)_{C,16h}$, $(w_h)_{CI,16h}$, respectively. Note that, since superinertial flows are removed by low-pass filtering, all density and velocity data, both estimates of $w$ and their components ($w_t$ and $w_h$) exclusively reflect contributions from subinertial flows.

The validity of this method for the estimation of vertical velocity below the mixed layer is demonstrated with the aid of numerical model output in Section 3.6.1. Further,

I follow the approach of Bryden (1980), who showed that the $w_h$ term can be estimated from the rotation of the horizontal velocity vector with depth by assuming geostrophic balance, to ground-truth our diagnostics of vertical velocity in Section 3.6.2.

The perturbation vertical buoyancy flux is $w'b'$, where vertical velocity perturbation $w' = w - \bar{w}$ is defined as departures from the annual mean, buoyancy $b$ is defined as $b = -\frac{g}{\rho_0}(\rho - \rho_0)$ and buoyancy perturbation is defined as $b' = b - \bar{b} = -\frac{g}{\rho_0}(\rho - \bar{\rho})$, such that the choice of reference density $\rho_0$ has negligible effect on $b'$. In order to compare the magnitude of outer and inner restratification with atmospheric forcing, the eddy component of the vertical buoyancy flux can be represented in terms of an equivalent heat flux, defined as,

$$Q_w = w'b'\frac{C_p\rho_0}{\alpha g}, \tag{3.5}$$

where $C_p$ is the specific heat capacity, and $\alpha$ is the thermal expansion coefficient of seawater. Note that the eddy component here incudes seasonal cycle.

The horizontal motion of the moorings is the main source of uncertainty in our calculation of vertical velocity. Unknown variability in the distances between individual moorings introduces uncertainty into $\partial_x\rho$ and $\partial_y\rho$ that is subsequently propagated into derived variables. Following Buckingham et al. (2016), I modeled the inner-mooring distance perturbations associated with mooring motion as a Gaussian white noise process with zero mean and non-zero variance, estimated from the time integration of differential horizontal currents. I used the stochastic realizations of mooring positions thus obtained in a Monte Carlo approach to quantify the uncertainty in inner vertical velocity (Figures 3.5e-f) and associated equivalent heat flux (Figure 3.7) introduced by mooring motion. This source of uncertainty is also estimated for the equivalent outer diagnostics.

A secondary limitation of the dataset is related to mooring knock-down, i.e. the pulling downward of a mooring by the drag of water flowing past the mooring (Meinen 2008). This introduces temporal variability in the vertical positions of the moored instruments, although large vertical excursions are rare (e.g., vertical excursions in excess of 100 m occur only in ~0.5% of the mooring record; see Figure 3.1c).

As the vertical resolution of the measurements is limited, the vertical translation of the instruments introduces uncertainty into our estimation of $w$. We have assessed the magnitude of this error by repeating the calculation of vertical velocity after sampling

the profile of vertical stratification $N^2$ at higher and lower vertical resolutions than in our standard mooring data set. For this exercise, we use the OSMOSIS glider measurements (Thompson et al. 2016), which sampled the water column at a vertical resolution of 2-4 m throughout the year. We find that our diagnostics' sensitivity to the vertical resolution of stratification is modest. For instance, varying the vertical resolution by a factor of 2 yields differences in the RMS value of $w$ of 15-35% relative to the original calculation. Increasing vertical resolution results in an increase of peak values of $N^2$, and thus yields slightly reduced vertical velocities.

Finally, to test the impact of instrumental errors in the computation of vertical velocity, we propagate the measurement uncertainty in Equations. 3.2-3.4. Following Naveira Garabato et al. (2001), we introduce instrumental random noise of prescribed amplitude ($\pm 4\times10^{-3}$ K for temperature, $8\times10^{-3}$ psu for salinity and 1% of the measured value $\pm\, 5 \times 10^{-3}$ m s$^{-1}$ for horizontal velocity) and allow these uncertainties to accumulate in the calculation of $w$, with confidence intervals computed at the 90% level using a Monte Carlo approach. Results suggest that instrumental errors lead to relative uncertainties of <6% in $w$ and its components.

### 3.3.4 Frontogenesis function

In the upper ocean, a large-scale confluent flow intensifies lateral buoyancy gradients through frontogenesis. This effect is quantified as

$$D_t(\nabla_h b) = \vec{Q} = \left(-u_x b_x - v_x b_y\,, -u_y b_x - v_y b_y\right), \tag{3.6}$$

where $\vec{Q}$ is the 'Q vector' (Hoskins et al. 1978); and $\nabla_h b = \left(b_x, b_y\right)$ is the lateral buoyancy gradient. Note that, under the QG approximation, the structure of the vertical velocity associated with the mesoscale circulation of the front is solely determined by the divergence of $\vec{Q}$ (Hoskins et al. 1978; Holton 2004). We draw on this dynamical relationship to further demonstrate the robustness of our density-conservation-based estimates of $w$, by showing that the divergence of $\vec{Q}$ from the outer array is significantly correlated with our diagnosed $w$ (Section 3.6.3).

Following Hoskins (1982), I use the frontogenesis function to diagnose the impact of frontogenesis on the magnitude of lateral buoyancy gradients,

$$Fs = \frac{1}{2} D_t(|\nabla_h b|^2) = \vec{Q} \cdot \nabla_h b. \tag{3.7}$$

Additionally, I define the current speed as

$$U = \sqrt{u^2 + v^2}, \tag{3.8}$$

and EKE as

$$EKE = \frac{1}{2}\left(u'^2 + v'^2\right). \tag{3.9}$$

This definition is re-expressed as $EKE_g = \frac{1}{2}\left({u_g}^2 + {v_g}^2\right)$ when calculating the geostrophic EKE associated with the geostrophic velocity $(u_g, v_g)$, estimated from AVISO sea surface height data.

### 3.3.5 Rossby and balanced Richardson numbers

Dynamically, submesoscale flows are characterized by Rossby and balanced Richardson numbers of O(1), indicating that the Earth's rotation is significant but not dominant in governing the dynamics of the flow (Thomas et al. 2008). Here we define the Rossby number as

$$\mathrm{Ro} = \zeta / f, \tag{3.10}$$

where $\zeta = v_x - u_y$ is the vertical component of relative vorticity. The balanced Richardson number is defined as

$$\mathrm{Ri}_B = N^2/(\partial U_g/\partial z)^2 = f^2 N^2/|\nabla_h b|^2. \tag{3.11}$$

## 3.4 Results

### 3.4.1 Annual cycle of upper-ocean hydrography and horizontal flow

The 30-hour low-pass-filtered time series of buoyancy perturbation $b'_{C,30h}$, stratification $N^2_{C,30h}$, and current speed $U_{C,30h}$ at the central mooring are shown in Figures 3.1a-c. In general, the near-surface $b'_{C,30h}$ (Figure 3.1a) is greatly affected by atmospheric forcing, which draws heat out of the ocean during winter and spring and injects heat into the ocean during fall and summer. In the ocean interior, water is advected by slowly-evolving baroclinic eddies through the mooring array, as is clearly shown by steep potential density contours (e.g. 4-9 June, 6-11 August). The maximum buoyancy perturbation $b'_{C,30h}$ occurs near the surface (at ~80 m) at the end of September 2012, when it attains $2.5\times10^{-3}$ m s$^{-2}$. Glider observations show that the compensation between temperature and salinity is common for the entire year, while lateral buoyancy gradients still persist and are able to exist and extend to depths of 500 m or more (Damerell et al. 2016; Thompson et al. 2016).

The MLD (Figure 3.1b) exhibits a significant seasonal cycle, shoaling to less than 30 m during summer and deepening to approximately 300 m during winter. The ocean is generally stratified with a shallow mixed layer above a strongly stratified pycnocline during the fall and summer months (e.g., September and July), coincident with high values of $b'_{C,30h}$due to atmospheric heating during these periods (Figure 3.1a). This strongly stratified pycnocline inhibits the outcropping of isopycnals from the ocean interior to the mixed layer. During wintertime, unstable stratification (i.e. $N^2_{C,30h} < 0$) occurs frequently within the mixed layer, indicating the occurrence of GI. A relatively weakly stratified pycnocline lies below the deep mixed layer, and isopycnal outcropping is common during winter and spring months (e.g., mid January to mid April). The maximum value of $N^2$ from mooring measurements is approximately $0.4 \times 10^{-5}\text{s}^{-2}$ ($N_{C,30h}/f$ = 18) occurring sporadically in the 200-300 m depth range during winter, and $8 \times 10^{-5}\text{s}^{-2}$ ($N_{C,30h}/f$ = 82) at ~110 m outside of winter, manifesting the strong seasonal cycle of upper-ocean stratification at the OSMOSIS site.

Whereas the maximum $U_{C,30h}$ exceeds 0.5 m s$^{-1}$ (Figure 3.1c), the annual-mean velocity magnitude $\overline{U_{C,30h}}$ is less than 0.05 m s$^{-1}$, characteristic of open-ocean regions with a weak mean flow. Intense flows typically coincide with periods of large mooring knock-down (see white blocks in Figure 3.1c). The depth-averaged $EKE_{C,30h}$ estimated from the central mooring matches well with $EKE_g$ from AVISO, as shown in Figure 3.1d. $EKE_{C,30h}$ peaks at 0.12 m$^2$ s$^{-2}$ in May, a factor of 4 smaller than values of ~0.5 m$^2$ s$^{-2}$ observed in the Gulf Stream (Zhai et al. 2008). $EKE_{C,30h}$ exhibits more high-frequency variability than $EKE_g$, which typically has coarser temporal resolution and smaller magnitude ($EKE_g < 0.05$ m$^2$ s$^{-2}$). Both $EKE_{C,30h}$ and $EKE_g$ show enhanced values in winter and spring, when multiple mesoscale vortices propagate through the mooring array, captured by AVISO SLA (not shown).

Additional understanding of the physical processes at the OSMOSIS study region can be gained by computing frequency spectra of the observed variables. Spectra of the horizontal velocity $u_{raw}$ and $v_{raw}$ at the central mooring (Figures. 3.2a-b) display high-energy peaks at the $M_2$ semi-diurnal tidal frequency and at the inertial frequency $f$, which make up a large fraction of the unbalanced KE in the region. Near-inertial flows are visible as a broad peak around $f$ and decrease in magnitude with depth. $M_2$ signals appear as a sharp peak, and have a higher spectral energy density than near-

inertial signals. These features are also evident in spectra of potential density $\rho_{raw}$ (Figure 3.2c). All spectra exhibit enhanced energy near the surface at temporal scales characteristic of submesoscale flows (i.e. in the time range between the inertial period and ~10 days), consistent with the preferential occurrence of submesoscale turbulence near the ocean surface (Capet et al. 2008b; Klein et al. 2008; Lévy et al. 2012).

While the additional variance observed in the submesoscale band might in part arise from near-inertial flows directly generated by local wind forcing or internal wave energy Doppler-shifted to lower frequencies by mesoscale motions, I find that submesoscale flows are largely in geostrophic balance. This is illustrated by Figure 3.3. The depth-averaged vertical shear, $\left|\frac{\partial U}{\partial z}\right| = \sqrt{(\frac{\partial \boldsymbol{u}}{\partial z})^2 + (\frac{\partial \boldsymbol{v}}{\partial z})^2}$, has a statistically significant correlation with the depth-averaged $\frac{1}{f}|\nabla_h b|_{I,30h}$, calculated from the inner cluster ($R$ = 0.91, $p$ < 0.001). A slightly weaker, significant correlation is also observed with $\frac{1}{f}|\nabla_h b|_{O,30h}$ calculated from the outer cluster ($R$ = 0.79, $p$ < 0.001). These correlations suggest that the inertial to 10-day variance is likely associated with submesoscale motions that are largely in geostrophic balance.

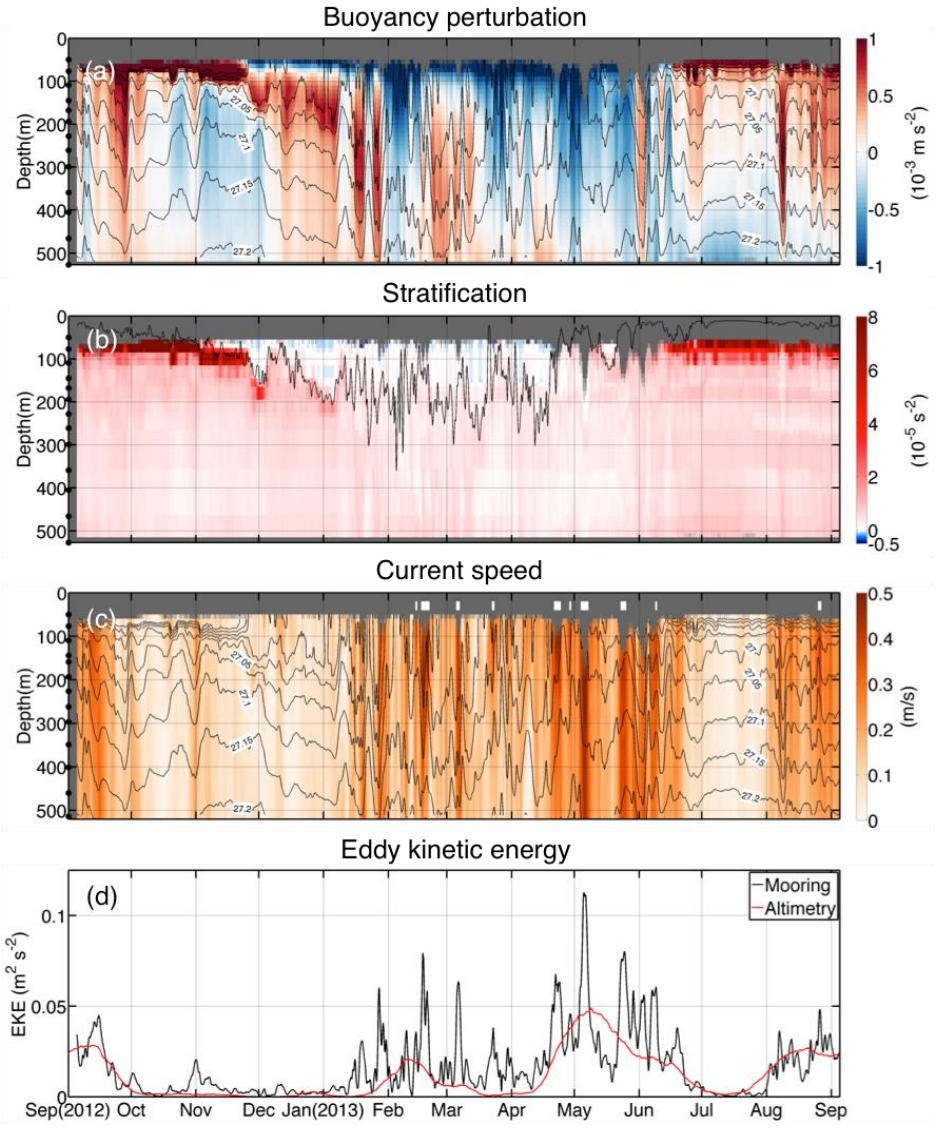


Figure 3.1: Time series of (a) buoyancy perturbation $b'_{C,30h}$, (b) stratification $N^2_{C,30h}$, (c) current speed $U_{C,30h}$, and (d) eddy kinetic energy $EKE_{C,30h}$ (black) and $EKE_g$ (red) at the central mooring site. Isopycnals are overlaid as black lines at intervals of 0.05 kg m$^{-3}$ in (a) and (c), ranging from 26.90 to 27.20 kg m$^{-3}$. Black lines in (b) indicate the MLD. White blocks in (c) indicate time periods with current speed larger than 0.4 m s$^{-1}$. Depths not sampled by the deployed instrumentation in (a-c) are colored in grey.

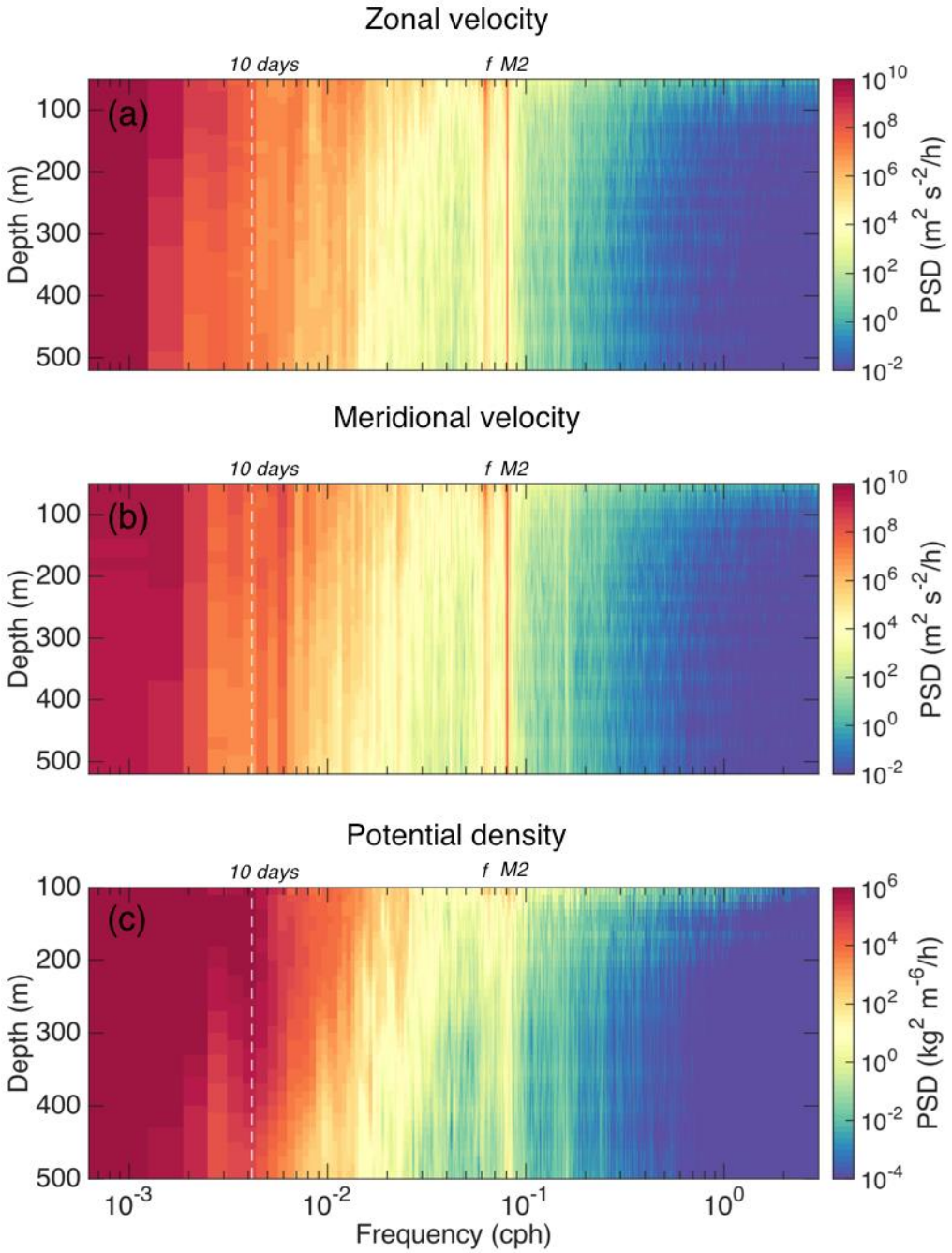


Figure 3.2: Frequency spectra of (a) zonal $u_{raw}$, (b) meridional $v_{raw}$ components of the velocity, and (c) potential density $\rho_{raw}$ at the central mooring as a function of depth. Signals have been linearly detrended. The 10 days, $M_2$ tidal and inertial periods are marked on the upper axis. The 10 days period is also indicated by the white dashed line.

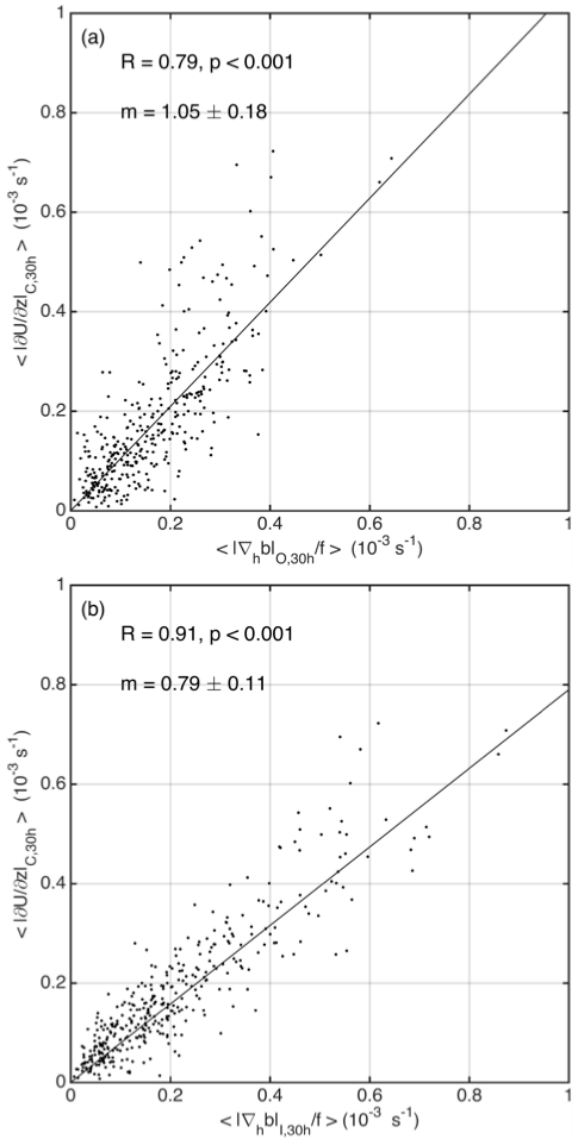


Figure 3.3: Daily vertical shear $\left|\frac{\partial U}{\partial z}\right|_{C,30h}$ plotted against (a) $\frac{1}{f}|\nabla_h b|_{O,30h}$ and (b) $\frac{1}{f}|\nabla_h b|_{I,30h}$ with respective best-fit linear regression lines shown. $m$ is the slope of the linear regression with $\pm$ 95% confidence intervals estimated by a bootstrapping method as noted in the text. Fields are below the mixed layer and depth-averaged.

### 3.4.2 Annual cycle of upper-ocean vertical velocity

The time series of outer and inner vertical velocities inferred from the OSMOSIS moorings are displayed in Figures 3.4a-c and 3.5a-c, after smoothing with a 1-day running mean to facilitate inter-comparison. The diagnosed inner vertical velocity, with RMS ($\langle w_{CI,16h} \rangle$) = 20.7 $\pm$ 10.9 m/day, is substantially larger than the outer vertical velocity, with RMS ($\langle w_{CO,30h} \rangle$) = 9.8 $\pm$ 6.3 m/day. Such highly variable vertical flows are primarily associated with the regular occurrence of mesoscale and submesoscale

features within the mooring array, and are the sum of the contributions from heaving of isopycnals, $w_t$, and flow along inclined isopycnals, $w_h$.

The two components of (outer or inner) vertical velocity, $w_t$ and $w_h$, are comparable in magnitude, but are often oppositely signed (Figures 3.4a-b and 3.5a-b). The $\langle (w_t)_{C,30h} \rangle$ and $\langle (w_t)_{C,16h} \rangle$ terms are highly coherent in depth, while the $\langle (w_h)_{CO,30h} \rangle$ and $\langle (w_h)_{CI,16h} \rangle$ terms occasionally change sign with depth (e.g., at the end of April and in August). This lack of vertical coherence is more common in $\langle (w_h)_{CI,16h} \rangle$ compared to $\langle (w_h)_{CO,30h} \rangle$, and may in part be attributable to mooring motion.

Vertical velocities associated with flows of both horizontal scales are generally larger in magnitude and more variable in winter and spring than in fall and summer (Figures 3.4c and 3.5c). Intense vertical flows during fall and summer are intermittent, and often elevated during the passage of eddy features associated with steep isopycnal slopes, for example in early August.

Annual-mean vertical velocities (Figures 3.4d-f and 3.5d-f) indicate that the site is characterized by weak downwelling of less than 10 m/day, which arises as a small residual of the highly variable vertical flow. This point is evidenced by the fact that the annual-mean vertical velocities (-3.9 m/day and -2.8 m/day for depth-averaged $\overline{\langle w_{CI,16h} \rangle}$ and $\overline{\langle w_{CO,30h} \rangle}$, respectively) are approximately a factor of 5 smaller than their RMS values ($20.7 \pm 10.9$ m/day and $9.8 \pm 6.3$ m/day for $\langle w_{CI,16h} \rangle$ and $\langle w_{CO,30h} \rangle$, respectively). Both outer and inner annual-mean vertical velocities are dominated by the horizontal advection term, $\overline{\langle (w_h)_{CO,30h} \rangle}$ and $\overline{\langle (w_h)_{CI,16h} \rangle}$, with $\overline{\langle (w_t)_{C,30h} \rangle}$ and $\overline{\langle (w_t)_{C,16h} \rangle}$ being much closer to zero. This result is consistent with the work of Sévellec et al. (2015) in the Southern Ocean, where the time-mean vertical motion in the deep Drake Passage was found to be primarily determined by the horizontal advection term, shaped by the underlying topography via stratified Taylor column dynamics. We have examined the possibility that a similar mechanism is at play in our study area by considering the vertical scale over which stratified Taylor column dynamics may be influential (Huppert 1975), and found that topographic effects are most likely insignificant in the uppermost 500 m (in which our measurements were acquired) of the ~4300 m-deep water column.

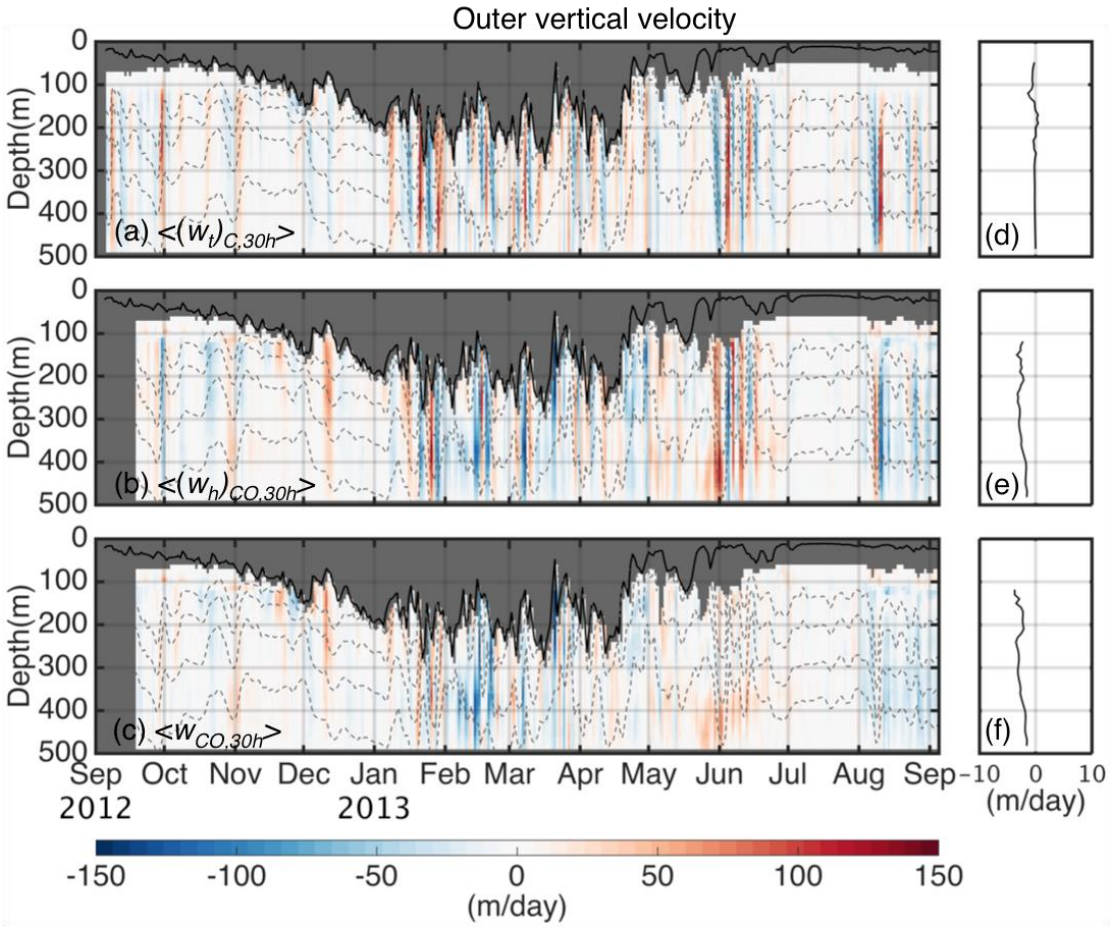


Figure 3.4: Time series of the daily-averaged outer vertical velocity and its components in m/day, (a) $\langle(w_t)_{C,30h}\rangle$ term, (b) $\langle(w_h)_{CO,30h}\rangle$ term and (c) $\langle w_{CO,30h}\rangle$ at the central mooring. A positive value indicates upwelling. The MLD is superimposed as a black line. Isopycnals are overlaid as grey dashed lines. Missing values in the calculations are colored in grey. (d-f) show time-mean values of outer vertical velocity corresponding to (a-c).

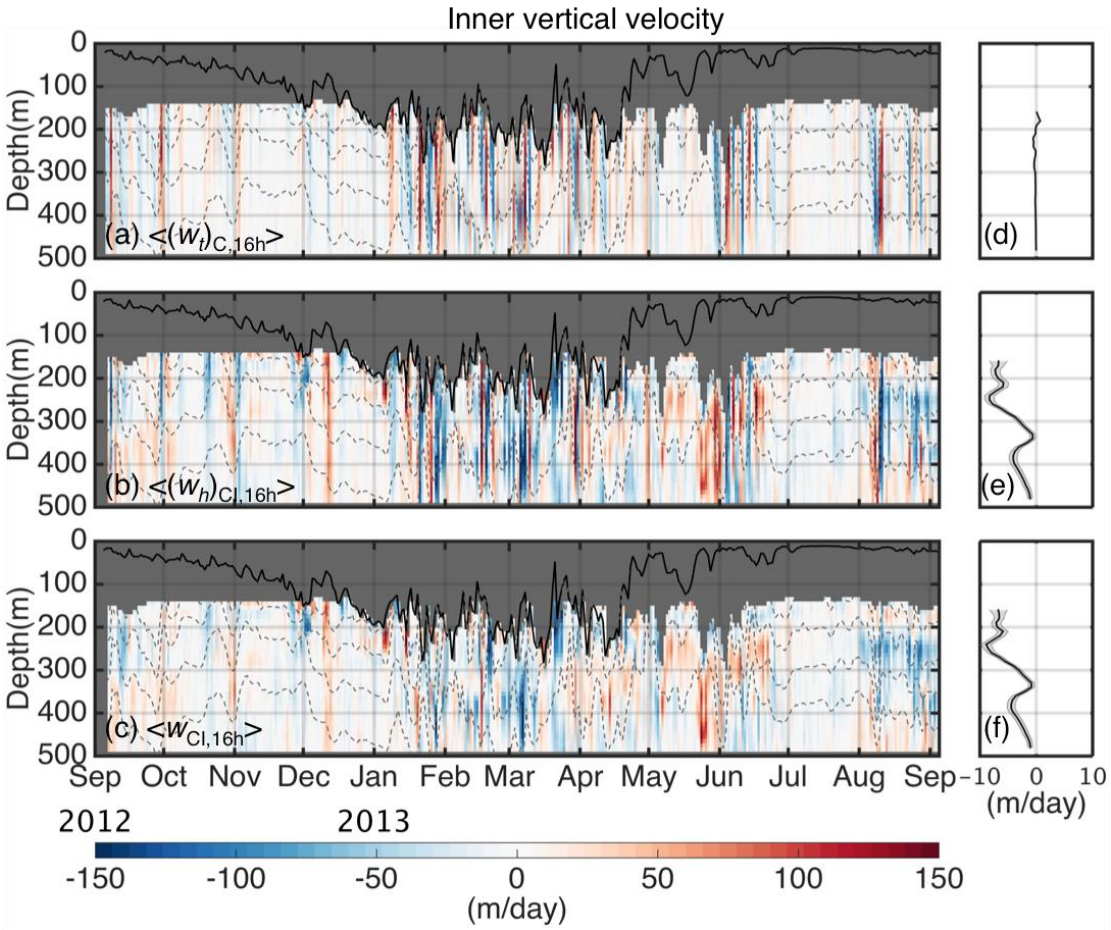


Figure 3.5: Same as Figure 3.4, but for inner vertical velocity. The grey shaded regions in (e) and (f) illustrate the 90% confidence envelope of time-mean vertical velocity, estimated using a Monte Carlo approach.

### 3.4.3 Annual cycle of upper-ocean vertical buoyancy flux

The time series of outer and inner vertical buoyancy flux ($\langle w'_{CO,30h} b'_{C,30h} \rangle$ and $\langle w'_{CI,16h} b'_{C,16h} \rangle$) are shown in Figure 3.6, having being smoothed with a one-day running mean as in the previous subsection. The RMS of these vertical fluxes of buoyancy is O($10^{-7}$ m$^2$ s$^{-3}$), with peak values of O($10^{-6}$ m$^2$ s$^{-3}$) occurring frequently in winter and spring. The magnitude of the buoyancy perturbation $b'_{C,30h}$ (Figure 3.1a) does not vary significantly with season. Thus, the seasonal modulation of the vertical buoyancy flux results from the variation of vertical velocity. Accordingly, $\langle w'_{CO,30h} b'_{C,30h} \rangle$ and $\langle w'_{CI,16h} b'_{C,16h} \rangle$ during winter and spring (i.e. at times in which the vertical velocity is enhanced) dominate restratification of the upper ocean. $\langle w'_{CO,30h} b'_{C,30h} \rangle$ and $\langle w'_{CI,16h} b'_{C,16h} \rangle$ are more intermittent during fall and summer, when they appear to be closely tied to a small number of mesoscale events (e.g., those

on 4-9 June or 6-11 August). Recall that my estimates of vertical velocity are founded on the assumption of negligible diffusive mixing below the ML. Since background thermocline mixing (at a rate of $\kappa \approx 3\times10^{-5}$ m$^2$ s$^{-1}$; Ledwell et al. 1993) would induce a vertical buoyancy flux of $\kappa b_z \approx 3\times10^{-5}$ m$^2$ s$^{-1}$ $\times$ $1.3\times10^{-5}$ s$^{-2}$ $\approx 4\times10^{-10}$ m$^2$ s$^{-3}$ (where $b_z \approx 1.3\times10^{-5}$ s$^{-2}$ is a characteristic value measured by our mooring array) that is much smaller than $\langle w'_{CO,30h} b'_{C,30h} \rangle$ and $\langle w'_{CI,16h} b'_{C,16h} \rangle$, our results are consistent with our starting assumption.

To assess the net contribution of the eddy-induced vertical buoyancy fluxes to the local climatological upper-ocean stratification, vertical profiles of the annual-mean (outer and inner) equivalent heat fluxes are computed from Equation 3.5, and compared with the destratification induced by the annually integrated atmospheric cooling of the area. The annual-mean outer equivalent heat flux $\overline{Q_w}$ (Figure 3.7a) is consistently positive and attains a maximum value of approximately 20 W m$^{-2}$. The amplitude of outer $\overline{Q_w}$ decreases gently with depth. In contrast, the annual mean of the inner equivalent heat flux $\overline{Q_w}$ (Figure 3.7b) is larger and more surface-intensified, reaching 90 W m$^{-2}$ above 250 m. This vertical range coincides with that in which spectra of horizontal velocity and density show elevated energy at submesoscale frequencies (Figure 3.2). Below 250 m, outer and inner $\overline{Q_w}$ are similar in magnitude and vertical structure. As the annual-mean surface heat flux is approximately -45 W m$^{-2}$ and so comparable to the annual-mean inner equivalent heat flux, this result suggests that submesoscale flows contribute importantly to upper-ocean restratification, even in relatively quiescent mid-ocean areas such as the OSMOSIS site.

To conclude, it is notable that, as was the case for the annual-mean vertical velocity (Figures 3.4d-f and 3.5d-f), the annual-mean vertical buoyancy flux is also dominated by the horizontal advection term ($Q_{w_h}$) at both horizontal scales. By contrast, the annual-mean ($Q_{w_t}$) term is close to zero. As $\langle (w_t)_{C,30h} \rangle$ and $\langle (w_t)_{C,6h} \rangle$ are aligned orthogonal to isopycnal surfaces, the vertical transport of buoyancy related to this term does not induce net restratification in the long term.

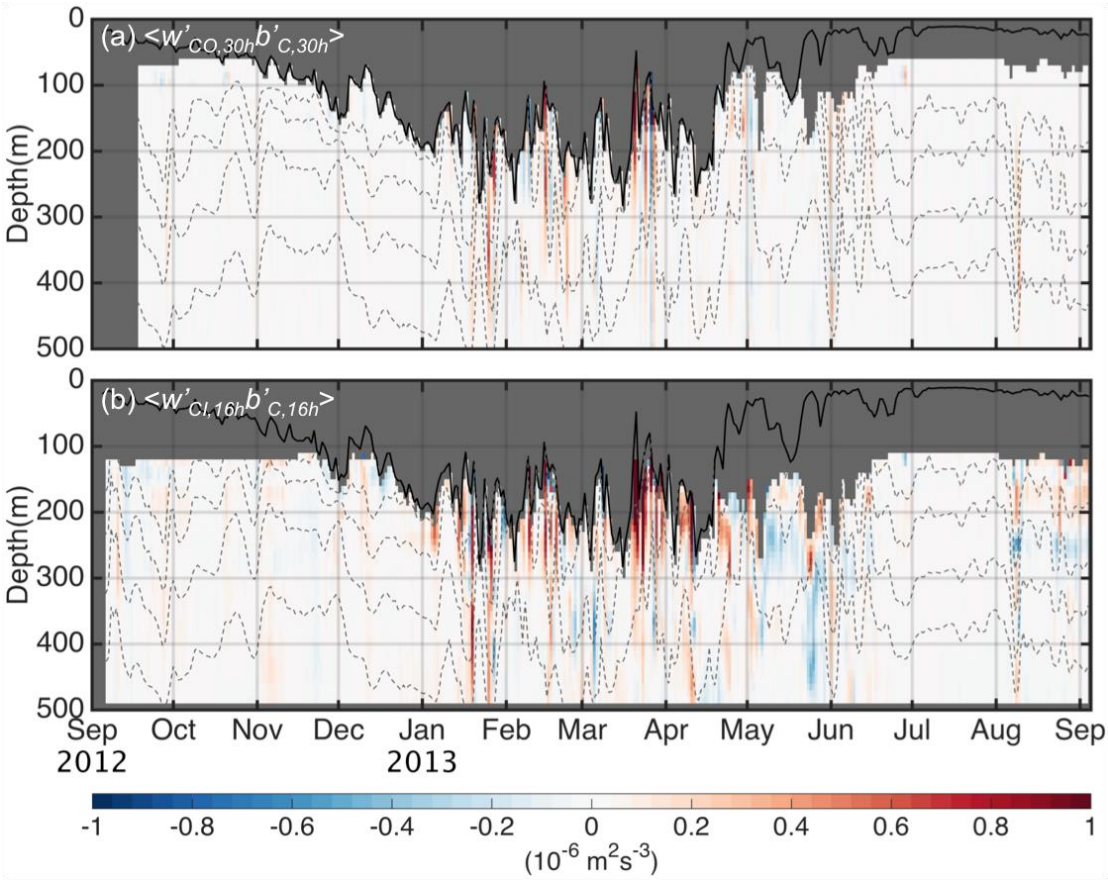


Figure 3.6: Year-long time series of daily-averaged vertical buoyancy flux at (a) mesoscale (outer) $\langle w'_{CO,30h} b'_{C,30h} \rangle$ and (b) submesoscale (inner) $\langle w'_{CI,6h} b'_{C,6h} \rangle$ from the central mooring. The black line represents the MLD. Isopycnals are overlaid as grey dashed lines. Missing values are colored in grey.

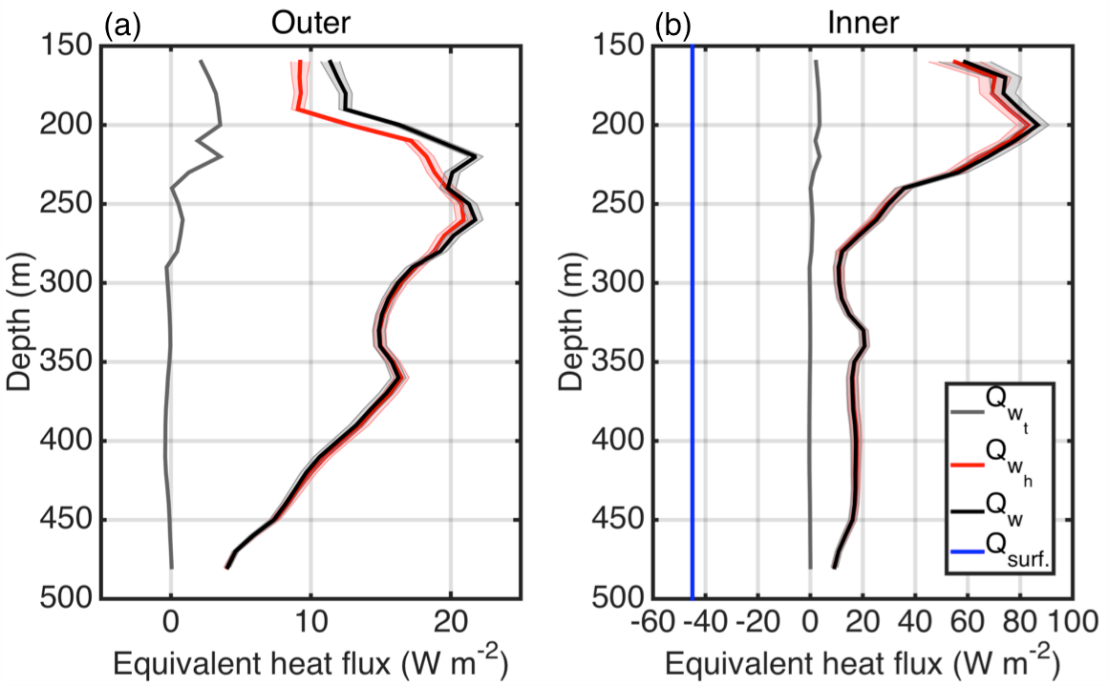


Figure 3.7: Year-mean equivalent heat flux calculated at (a) mesoscales (outer) and (b) submesoscales (inner). The total equivalent heat flux $Q_w$ is shown by the black line. Its two components ($Q_{w_t}$ and $Q_{w_h}$) are indicated by the grey and red lines, respectively. The surface equivalent heat flux $Q_{surf.}$ is shown by the blue line as a reference. The red and black shaded regions in (b) illustrate the respective 90% confidence envelope of time-mean $Q_{w_h}$ and $Q_w$, estimated using a Monte Carlo approach.

### 3.4.4 Annual cycle of frontogenesis and lateral buoyancy gradients

Using the year-long time series provided by the OSMOSIS moorings, I document the probability distribution function (PDF) of the depth-averaged outer frontogenesis function, $Fs_{O,30h}$, in different seasons (Figure 3.8a). The dominant feature is the marked asymmetry between frontogenesis (i.e. positive $Fs_{O,30h}$) and frontolysis (i.e. negative $Fs_{O,30h}$) during winter and spring, when frontogenetic processes are intensified (with $Fs_{O,30h}$ exceeding $1\times10^{-20}$ s$^{-5}$, or $Fs_{O,30h}/f^5 = 0.63$) relative to frontolytic processes, albeit for less than 15% of the time. Over 95% of the values of $Fs_{O,30h}$ during the fall and summer are in the range of $-0.4\times10^{-20}$ to $0.4\times10^{-20}$ s$^{-5}$ ($Fs_{O,30h}/f^5 = 0.25$). The decorrelation time scale of $Fs_{O,30h}$ over the annual cycle of measurements is roughly 2 days. Overall, the increase in the probability of observing positive $Fs_{O,30h}$ in winter and spring over that in fall and summer suggests the occurrence of a seasonal cycle in the rate of mesoscale frontogenesis in the upper ocean.

Representative winter and spring times series of $Fs_{O,30h}$, $|\nabla_h b|_{I,30h}$ and $|\nabla_h b|_{O,30h}$ are shown in Figures 3.8b-d. The magnitude of $|\nabla_h b|_{I,30h}$ is generally a factor of 2 larger than that of $|\nabla_h b|_{O,30h}$, with typical values on the order of $10^{-7}$ s$^{-2}$. The decorrelation time scale of $|\nabla_h b|_{I,30h}$ is approximately 3 days. High $Fs_{O,30h}$ events correspond to inner lateral buoyancy gradients, $|\nabla_h b|_{I,30h}$, that are enhanced to a greater extent than outer lateral buoyancy gradients, $|\nabla_h b|_{O,30h}$. Positive $Fs_{O,30h}$ values display a significant positive trend with $|\nabla_h b|_{I,30h}$ in log space (Figure 3.9a). These results are consistent with an active generation of submesoscale fronts (defined as areas of elevated lateral density gradient with horizontal scales of 1-10 km) by mesoscale frontogenesis (Figure 3.9b). Notably, the vertical extent of the enhancement of $|\nabla_h b|_{I,30h}$ associated with $Fs_{O,30h}$ exceeds the MLD (Figures 3.8b-c). This may reflect the vertical extent of the ageostrophic secondary circulation required to restore thermal wind balance as frontogenesis unfolds (Thomas and Ferrari 2008).

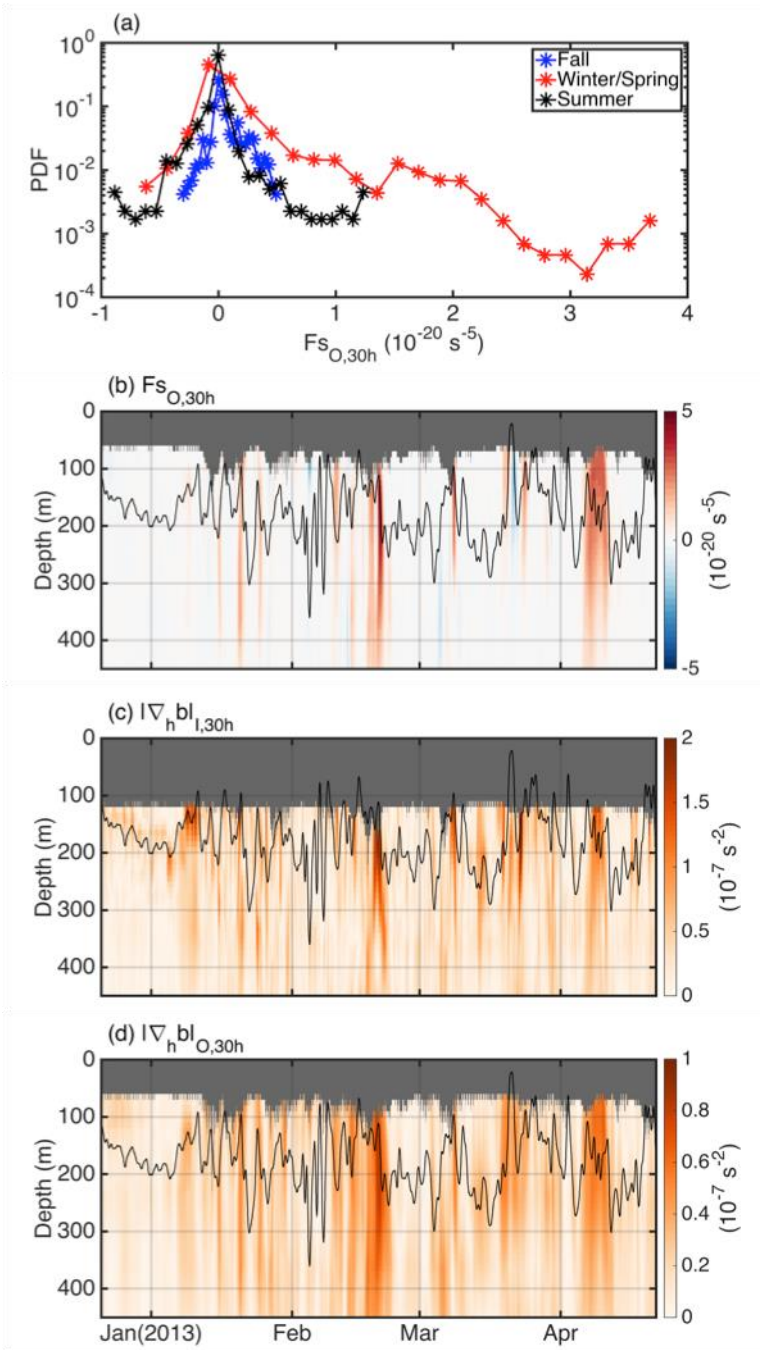


Figure 3.8: (a) Histogram of depth-averaged outer frontogenesis function $Fs_{O,30h}$. Representative winter and spring times series of (b) outer frontogenesis function $Fs_{O,30h}$, (c) inner lateral buoyancy gradient $|\nabla_h b|_{I,30h}$ and (d) outer lateral buoyancy gradient $|\nabla_h b|_{O,30h}$at the central mooring site. The black line in (b-d) shows the MLD. Missing values are colored in grey.

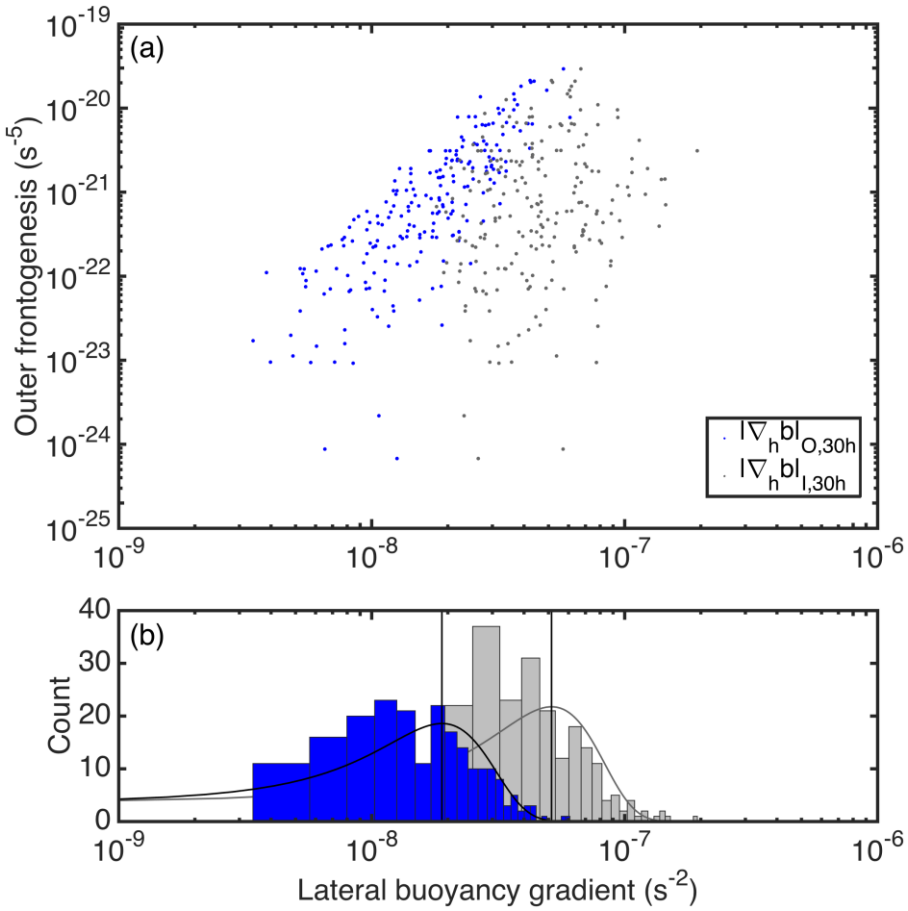


Figure 3.9: (a) Scatterplot of daily values of outer frontogenesis (i.e., $Fs_{O,30h} > 0$) against (blue) outer and (grey) inner lateral buoyancy gradients. Fields are below the mixed layer and depth-averaged. (b) Histograms of (blue) outer and (grey) inner lateral buoyancy gradients, with respective mean values and Normal distribution fits displayed.

## 3.5 Discussion

### 3.5.1 Mechanisms inducing submesoscale vertical motion and restratification

In the previous section, the vertical velocity and buoyancy flux associated with submesoscale motions are shown to be substantially larger than those associated with mesoscale flows. I now consider the possible mechanisms underpinning this result.

Both the outer and inner vertical velocities broadly follow the annual cycle of $EKE_{C,30h}$ at the central mooring (Figures 3.1d and 3.10a). Inner vertical velocity is modest at times of weak mesoscale eddy activity (e.g., in July, with an RMS of 11.3 $\pm$ 2.0 m/day), but is elevated when energetic mesoscale features propagate through the mooring array (e.g., in February, with an RMS of 40.0 $\pm$ 9.7 m/day). I find that most of the enhanced inner vertical velocity events coincide with large values of $\langle EKE_{C,30h} \rangle$ (Figure 3.10b), yielding a statistically significant correlation coefficient between daily

$EKE_{C,30h}$ and daily RMS $\langle w_{CI,16h} \rangle$ of 0.66. This suggests that the presence of mesoscale features may play a role in energising submesoscale flows with pronounced vertical velocity signatures. Outer $\langle w_{CO,30h} \rangle$ also exhibits a positive correlation with $\langle EKE_{C,30h} \rangle$, yet its magnitude ($R$ = 0.44, $p$ < 0.001) is lower than for inner $\langle w_{CI,16h} \rangle$.

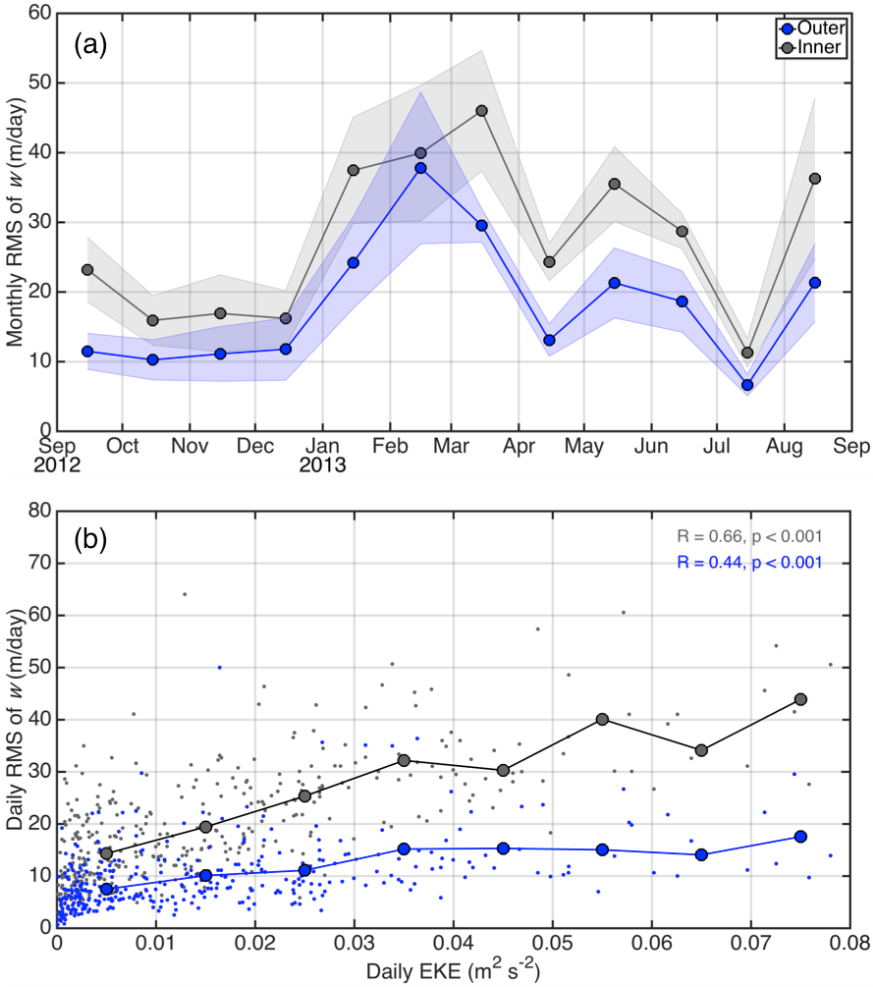


Figure 3.10: (a) Root mean square of vertical velocity at mesoscale (outer) and submesoscale (inner) throughout the year. The standard deviation is shown by the light shades. (b) Daily root mean square of vertical velocity (dots) as a function of EKE. The mean values of RMS of vertical velocity, discretized in 0.01 $m^2$ $s^{-2}$ EKE bins, for mesoscale (blue) and submesoscale (grey) are given by the circles.

Mesoscale frontogenesis is a potentially significant player in shaping upper-ocean stratification within and below the base of MLD. In the OSMOSIS site, vertical velocity beneath the mixed layer is enhanced in the presence of prominent mesoscale eddies, suggesting that ageostrophic secondary circulations induced by mesoscale frontogenesis are an important contributor to upper-ocean vertical flow. As mentioned

in Section 3.3.2, a further 30-hour low-pass filter was applied to inner variables in investigating the relationship between submesoscale turbulence and mesoscale forcing. I find that the magnitude of inner $w'^2_{CI,30h}$and associated restratification (i.e. positive $w'_{CI,30h}b'_{C,30h}$) exhibit significant positive correlations with the inner lateral buoyancy gradient, $|\nabla_h b|_{I,30h}$, and with the outer frontogenesis function, $Fs_{O,30h}$ (Figure 3.11). This is consistent with the predictions of modeling studies on the regulatory role of mesoscale frontogenesis on submesoscale turbulence (Capet et al. 2008b). These positive correlations are shown to be significant by a bootstrap method.

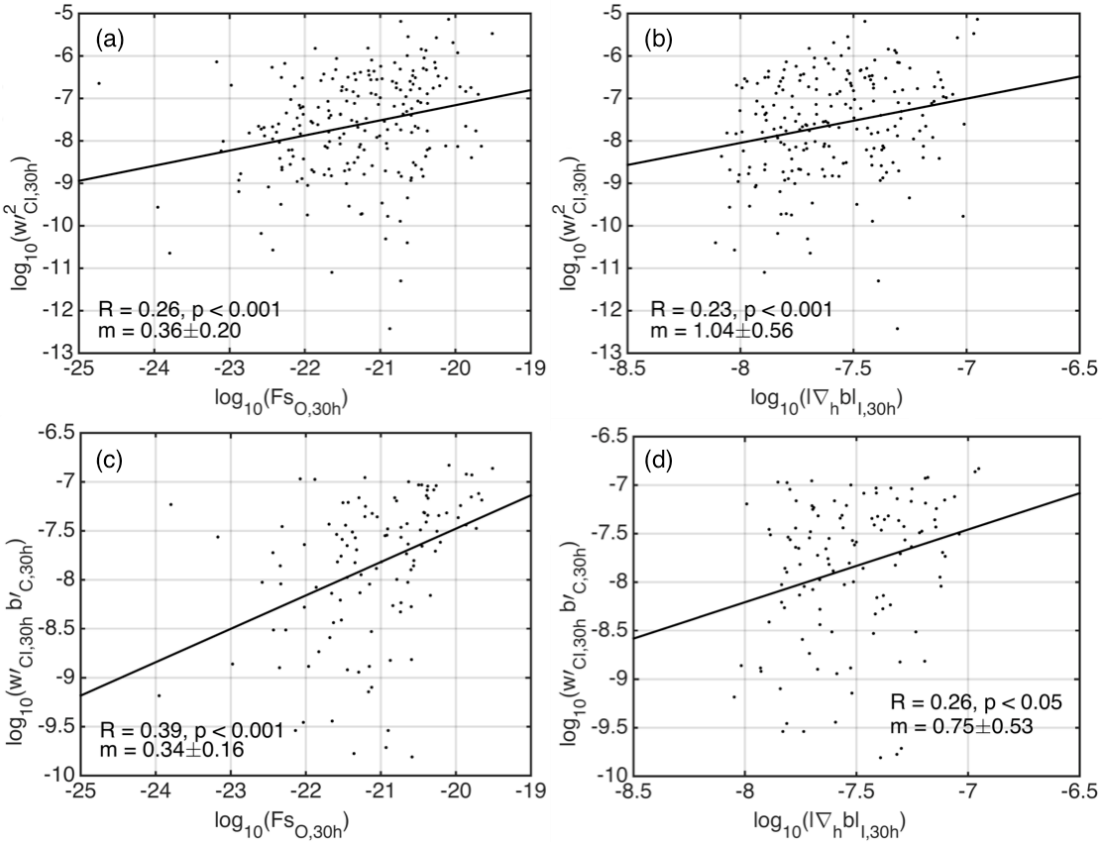


Figure 3.11: Regression relationship between (a) $\langle w'^2_{CI,30h}\rangle$ and $\langle Fs_{O,30h}\rangle$, (b) $\langle w'^2_{CI,30h}\rangle$ and $\langle|\nabla_h b|_{I,30h}\rangle$ , (c) $\langle w'_{CI,30h}b'_{C,30h}\rangle$ and $\langle Fs_{O,30h}\rangle$ , (d) $\langle w'_{CI,30h}b'_{C,30h}\rangle$ and $\langle|\nabla_h b|_{I,30h}\rangle$. Black lines in (a-d) show linear regression fits. $m$ is the slope of the linear regression with $\pm$ 95% confidence intervals estimated by a bootstrapping method as noted in the text.

Frontogenesis has been indicated by numerical simulations to be most pronounced in a thin surface boundary layer, and to decay rapidly below this layer (Lapeyre et al. 2006; Capet et al. 2008b). Our observational results present a somewhat different

picture, in which mesoscale frontogenetic processes and intensified submesoscale lateral buoyancy gradients are found well beneath the mixed layer, particularly during winter and spring. The sharp and deep submesoscale lateral buoyancy gradients and relatively weak stratification across the mixed layer base (Figure 3.1b) provide an environment that is optimally suited for the potential development of submesoscale turbulence throughout the upper ocean by submesoscale BCI (Capet et al. 2016).

The notable vertical penetration of submesoscale flows is illustrated by the structure of the Rossby and balanced Richardson numbers calculated from the outer and inner arrays, shown in Figure 3.12. The Rossby number is generally surface-intensified, yet decays only gradually with depth. The inner Rossby number, $\zeta_{I,30h}/f$, is in the range of -0.8 – 0.8, a factor of 2 larger than the outer Rossby number, $\zeta_{O,30h}/f$. The Rossby number substantially exceeds 0 down to 500 m depth, especially for the inner cluster, suggesting that strong ageostrophic secondary circulations may extend beyond the ML base. Small values (< 5) of the inner balanced Richardson number are often observed below the ML, and indicate that submesoscale processes may be intensified in episodes of strong lateral buoyancy gradients and relatively weak vertical stratification. In contrast, the outer balanced Richardson number consistently and considerably exceeds the inner balanced Richardson number below the ML.

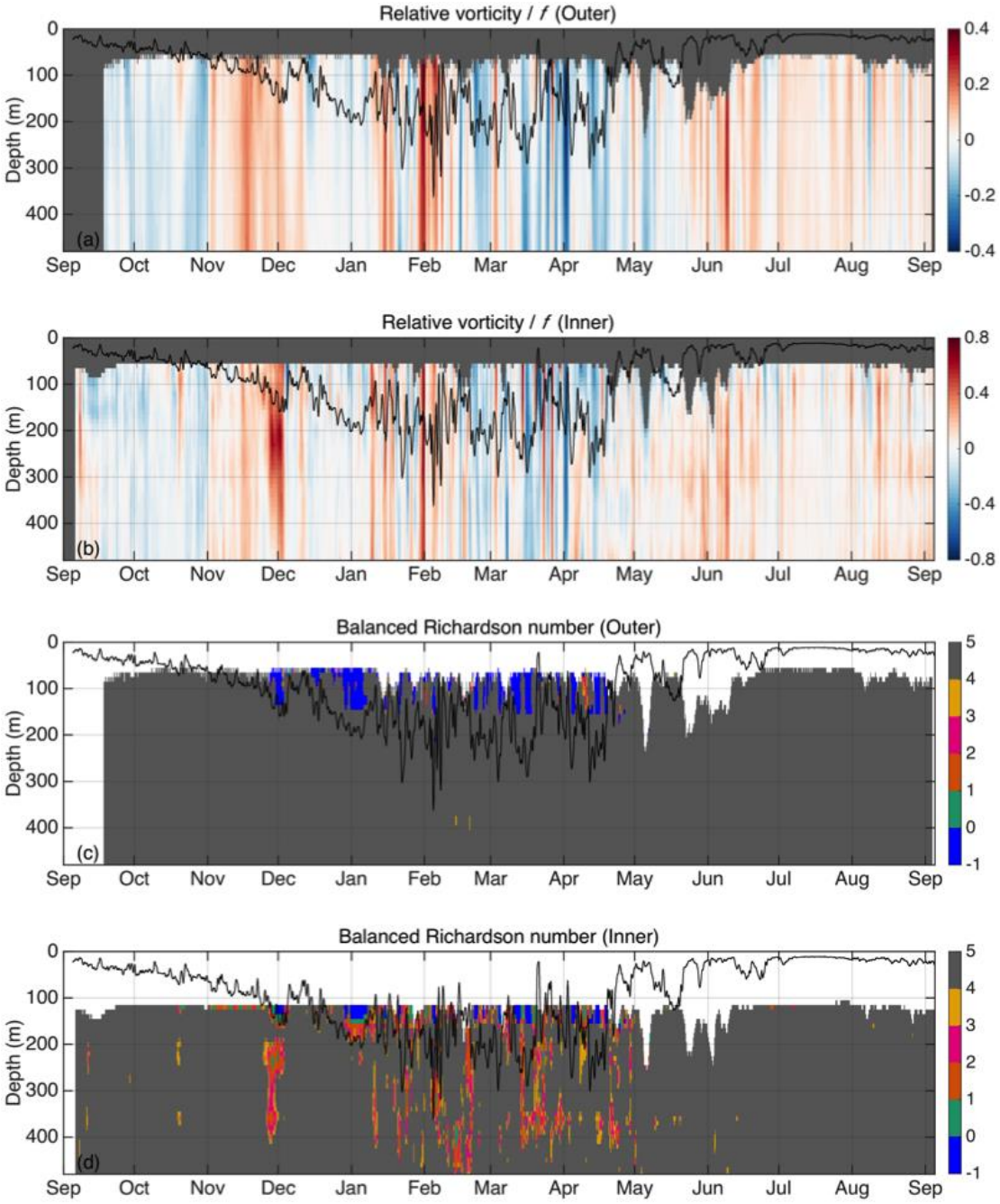


Figure 3.12: Time series of (a) outer Rossby number $\zeta_{O,30h}/f$, (b) inner Rossby number $\zeta_{I,30h}/f$, (c) outer Richardson number $f^2N^2_{C,30h}/|\nabla_h b|^2_{O,30h}$ and (d) inner Richardson number $f^2N^2_{C,30h}/|\nabla_h b|^2_{I,30h}$ at the central mooring. The black line represents the MLD. Missing values in (a-b) are colored in grey.

To synthesise the relationship between the generation of upper-ocean submesoscale turbulence and the occurrence of mesoscale frontogenesis in the OSMOSIS area, I

conducted an analysis of the relationship of $w'^2_{CI,30h}$ and $w'_{CI,30h}b'_{C,30h}$ with $Fs_{O,30h}$ and $|\nabla_h b|_{I,30h}$, shown in Figures 3.13. Inner vertical velocity and buoyancy flux are clearly enhanced when both of $Fs_{O,30h}$ and $|\nabla_h b|_{I,30h}$ are elevated. Persistent frontogenesis induced by the mesoscale strain field is common to periods of large submesoscale horizontal buoyancy gradient and enhanced upper-ocean restratification. This is consistent with mesoscale frontogenesis being a regular precursor of restratifying submesoscale instabilities, and thus suggests that it is likely an important mechanism in generating the observed submesoscale turbulence.

### 3.5.2. Effects of instabilities of balanced flows

Mesoscale BCI is a likely contributor to upper-ocean restratification. This is suggested by the frequent occurrence of a reversal with depth (below the mixed layer base down to ~500 m) of the isopycnal PV gradient (not shown), which is a necessary condition for the development of the instability (Charney and Stern 1962). Below 250 m, my diagnosed outer and inner equivalent heat fluxes exhibit similar patterns, with values approaching 20 W $m^{-2}$ (Figure 3.7). This is indicative of the restratifying action of deep-reaching, slowly-evolving mesoscale eddies in the ocean interior.

Submesoscale instabilities have been argued to be active in the mixed layer, where they can reverse the sign of the equivalent surface heat flux intermittently in the OSMOSIS domain during winter (Thompson et al. 2016). The enhancement of the upper-ocean vertical velocity and buoyancy flux during winter and spring (when upper-ocean stratification is weakest) in my calculations is consistent with this interpretation, as well as with recent simulations of submesoscale BCI (Callies et al. 2016). I thus highlight the likely importance of submesoscale BCI in inducing intense vertical motion and restratification in the upper ocean at the OSMOSIS site.

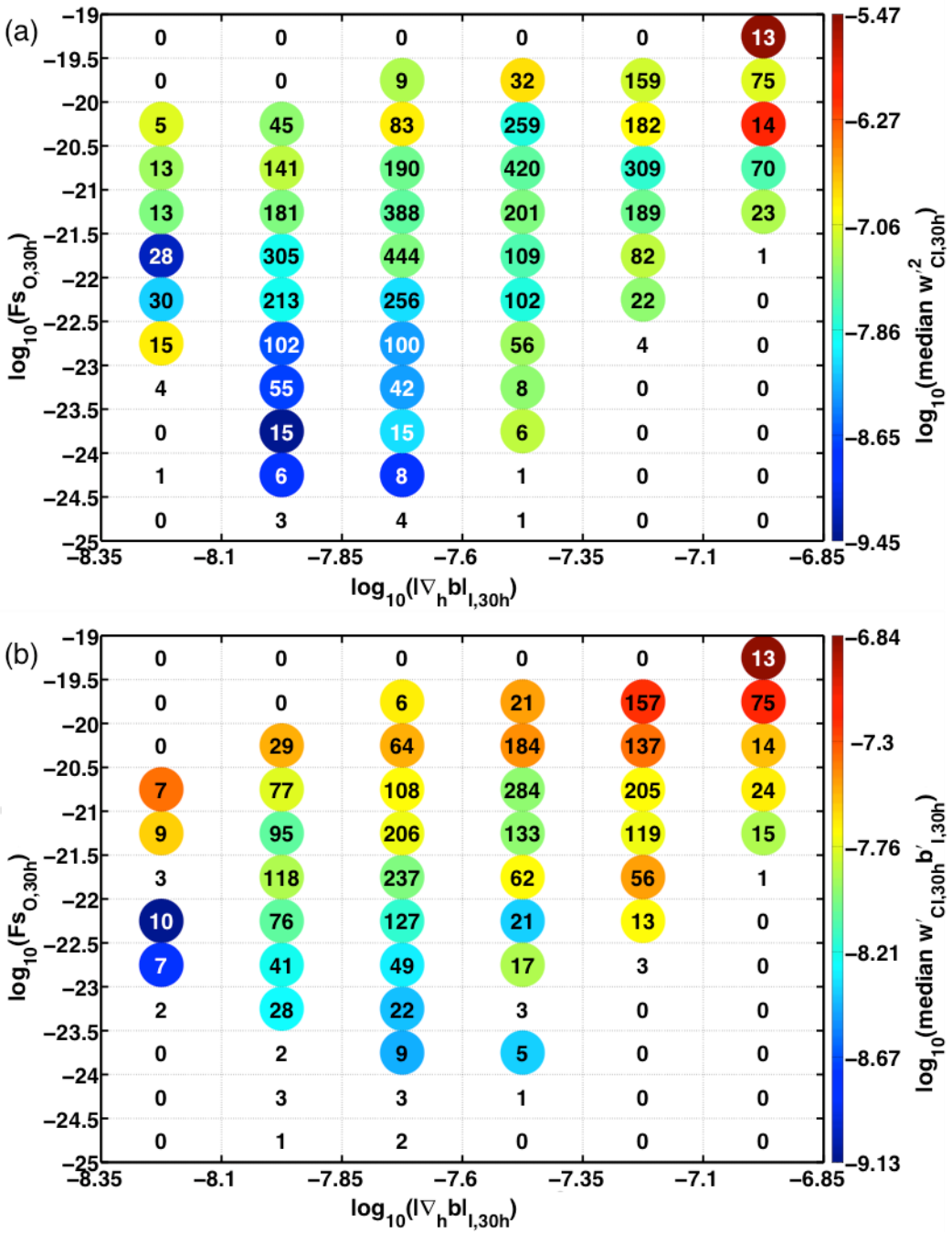


Figure 3.13: Bin-averaged median values of (a) the square of submesoscale vertical velocity perturbation $w'_{CI,30h}$, and (b) the submesoscale vertical buoyancy flux $w'_{CI,30h}b'_{C,30h}$, as a function of depth-averaged submesoscale lateral buoyancy gradient $|\nabla_h b|_{I,30h}$ and mesoscale frontogenesis function $Fs_{O,30h}$. Sample numbers in each bin are indicated in text. Sample numbers $< 5$ are neglected.

## 3.6 Testing the calculation of vertical velocity

### 3.6.1 Testing the calculation of vertical velocity with a numerical model

An idealized doubly-periodic numerical model (Brannigan et al. 2015) is employed to investigate the validity of the non-diffusive density equation used to diagnose vertical motion. The model domain is an analogue of an open ocean region like the OSMOSIS mooring site, where the KE budget is dominated by mesoscale eddies. The model state from a simulation spun up with 4 km horizontal grid resolution is interpolated to a finer resolution of 0.5 km to permit submesoscale instabilities. The model is integrated for 30 days using MITgcm in a hydrostatic configuration, and model outputs are averaged over one inertial period (about 15.9 h) to reduce inertial-gravity wave effects. The model is forced at the surface by wind forcing and a heat flux, but contains no barotropic tides. The surface boundary condition is calculated relative to a uniform zonal 10 m wind speed of 6.3 m $s^{-1}$ to allow eddy-Ekman interactions, and the surface heat flux is a cooling of 75 W $m^{-2}$. A limitation of the model is that the internal wave field is likely to be modest, due to the relatively coarse vertical and horizontal resolutions and smoothly varying surface forcing.

Figure 3. 14a shows the surface temperature at the initial state. The RMS values of vertical motion increase continuously during the model run and the largest values of the vertical velocity below the MLD are of order 10 m $day^{-1}$. Data at 258 m depth (below the maximum MLD) are used to validate my vertical flow calculation method. First, the amplitudes of $w_{DE}$ computed from the non-diffusive density equation (see Equation 3.1) are compared to the $w_{model}$ from simulations. To do so, 100 uniformly distributed data points throughout the model domain are chosen (shown as black dots in Figure 3.14a). The density gradients are calculated on a grid analogous to that of the inner mooring cluster. The absolute minima and maxima in the diagnosed and modeled distributions at each time interval are compared in Figure 3.14b. Generally, $w_{DE}$ matches $w_{model}$ well, and the correlation coefficient between the amplitudes of $w_{DE}$ and $w_{model}$ is 0.76. The slope of the linear fitting line is 1.41, suggesting it is likely that the non-diffusive density equation slightly overestimates the intensity of vertical flow. The overestimation of vertical velocity by applying mass conservation is likely to result from numerical and explicit diffusion in the model. The horizontal distribution of vertical velocity implied by the non-diffusive density equation is compared to the modeled vertical velocity field (Figures 3.14c-d). The similarities between the two

fields suggest that the non-diffusive density equation diagnoses the horizontal distribution of vertical velocity correctly.

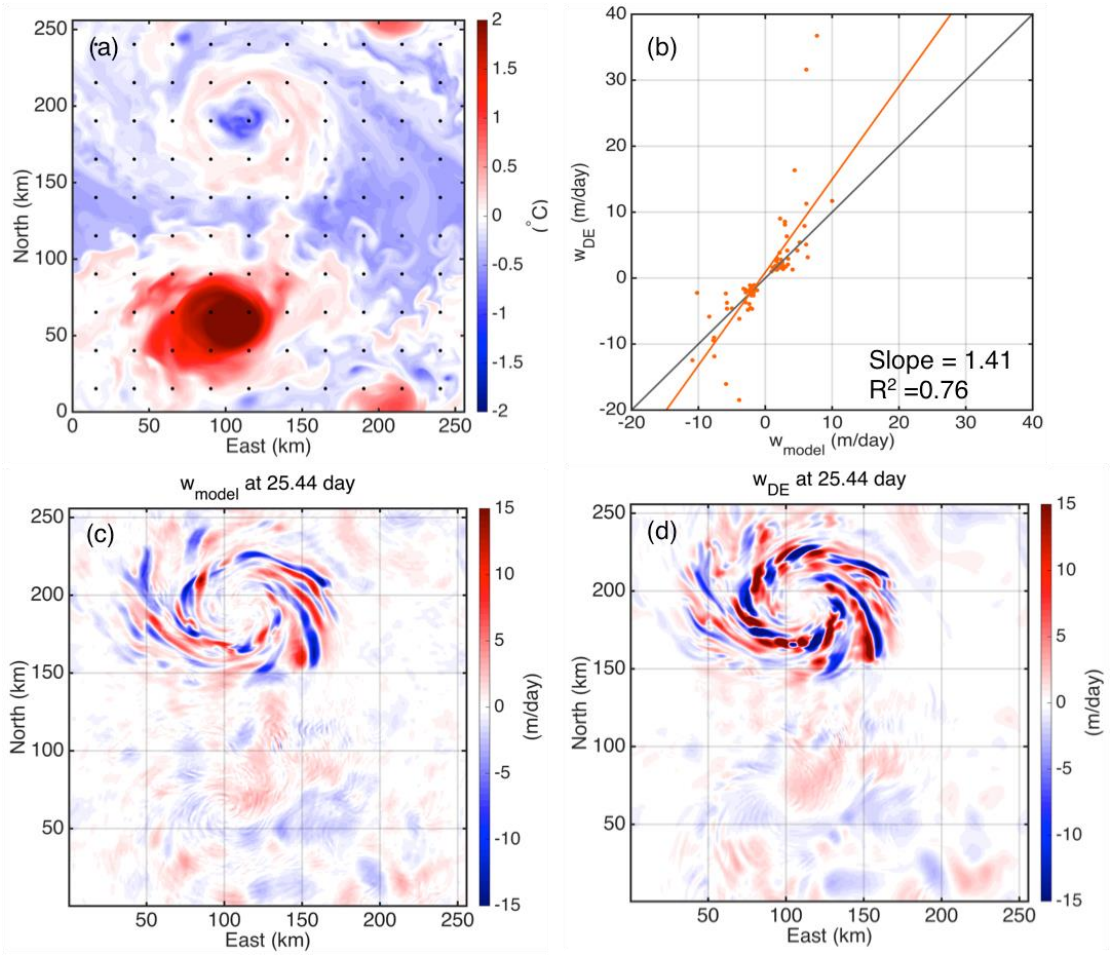


Figure 3.14: (a) Surface temperature anomaly at the initial state of the model simulation. (b) Relationship between the amplitude of the modeled vertical velocity, $w_{model}$, and that of the vertical motion implied by the density conservation equation, $w_{DE}$. The amplitudes (minima and maxima) are extracted from each time interval (i.e. every one inertial period) of the model output at 100 data points, shown as black dots in (a). Reference line with slope 1 is indicated in grey. The horizontal distribution of (c) $w_{model}$ and (d) $w_{DE}$ (d) at a depth of 252 m at day 25.44.

### 3.6.2 Estimation of vertical velocity from individual moorings under the assumption of geostrophic balance

Following Bryden (1980), the $w_h$ term in Equation 3.2 can be expressed as the rotation of the horizontal velocity vector with depth by assuming geostrophic balance,

$$w_{h_g} = -\frac{\frac{f\rho}{g}\left(v\frac{\partial u}{\partial z} - u\frac{\partial v}{\partial z}\right)}{\partial_z \rho} = -\frac{\frac{f\rho}{g}U^2\frac{\partial \phi}{\partial z}}{\partial_z \rho}, \quad (3.12)$$

where $\phi$ is the direction of the flow measured anti-clockwise from east, and $w_{h_g}$ is related to horizontal geostrophic advection. This alternative approach is particularly appropriate for reproducing *w* from a time series of density and horizontal velocity measurements at multiple depth levels from a single mooring. The vertical velocity $\langle w_{g_{CO,30h}} \rangle$ inferred from the central mooring agrees well with $\langle w_{CO,30h} \rangle$ estimated from density equation with best-fit slopes of 0.80 – 1.06 and statistically significant correlation coefficients exceeding 0.70 (Figure 3.15), thereby endorsing our density conservation-based diagnostics.

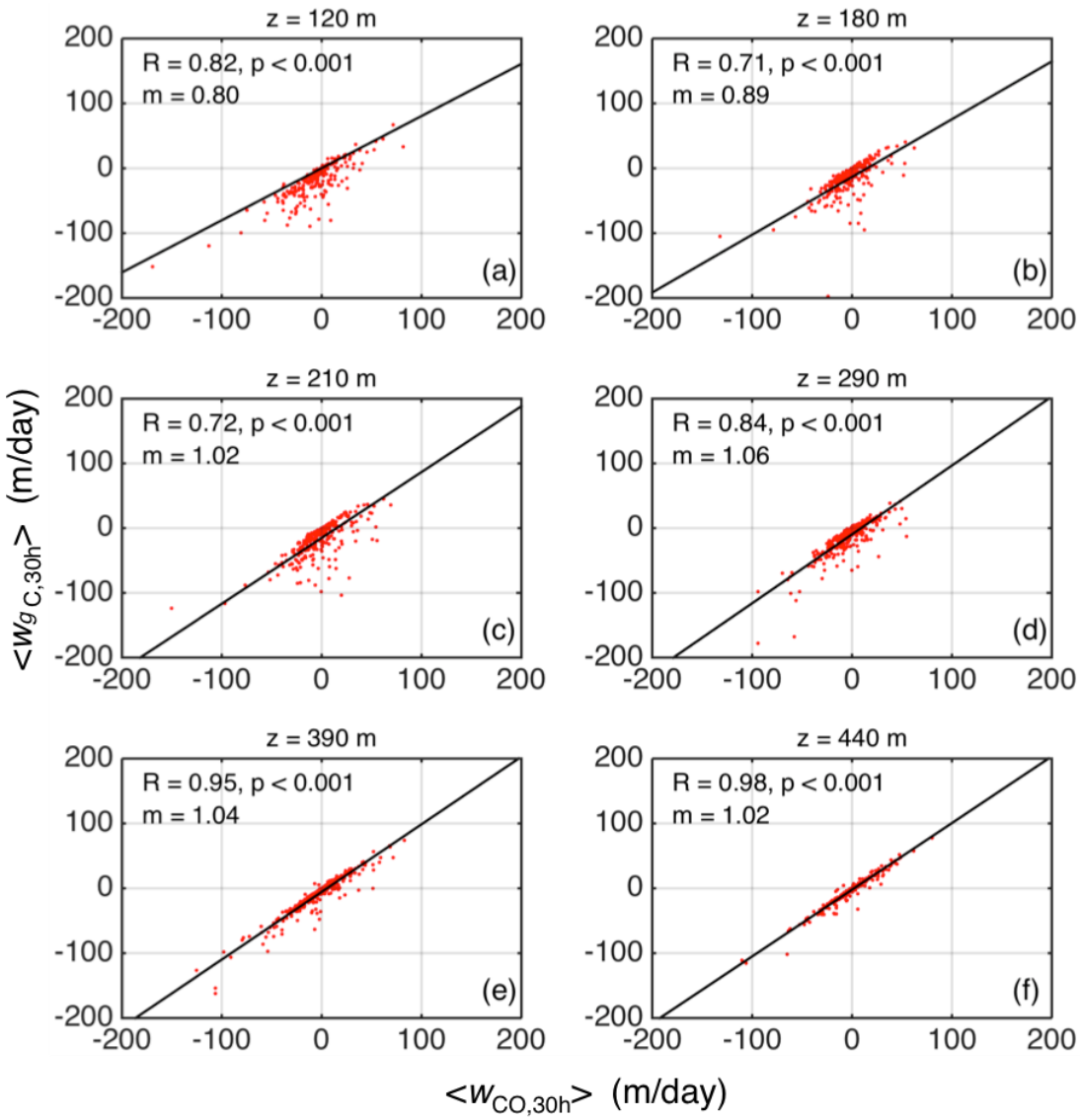


Figure 3.15: Comparison of diagnosed $\langle w_{CO,30h} \rangle$ estimated from the density equation and $\langle w_{g_{C,30h}} \rangle$ estimated from the central mooring measurements only as illustrated in Section 3.6.2. Black lines in (a-f) show linear regression fits. $m$ is the slope of the linear regression and $R$ is the correlation coefficient.

### 3.6.3 Testing the calculation of vertical velocity within the QG framework

The QG omega equation is derived by eliminating the time derivative between the buoyancy equation and the PV equation, and may be used to estimate vertical velocity from 'snapshot' measurements. Following Hoskins et al. (1978), the QG omega equation is expressed as

$$f^2 \frac{\partial^2 w}{\partial z^2} + \left(\frac{\partial^2}{\partial x^2} + \frac{\partial^2}{\partial y^2}\right)(N^2 w) = 2\nabla_h \cdot \vec{Q}. \quad (3.13)$$

We cannot solve the full 3-D elliptic equation for w from the OSMOSIS mooring dataset, as we lack sufficient measurement points to obtain robust estimates of all the spatial derivatives present in Equation 3.13. However, we can exploit the fact that the structure of the vertical velocity is solely determined by the divergence of $\vec{Q}$ in the QG omega equation, such that convergent (divergent) $\vec{Q}$ corresponds to upward (downward) motion (Hoskins et al. 1978; Holton 2004). To estimate the divergence of $\vec{Q}$ at the central mooring site, $\vec{Q}$ is first computed within four triangular regions of the outer mooring domain. In each triangular mooring area, gradients in velocity and buoyancy can be obtained by averaging over the whole triangle. Figure 3.16 shows the time series of the convergence of $\vec{Q}$ (i.e. $-\nabla_h \cdot \vec{Q}_{CO,30h}$) and its correlation coefficient with the outer vertical velocity. The convergence of $\vec{Q}$ closely resembles the pattern of vertical velocity diagnosed from the density conservation equation. Both fields are significantly correlated at the 95% confidence level for all depths, throughout the annual cycle.

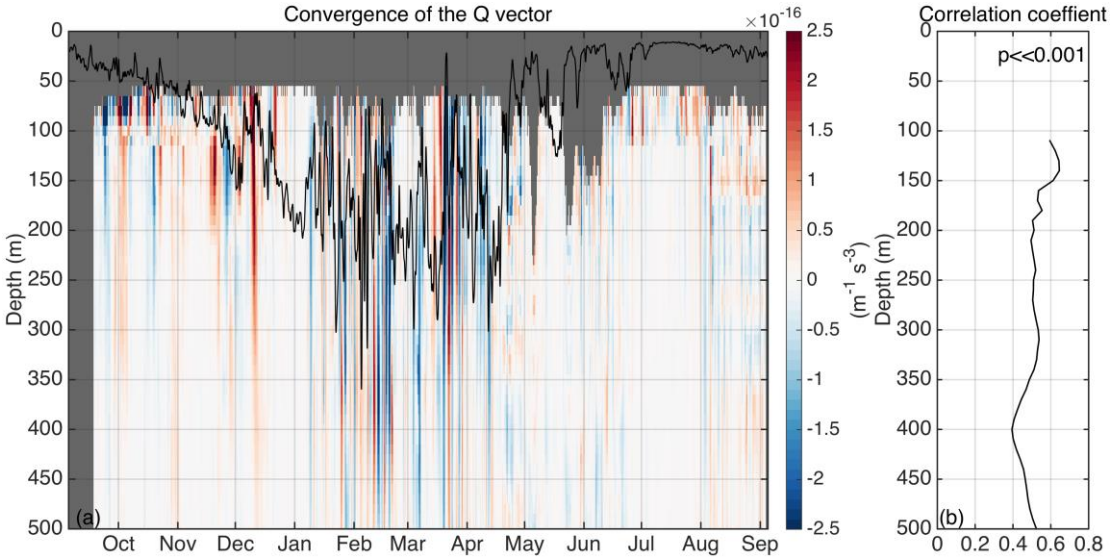


Figure 3.16: (a) Convergence of the Q vector (i.e. $-\nabla_h \cdot \vec{Q}_{CO,30h}$) estimated from the outer cluster, and (b) correlation coefficient with the outer $w_{CO,30h}$ estimated from the density equation.

### 3.7 Conclusions

The year-long OSMOSIS mooring observations provide an unprecedented long-term dataset to assess the phenomenology of submesoscale vertical flow in the context of measurements of mesoscale motions.

My results indicate that submesoscale motions act to restratify the upper ocean throughout the year, and most intensely in winter and spring. Enhanced submesoscale vertical velocity and buoyancy flux generally occur in the presence of energetic mesoscale features. While submesoscale flows are found to be largely in geostrophic balance below the ML, ageostrophic circulations can be induced in response to strong frontal tendency to restore geostrophy. Persistent frontogenesis induced by the mesoscale strain field is common to periods of intensified submesoscale lateral buoyancy gradient and rapid surface restratification. This is consistent with mesoscale frontogenesis playing a role in generating the lateral buoyancy fronts that are necessary for the development of submesoscale turbulence. The role of mesoscale frontogenesis in underpinning the enhanced submesoscale turbulence is suggested by the marked increase in submesoscale vertical velocity and buoyancy flux for periods of intensification of submesoscale lateral buoyancy gradient. The net upper-ocean

restratification induced by submesoscale motions over the annual cycle is comparable in magnitude to the destratification associated with the annual-mean atmospheric cooling of the area, indicating that submesoscales play an important role in determining the climatological state of the local stratification.

# Chapter 4: The annual cycle of upper-ocean potential vorticity and its relationship to submesoscale instabilities

---

This chapter investigates attributing processes for the evolution of the OSBL from the PV budget perspective. A mathematical framework is developed to closing the PV budget from measurements with a horizontal resolution of about 10 km, under certain simplifying assumptions appropriate for the current dataset. The submesoscale instabilities are discussed focusing on the role of SI in upper-ocean turbulent convection and its dependence with atmospheric forcing.

## 4.1 Abstract

Potential vorticity (PV) is a key property in understanding the competing processes that deepen and shoal the ocean surface boundary layer (OSBL). Previous PV studies of these processes were mainly based on numerical simulations. Here I use a year-long, meso- and submesoscale resolving time series of buoyancy and horizontal velocity, obtained from mooring observations in the Northeast Atlantic under the auspices of the UK NERC OSMOSIS programme, to investigate the upper-ocean PV budget and its relationship with the occurrence of submesoscale frontal instabilities. The results show that non-advective PV changes in the OSBL are balanced by the diabatic and frictional PV fluxes in an integral sense. Deep mixed layers (up to about 350 m) during wintertime are attributed to persistent atmospheric cooling. The cooling predominantly triggers gravitational instability (GI) that leads to deepening of the mixed layer. However, on shorter time scales, conditions favorable to symmetric instability (SI) are often observed when winds are aligned with frontal flow. The ensuing overturning instabilities rapidly re-stratify the mixed layer and limit the reduction of PV, as indicated by the approximate balance between the local temporal change of PV and the advection of PV below the convective layer. These results emphasize the key role of submesoscale instabilities in determining the evolution of the OSBL.

## 4.2 Introduction

The evolution of the OSBL is the dynamical foundation of our understanding of the exchange rate of physical properties (such as heat, momentum) and biogeochemical tracers (such as carbon, oxygen, nutrients) between the ocean surface and the ocean interior (Klein and Lapeyre 2009; Lévy et al. 2012; Omand et al. 2015; McWilliams 2016). Traditional thinking of the OSBL evolution and the associated vertical exchange are governed by one-dimensional processes, which enter the climate-scale models of the ocean circulation via parameterizations such as KPP (K profile parameterization; Large et al. 1994). These one-dimensional parameterizations assume a local balance between the net surface buoyancy flux into the ocean through the surface and a vertical redistribution of buoyancy due to vertical mixing (Spall et al. 2000). More recent studies suggest that the OSBL is a turbulent environment responding to processes across different spatial and temporal scales, including Langmuir turbulence (Belcher et al. 2012), internal waves (Alford et al. 2015), convective mixing (Taylor and Ferrari 2010) and three-dimensional frontal instabilities (Sasaki et al. 2014; Thomas et al.

2016). More importantly, these multi-scale processes do not exist in isolation but interact with each other in the upper ocean (e.g. Hamlington et al. 2014; Haney et al. 2015).

In particular, a series of papers by Thomas and co-authors (Thomas and Lee 2005; Thomas and Ferrari 2008; Thomas and Taylor 2010; Thomas et al. 2016) highlight the importance of the interaction between surface winds and submesoscale fronts, especially the role of downfront winds (i.e., oriented in the direction of the geostrophic shear) in reducing the PV in the OSBL and often 'preconditioning' the flow to SI. Downfront winds destabilize the water column as Ekman flow advects dense water over light water for this wind orientation (also see in Figure 1.4). Some observational research shows that forced SI in the upper ocean, either by buoyancy loss or by downfront winds, may provide an effective exchange pathway with the atmosphere, and play a significant role in the energy balance of the ocean circulation in the regions with strong frontal strength and surface forcing like the Gulf Stream (Thomas et al. 2013; Thomas et al. 2016) and the Kuroshio (D'Asaro et al. 2011). Brannigan (2016) have also shown that using an idealized model intense submesoscale upwelling, associated with SI inside anticyclonic eddies, may drive a transport of nutrients from the thermocline to the mixed layer. However, the integrated effect of SI in the more general open ocean situation, where fronts and surface forcing are intermittent in direction and strength is still unclear.

The concept of Ertel PV has been widely used to advance our understanding of dynamical behavior in the atmosphere (Hoskins 1974; McDowell et al. 1982; Haynes and McIntyre 1987) and ocean (Marshall and Nurser 1992; Polton and Marshall 2007; Thomas 2008; Maze et al. 2013). PV strongly constrains the circulation in a stratified, rotating fluid system (Haynes and McIntyre 1987; Hoskins et al. 1985; McIntyre 2015a). For adiabatic and inviscid flow, the PV is materially conserved, but the PV can be created or destroyed at the surface by diabatic and frictional atmospheric fluxes. Hoskins (1974) point out that the Ertel PV taking the opposite sign of the Coriolis parameter is a necessary condition for the generation of SI. Furthermore, Taylor and Ferrari (2010) have proposed that a turbulent layer may be generated by SI below a convective layer in the presence of lateral buoyancy fronts and surface buoyancy loss. Numerical simulations from Thomas et al. (2008) and Brannigan (2016) show that SI acts as a PV pump, upwelling high PV water from the pycnocline and subducting low-PV water in the OSBL. Consequently, I employ a framework of the flux form of the

PV equation to investigate these dynamical processes (i.e., atmospheric fluxes and frontal instabilities) that set the circulation of the OSBL and the ocean interior.

The OSMOSIS mooring dataset provides a unique opportunity to resolve an annual cycle of the OSBL accounting for turbulent processes that deepen and meso- and submesoscale processes shoaling the layer. In this chapter, I will present an observation based investigation of the PV budget of a patch with a horizontal spatial scale of 10 km, focussing on the distinguishing characteristics of the OSBL dynamics. The closure of the OSBL PV budget will be described, in which diabatic and frictional effects and three-dimensional frontal instabilities play significant roles.

The layout of this chapter is as follows. The data and methods are introduced in Section 4.3. Section 4.4 contains a description of the PV budget in the upper ocean and a summary of the annual cycle of submesoscale characteristics. A discussion and the conclusions are given in Sections 4.5 and 4.6, respectively.

## 4.3 Data and Methods

The framework of the flux form of the PV equation is established by the measurements of horizontal velocity and buoyancy from the central and four outer moorings (Figure 4.1). It should be noted that measurements from the inner moorings are not used for closing the PV budget, because the horizontal gradients of PV between two inner moorings are found to be over noisy in such a small distance.

As a brief summary of the data processing for the PV budget analysis, temperature, salinity and horizontal velocity measured at outer- and central-mooring instruments were interpolated onto a uniform depth grid (10 m intervals between depths of 50 m and 520 m) and averaged onto hourly intervals. A fourth-order low-pass Butterworth filter with a cutoff frequency of 0.8 cpd (period of 30 hours) was then applied to the hourly data, and then the data time series were averaged onto daily intervals. The heat flux, freshwater flux and wind stress were also averaged onto the daily intervals to match the mooring data.

### 4.3.1 Upper-ocean potential vorticity

The Ertel PV is defined as:

$$q_{Ertel} = \omega_a \cdot \nabla b, \tag{4.1}$$

where $\omega_a = 2\Omega + \nabla \times \boldsymbol{u}$ is the absolute vorticity, $\Omega$ is Earth's angular velocity, $b$ is the buoyancy as already defined in Chapter 3 and $\boldsymbol{u} = (u, v, w)$ is the three-dimensional velocity vector. Following, e.g. Thomas et al. (2013), the PV can be

decomposed into two terms

$$q = q_{vert} + q_{bc}, \tag{4.2}$$

where the subscripts '*vert*' and '*bc*' denote the vertical and baroclinic components of PV, respectively. Dividing the PV into these two components highlights the contrasting roles of vertical vorticity/stratification and baroclinicity under certain assumptions, which will be discussed as follows.

The first term on the RHS of Equation 4.2,

$$q_{vert} = (f + \zeta)N^2, \tag{4.3}$$

is associated with the vertical component of the absolute vorticity, $f + \zeta$, and the vertical stratification $N^2$, where $f = 2\Omega\sin\phi$ is the Coriolis parameter, $\phi$ is latitude and $\zeta = \partial v/\partial x - \partial u/\partial y$ is the vertical relative vorticity.

The second term on the RHS of Equation 4.2, expressed as

$$q_{bc} = \omega_h \cdot \nabla_h b = \left(\frac{\partial w}{\partial y} - \frac{\partial v}{\partial z}\right)\frac{\partial b}{\partial x} + \left(\frac{\partial u}{\partial z} - \frac{\partial w}{\partial x}\right)\frac{\partial b}{\partial y}, \tag{4.4}$$

is attributable to the horizontal components of vorticity $\omega_h$and horizontal buoyancy gradient $\nabla_h b$. Note that terms related to the non-traditional component (i.e. the locally horizontal component of the Earth's rotation) of the Coriolis frequency are neglected (i.e., in strongly stratified flows we have $N^2 \gg 4|\Omega|^2$, making $\nabla b$ nearly vertical – the scalar multiplication by $\nabla b$ picks out $f$, which is the latitude-dependent vertical component of $2\Omega$, to good approximation). By further neglecting terms that include vertical velocity in Equation 4.4 and assuming geostrophic balance, the expression for the PV may be written as

$$q = (f + \zeta)N^2 - \frac{1}{f}|\nabla_h b|^2. \tag{4.5}$$

In this expression, the baroclinic component, $q_{bc} = -\frac{1}{f}|\nabla_h b|^2$, is always negative and reduces the PV, whereas $q_{vert}$ may be either positive or negative. Importantly, SI tends to develop when $q_{bc}$ can overcome $q_{vert}$ with $q_{vert} > 0$.

Although this expression of PV (Equation 4.5) is widely used in observational studies (e.g., Thomas et al. 2013; Thompson et al. 2016), there may be two possible sources of error associated with the approximations here. First, I neglect terms in $q_{bc}$ that involve the vertical velocity $w$. Preliminary estimates of the vertical velocity at each mooring site confirm that this is a reasonable assumption. Second, I assume the flow is in geostrophic balance. This is supported by the close agreement between the along-mooring lateral buoyancy gradient and measured vertical shear at the central

mooring (see Figure 3.3 in Chapter 3).

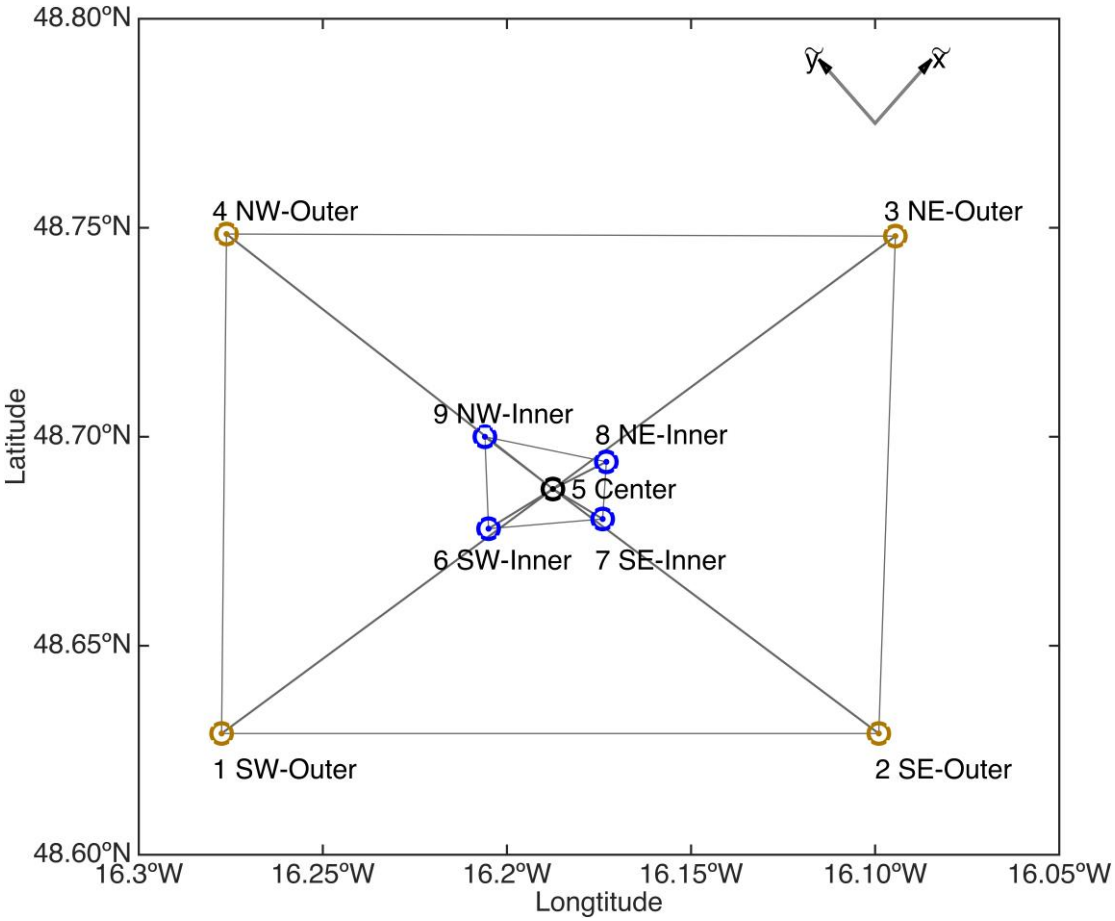


Figure 4.1: Locations of center (black), four inner moorings (blue) and four outer moorings (dark yellow). Numbers (1-9) are also used to denote the different locations of moorings. The inner mooring domain is divided into four triangular regions. The rotated coordinate system is plotted as reference.

### 4.3.2 PV flux framework from the outer mooring array

It may be inferred from PV conservation that the local temporal changes of PV at the central mooring arise from the convergence or divergence of the $J$ vectors within the outer-mooring boundary (Marshall and Nurser 1992),

$$\partial q/\partial t \; + \; \nabla \cdot J = 0, \tag{4.6}$$

where $J$ represents the total advective and non-advective transport of PV in the ocean,

$$J = \; q\boldsymbol{u} \; + \nabla b \; \times \; \boldsymbol{F} - \omega_a \, Db/Dt. \tag{4.7}$$

The $J$ vector has advective ($q\boldsymbol{u}$), frictional ($J^F = \nabla b \times \boldsymbol{F}$) and diabatic ($J^D = -\omega_a \, Db/Dt = \; -\omega_a \mathcal{D}$) components. Here $\boldsymbol{F}$ is a frictional or non-conservative body force; $Db/Dt$ is the Lagrangian rate of change of buoyancy, and $\mathcal{D}$ represents all diabatic processes. Further, I am unable to comment on the top 50 m water column

owing to the minimum observable depth of moorings. To solidify this empirical parameter choice, the value should be revisited in future studies and can certainly by increased as more data, especially at small separation distances, become available. When these assumptions are violated (and in practice they are never perfectly valid), the interpretation of either statistic, and of their mutual relation, becomes much more difficult. Hence, caution in analysing either statistic is recommended, and it is crucial to assess and possibly mitigate departures from homogeneity and isotropy.

According to the 'impermeability theorem' (Haynes and McIntyre 1987), the PV in any isopycnal layer can only be changed by PV fluxes through a boundary. The PV flux across the sea surface (hereafter denoted by $J_z$) is thus the only 'forcing term' in the PV budget of the OSBL in an integral sense, and defined as

$$J_z = J_z^F + J_z^D = (\nabla b \times \boldsymbol{F})_{z=0} - (\omega_a \, Db/Dt)_{z=0}. \tag{4.8}$$

With the knowledge of Equations 4.7-4.8, taking the depth integral of Equation 4.6 yields

$$\int \frac{\partial q}{\partial t} dz + \int \boldsymbol{u} \cdot \nabla q \, dz + J_z^D + J_z^F = 0. \tag{4.9}$$

The PV conservation equation applied here indicates that the temporal change of PV and advective PV flux integrated over the OSBL are balanced by the diabatic and frictional PV fluxes through the sea surface. Below the OSBL, PV is approximately a materially conserved scalar and the diabatic and frictional terms can be neglected in Equation 4.9. The measurements from the central and four outer moorings are used to estimate the terms in Equations 4.9 under certain assumptions, as described in the following subsections.

#### 4.3.2.1 Temporal change of PV

To estimate the temporal change of PV $(\partial q/\partial t)$ at the central mooring site, the measurements at the four outer moorings are used for the calculation of $\zeta$ and $|\nabla_h b|$. To do so, the coordinate is rotated counter-clockwise (CCW) by an angle of 45 degrees (Figure 4.1). The $\zeta$ and $|\nabla_h b|$ at the central mooring site are given by:

$$\zeta_5 = \frac{\tilde{v}_3 - \tilde{v}_1}{\tilde{x}_3 - \tilde{x}_1} - \frac{\tilde{u}_4 - \tilde{u}_2}{\tilde{y}_4 - \tilde{y}_2}, \tag{4.10}$$

$$|\nabla_h b|_5 = \sqrt{\left(\frac{\tilde{b}_3 - \tilde{b}_1}{\tilde{x}_3 - \tilde{x}_1}\right)^2 - \left(\frac{\tilde{b}_4 - \tilde{b}_2}{\tilde{y}_4 - \tilde{y}_2}\right)^2}, \tag{4.11}$$

where $\tilde{u} = u\,cos\,45º - v\,sin\,45º$ and $\tilde{v} = u\sin 45º + v\cos 45º$ denote horizontal velocities in the rotated coordinate, and subscripts indicate mooring numbers (Figure 4.1). The PV at the central mooring is then given by

$$q_5 = (f + \zeta_5)N_5^2 - \frac{1}{f}(|\nabla_h b|_5)^2. \tag{4.12}$$

Here the time differential in the calculation of $\partial q_5/\partial t$ is 24 hours.

#### 4.3.2.2 Horizontal advection of PV

PV fields at four outer-mooring sites are needed to estimate the horizontal advection of PV, $u\frac{\partial q}{\partial x} + v\frac{\partial q}{\partial y}$. Note that the horizontal gradients in velocity and buoyancy cannot be estimated directly at their locations, so they are calculated assuming the same lateral gradients of velocity and buoyancy between two neighbouring moorings. For example, $\zeta$ and $|\nabla_h b|$ at the SW-Outer mooring (Figure 4.1) can be computed as

$$\zeta_1 = \frac{v_2 - v_1}{x_2 - x_1} - \frac{u_3 - u_1}{y_3 - y_1}, \tag{4.13}$$

$$|\nabla_h b|_1 = \sqrt{(\frac{b_2 - b_1}{x_2 - x_1})^2 - (\frac{b_3 - b_1}{y_3 - y_1})^2}. \tag{4.14}$$

One can similarly compute the $\zeta$ and $|\nabla_h b|$ at the NE-Outer mooring:

$$\zeta_3 = \frac{v_4 - v_3}{x_4 - x_3} - \frac{u_3 - u_1}{y_3 - y_1}, \tag{4.15}$$

$$|\nabla_h b|_3 = \sqrt{(\frac{b_4 - b_3}{x_4 - x_3})^2 - (\frac{b_3 - b_1}{y_3 - y_1})^2}. \tag{4.16}$$

The horizontal advection of PV is derived from the PV fields at four outer-mooring sites and horizontal velocity measurements at the central mooring. The coordinate is rotated CCW by an angle of 45 degrees to compute the horizontal advection of PV:

$$u\frac{\partial q}{\partial x} + v\frac{\partial q}{\partial y} = \tilde{u}_5\frac{q_3 - q_1}{\tilde{x}_3 - \tilde{x}_1} + \tilde{v}_5\frac{q_4 - q_2}{\tilde{y}_4 - \tilde{y}_2}. \tag{4.17}$$

#### 4.3.2.3 Vertical advection of PV

The vertical advection of PV, $w\frac{\partial q}{\partial z}$, is computed separately in the OSBL and the ocean interior. In the OSBL, the set of equations from which my results are derived is given below. These encompass the alternative expression of the vertical advection of PV, buoyancy equation, continuity equation, and the two components of PV:

$$w\frac{\partial q}{\partial z} = \frac{\partial(wq)}{\partial z} - q\frac{\partial w}{\partial z}, \tag{4.18}$$

$$\frac{\partial b}{\partial t} + u_h\nabla_h b + wN^2 = \mathcal{D}, \tag{4.19}$$

$$\frac{\partial u}{\partial x} + \frac{\partial v}{\partial y} + \frac{\partial w}{\partial z} = 0, \tag{4.20}$$

$$q = q_{vert} + q_{bc}. \quad (4.21)$$

I simplify this set of equations further by assuming low diffusion ($\mathcal{D}$ is negligible) and a small baroclinicity term ($q_{bc} \ll q_{vert}$). Applying these assumptions, I obtain

$$w\frac{\partial q}{\partial z} = \frac{\partial}{\partial z}(wq_{vert}) - q\frac{\partial w}{\partial z}. \quad (4.22)$$

I use the buoyancy equation to yield $wN^2$ in the $wq_{vert}$ term (see Equation 4.3), and the continuity equation to yield $\frac{\partial w}{\partial z}$ for the OSBL,

$$w\frac{\partial q}{\partial z}|_{OSBL} = \frac{\partial}{\partial z}\left[\left(-\frac{\partial b}{\partial t} - u\frac{\partial b}{\partial x} - v\frac{\partial b}{\partial y}\right)(f + \zeta)\right] + q\left(\frac{\partial u}{\partial x} + \frac{\partial v}{\partial y}\right). \quad (4.23)$$

In the ocean interior, $w\frac{\partial q}{\partial z}$ can be calculated directly from the estimated vertical velocity (Chapter 3) and PV (Equation 4.12) at the central mooring site,

$$w\frac{\partial q}{\partial z}|_{interior} = \left[\frac{\left(-\frac{\partial \rho}{\partial t} - u\frac{\partial \rho}{\partial x} - v\frac{\partial \rho}{\partial y}\right)}{\frac{\partial \rho}{\partial z}}\right][(f + \zeta_5)N_5^2 - \frac{1}{f}(|\nabla_h b|_5)^2]. \quad (4.24)$$

#### 4.3.2.4 Diabatic PV flux

Following Marshall and Nurser (1992), the diabatic PV flux (i.e., diabatic component of the $J$ vector) at the sea surface is approximated by

$$J_z^D = -\frac{fg\alpha Q_{\text{net}}}{H\rho_0 c_p} + \frac{f\beta S(E-P)}{H} = B_0\frac{f}{H}, \quad (4.25)$$

where $B_0 = -\frac{g\alpha}{\rho_0 c_p}Q_{\text{net}} + g\beta S(E-P)$ is the surface buoyancy flux (SBF), $Q_{\text{net}}$ is the air-sea heat flux, $c_p$ is the specific heat capacity, $\alpha$ and $\beta$ are the thermal and haline expansion coefficients, $S$ is the surface salinity, $(E-P)$ is the freshwater flux, $H$ is the MLD. Note that $J_z^D$ is positive for a surface buoyancy loss, and is negative for a surface buoyancy gain.

#### 4.3.2.5 Frictional PV flux

Following Thomas (2005), the frictional PV flux (i.e., frictional component of the $J$ vector) at the sea surface is approximated by

$$J_z^F = \frac{\vec{k}\cdot(\tau \times \nabla b)}{\rho_0 \delta_e} = B_e\frac{f}{\delta_e}, \quad (4.26)$$

where $B_e = \vec{k}\cdot(\tau \times \nabla b)/\rho_0 f$ is the Ekman buoyancy flux (EBF), $\tau$ is the surface wind stress, and $\delta_e$ is the Ekman layer depth. The Ekman layer depth is usually approximated by $\delta_e = 0.4u_*/f$, with $u_* = \sqrt{|\tau|/\rho}$, where 0.4 is an empirical constant determined from observations (Wang and Huang 2004). Note that $J_z^F$ is positive if the wind stress has a component downfront (i.e., directed with the geostrophic shear), and

negative if the wind stress has a component upfront (i.e., directed against the geostrophic shear).

### 4.3.3 Identification of instability types in the mixed layer

#### 4.3.3.1 Horizontal gradients and subsequent quantities in a triangle mooring array

The mooring dataset available allows an estimate of $\zeta$ and $|\nabla_h b|$ at different horizontal resolutions in the area delimited by the mooring cluster. Here, in order to maintain as high a spatial resolution as possible, I divide the inner mooring domain into four triangular regions (Figure 4.1). The hourly data series are low-pass filtered with a fourth-order low-pass Butterworth filter of 6-h cutoff (i.e. advective time scale of the inner mooring array). In each triangular mooring array, gradients in velocity and buoyancy can be obtained averaged over the whole triangle instead of at a single point. To do so, the coordinates are rotated CCW by an angle of 45 degrees (Figure 4.1). For example, one can compute $\zeta$ and $|\nabla_h b|$ for the west triangle:

$$\zeta_{569} = \frac{\tilde{v}_5 - \tilde{v}_6}{x_5 - x_6} - \frac{\tilde{u}_9 - \tilde{u}_5}{y_9 - y_5}, \tag{4.27}$$

$$|\nabla_h b|_{569} = \sqrt{\left(\frac{b_5 - b_6}{x_5 - x_6}\right)^2 - \left(\frac{b_9 - b_5}{y_9 - y_5}\right)^2}. \tag{4.28}$$

It is also worth noting that $\zeta$ can be estimated alternatively from circulation following Stokes' theorem $\zeta = \lim_{A \to 0} \oint \vec{u} \cdot d\vec{l}$ (Batchelor 2000), yielding numerically equivalent values.

#### 4.3.3.2 Identification of instability types in the OSBL

Various overturning instabilities may arise when planetary vorticity takes the opposite sign to PV (Hoskins 1974; Haine and Marshall 1998), which at the PAP site is equivalent to negative PV. Negative PV values may occur when the fluid column is unstably stratified (GI) or experiences horizontally sheared flows (CI) or strong anticyclonic along-isopycnal shear (SI).

In order to distinguish the attributable processes for the onset of overturning instabilities, the balanced Richardson number angle $\phi_{Ri_B} = \tan^{-1}\left(-\frac{f^2 N^2}{|\nabla_h b|^2}\right)$ and the critical angle $\phi_C = \tan^{-1}\left(-\frac{\zeta_g}{f}\right)$ were introduced by Thomas et al. (2013), with $\zeta_g = f + \nabla \times \boldsymbol{u}_g \cdot \vec{k}$ as the vertical component of the absolute vorticity of the geostrophic flow (Haine and Marshall 1998). The instability criterion may be expressed as $\phi_{Ri_B} <$

$\phi_C$ and the types of instabilities may be identified by the value of $\phi_{Ri_B}$. (i) GI is expected to dominate when -180° < $\phi_{Ri_B}$ < -135° and $N^2$ < 0. A hybrid GI/SI will occur when -180° < $\phi_{Ri_B}$ < -135° and $N^2$ < 0. (ii) For stable stratification ($N^2$ > 0) and cyclonic vertical vorticity, SI should arise when -90° < $\phi_{Ri_B} < \phi_C$, with $\phi_C$ < -45°. (iii) For anti-cyclonic vertical vorticity, SI is indicated by -90° < $\phi_{Ri_B}$ < -45° with $\phi_C$ > -45°, and a hybrid symmetric-centrifugal instability is expected when -45° < $\phi_{Ri_B} < \phi_C$.

I note that assumptions here include that there is no curvature to the flow and that there is thermal wind balance. Also, this analysis does not take into account the mixed-layer BCI which can arise when $fq$ is positive, and the stratification is modified by surface waves (Hamlington et al. 2014; Haney et al. 2015).

### 4.3.4 Convective layer depth

Taylor and Ferrari (2010) proposed a two-layer system in the OSBL in conditions of a front subject to buoyancy loss: (1) a surface convective layer, $h$, and a 'forced SI' layer beneath the convective layer (here I refer to this layer as the intermediate layer). Near the surface in the convective layer ($z > -h$) convective mixing develops and the water column stays relatively unstable. In the intermediate layer, restratification by forced SI (due to buoyancy loss or downfront winds) wins the competition with the convective mixing, and the boundary layer restratifies.

Following Thomas et al. (2013) and Bachman et al. (2017), a quartic equation is used to solve for the convective layer depth (CLD) $h$,

$$\left(\frac{h}{H}\right)^4 - c^3 \left(1 - \frac{h}{H}\right)^3 \left[\frac{w_*^3}{|\Delta u_g|^3} + \frac{u_*^2}{|\Delta u_g|^2} \cos\theta_w\right]^2 = 0, \qquad (4.29)$$

where $w_* = (B_0 H)^{1/3}$ is the convective velocity; $u_* = \sqrt{|\tau|/\rho_0}$ is the frictional velocity; $\theta_w$ is the angle between the wind vector and the geostrophic shear and $c$ = 14 is an empirical constant. The change in geostrophic velocity across the OSBL, $\Delta u_g$, is computed by assuming geostrophic balance as $\Delta u_g = \left|\partial \boldsymbol{u_g}/\partial z\right| H = |\nabla_h b| H/f$. Making the substitution,

$$\gamma = c^3 \left[\frac{w_*^3}{|\Delta u_g|^3} + \frac{u_*^2}{|\Delta u_g|^2} \cos\theta_w\right]^2, \qquad (4.30)$$

Equation 4.29 becomes

$$\left(\frac{h}{H}\right)^4 + \gamma \left(\frac{h}{H}\right)^3 - 3\gamma \left(\frac{h}{H}\right)^2 + 3\gamma \left(\frac{h}{H}\right) - \gamma = 0. \qquad (4.31)$$

This equation has two complex solutions and two real solutions for $h/H$, and only

solution between 0 and 1 that is of interest (Bachman et al. 2017). The CLD $h$ is therefore always no greater than the OSBL depth $H$. When $h/H \ll 1$ much of the OSBL is dominated by SI restratification (i.e., slantwise convection), whereas for $h/H \sim 1$ the layer is dominated by vertical convective mixing. The relationship during wintertime between $\gamma$ and the real solution of interest is shown in Figure 4.2 and here $\gamma$ is in the range of $10^{-3}$ to $10^{7}$.

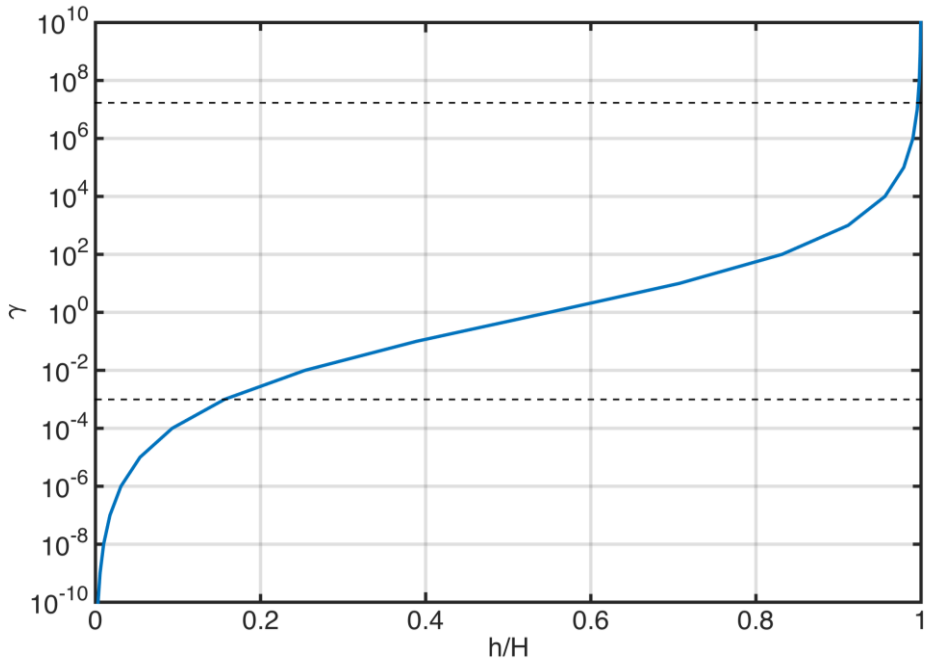


Figure 4.2: Numerical solution of the quartic Equation 4.31 for the ratio of the CLD to MLD, $h/H$. The solution is plotted as a function of γ, which ranges here from $10^{-10}$ to $10^{10}$. Adapted from Bachman et al. (2017). Dashed lines indicate the boundaries of wintertime γ estimated from the OSMOSIS mooring dataset.

## 4.4 Results

### 4.4.1 An annual cycle of upper-ocean PV

Using Equation 4.5, it is possible to generate a year-long times series of upper-ocean PV (Figure 4.3). The general features of the PV time series typically coincide with the seasonal variability of the MLD. Negative PV is frequently observed within the deep mixed layer during winter and early spring (December – late April), suggestive of conditions that are unstable to overturning instabilities. Below the mixed layer, PV is largely positive with an enhancement at the base of the mixed layer, where the maximum value of PV reaches $10^{-8}$ $s^{-3}$, exceeding ocean-interior typical values by one order of magnitude, in particular during non-winter time.

Note that the annual cycle of PV looks very similar to the $N^2$ time series (Figure 3.1b), with well-mixed conditions in winter and early spring, surface warming in late spring and summer and erosion of stratification in fall. This is because the derived horizontal gradients in velocity and buoyancy are small from the outer mooring array. Working with the same mooring data Buckingham et al. (2016) indicate that relative vorticity is positively skewed during winter, even though the scale of the Rossby number is less than 0.5. These relatively small vertical vorticity values reflect the fact that the study region is not generally favorable for CI, consistent with our later results (e.g. Figure 4.10). Furthermore, it will be shown later in this chapter that the lateral buoyancy gradient term becomes more important when, in the inner-triangle mooring array, the submesoscale fronts are better resolved.

In addition to the seasonality, the year-long PV time series reveal dramatic transitions from fall to winter and from spring to summer. A strong convective event, caused by destabilizing surface forcing at the fall-winter transition (around 25 November - 5 December), reduced PV to negative values and deepened MLD by 100 m within a period of a few days. The persistent stratification of the OSBL occurred after the spring-summer transition, caused by a cyclonic intrathermocline eddy (3 May) and a persistent surface heating period (mid-May). After that, MLD remained shallow at about 20 m. Moreover, low PV values were also found around 6 August associated with the appearance of an anti-cyclonic eddy that propagated across the mooring array.

The MLD is considerably more variable throughout the winter, attributed to the competing processes of multiple instances of rapid surface restratification by frontal overturning instabilities and deepening processes by destabilizing surface forcing. The cumulative MLD change over time provides further information on the intensity of the competing processes in the OSBL (Figure 4.4). Most of the mixed layer deepening and shoaling events occur from December 2012 to late April 2013, when the mixed layer is deep and submesoscale motions are expected to be active. I will focus on this period in our PV budget analysis in the OSBL. For the rest of year, the variability of the mixed layer is relatively small with the MLD largely shallower than 50 m. I am unable to comment on summertime PV dynamics in the OSBL.

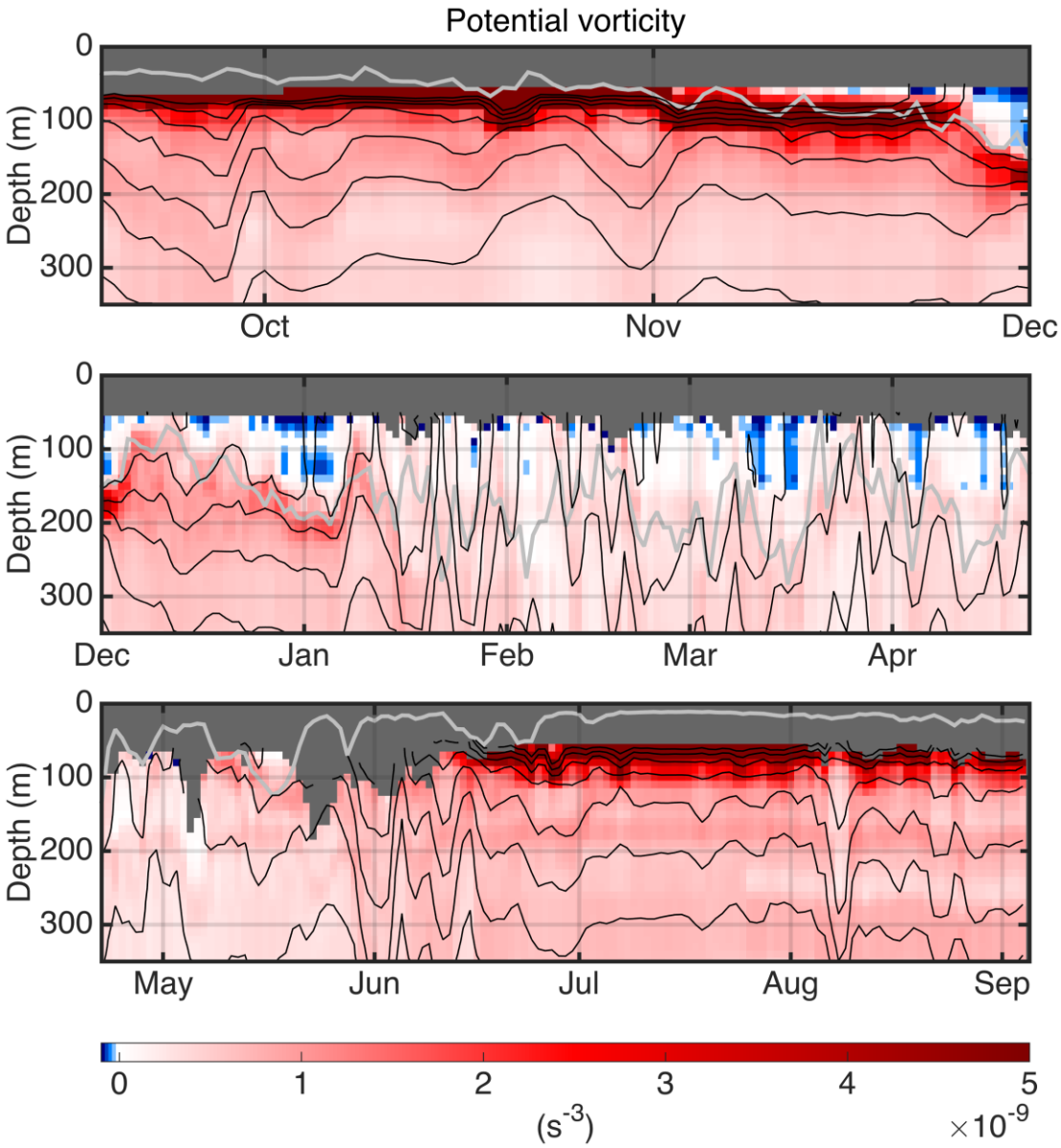


Figure 4.3: Year-long time series of PV, calculated from the daily central and outer mooring data as described in Section 4.3.1. The time series is divided into (top) fall, (middle) winter and (bottom) spring-summer periods. The MLD is superimposed as a light grey line. Missing values in our calculations are colored in dark grey. Isopycnals are overlaid as solid black lines.

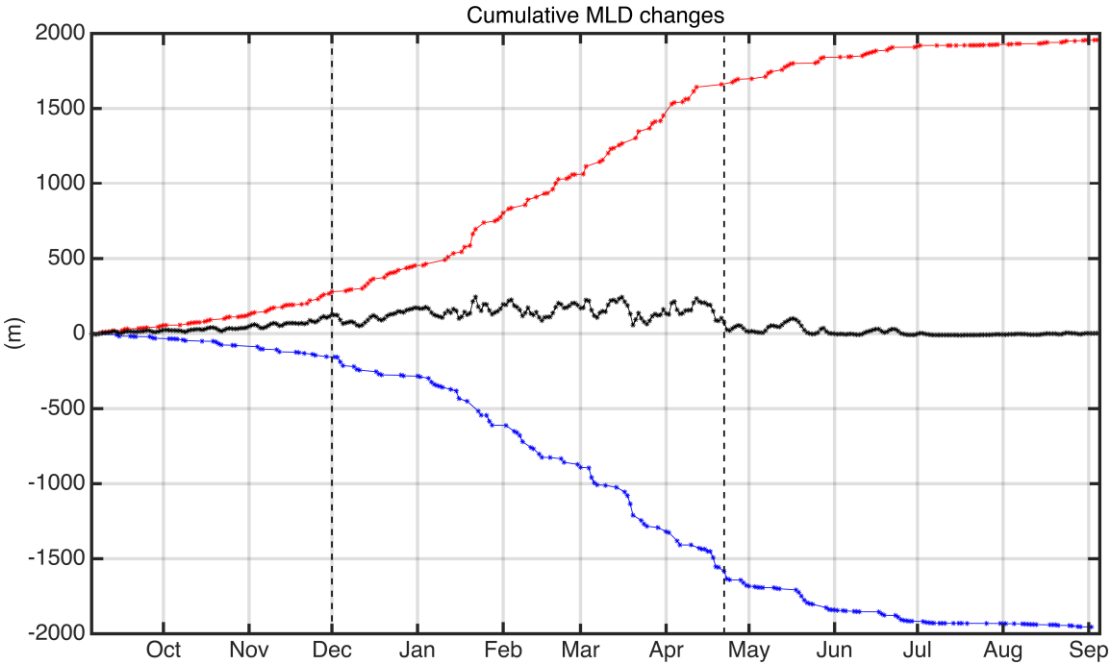


Figure 4.4: The time integral of daily $dH/dt$ (black), positive $dH/dt$ (MLD deepening; red), and negative $dH/dt$ (MLD shoaling; blue) showing the cumulative MLD changes.

### 4.4.2 An annual cycle of diabatic and frictional PV fluxes

The year-long time series of diabatic ($J_z^D$) and frictional ($J_z^F$) PV fluxes are shown in Figure 4.5. Note that PV is extracted from the ocean when $J_z^D + J_z^F > 0$. Consistent with the seasonal cycle of the upper-ocean PV, the $J_z^D$ at the sea surface changes from a sizeable PV exit ($J_z^D > 0$) in winter to a very strong PV entry ($J_z^D < 0$) in summer, with maximum amplitudes of $1 \times 10^{-12}$ m s$^{-4}$ and $-3 \times 10^{-12}$ m s$^{-4}$, respectively. This asymmetry is caused by the shallow MLD (~20 m) between June and September in 2013. The non-wintertime $J_z^D$ is larger in magnitude than the wintertime $J_z^D$, because the summer heating confines the diffusive flux to a much shallower depth than the winter MLD, which enhances the magnitude of the vertical divergence of the non-advective buoyancy flux over the mixed layer. The strong seasonality of $J_z^D$ is mainly determined by the local air-sea heat flux, which is directed from the ocean to the atmosphere in fall/winter and directed from the atmosphere to the ocean in spring/summer. In contrast, the $J_z^D$ contributed from the freshwater flux is more intermittent, and very small compared with the surface air-sea heat flux at the PAP site.

Including the cross product of the surface wind stress and the near-surface lateral buoyancy gradient, reversals in sign are frequent in the frictional PV flux $J_z^F$ throughout the entire year. A comparison of the $J_z^F$ estimated from the inner and outer buoyancy

gradient is also given in Figure 4.5. A consistent pattern between inner and outer results is observed, and higher magnitudes are observed from the inner moorings owing to the inner cluster's ability to measure the lateral buoyancy gradients at a higher spatial resolution. It is especially true during winter and early spring when elevated mesoscale frontogenesis is commonly observed and submesoscale flows are active. The values of $J_z^F$ are in the range of -6 × $10^{-13}$ to 6 × $10^{-13}$ m $s^{-4}$, which is substantially smaller than $J_z^D$ except in winter and early spring, when the magnitude is comparable between them. It suggests that the surface wind stress combined with the ubiquitous presence of the lateral buoyancy gradients in the OSBL may have an important impact on the evolution of the OSBL at the mooring site, at least during winter and early spring.

The annual mean of non-advective PV fluxes ($\overline{J_z^D + J_z^F}$) in the OSMOSIS region is overwhelmingly dominated by the diabatic processes. The annual averaged $J_z^D$ is found to be directed into the ocean with a value of -2.46 × $10^{-13}$ m $s^{-4}$, indicating that PV entry more than compensates the PV exit from diabatic processes over the annual cycle. In contrast, $J_z^F$ averages towards zero over a long time, with the annual mean value of -1.37× $10^{-15}$ m $s^{-4}$ and -1.52× $10^{-15}$ m $s^{-4}$ for inner and outer moorings, respectively, both two orders of magnitude smaller than that of $J_z^D$. This is consistent with previous studies (e.g., Maze and Marshall 2011; Olsina et al. 2013).

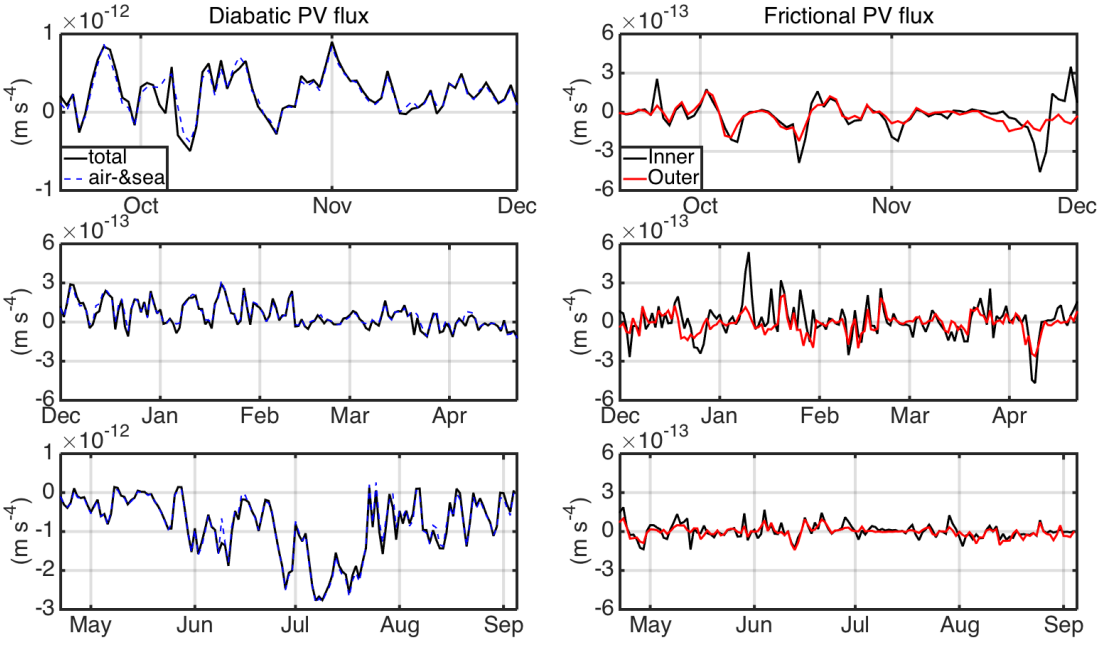


Figure 4.5: Year-long time series of (left) the diabatic PV flux, $J_z^D$, and (right) the frictional PV flux, $J_z^F$, calculated from outer (red) and inner (black) mooring array. The

blue dashed line in the left panel shows contributions from the air&sea heat flux for reference. The time series is divided into (top) fall, (middle) winter and early spring, and (bottom) late spring and summer periods.

### 4.4.3 PV budget in the OSBL

I now focus on attributing processes for the evolution of the OSBL from the PV budget perspective. From 1 December 2012 to 22 April 2013, the vertically integrated temporal changes of PV and advective PV fluxes in the OSBL tend to cancel each other with a statistically significant anti-correlation ($R$ = -0.64, $p$ < 0.001; Figure 4.6a), suggesting that advective PV fluxes in the OSBL play an important role in the local PV changes over short periods. However, as a consequence of the presence of non-advective processes (i.e. diabatic and frictional PV fluxes), the correlation coefficient is smaller than that in the ocean interior ($R$ = -0.81, $p$ < 0.001; Figure 4.9).

To determine the impact of the non-advective PV fluxes on the PV evolution in the OSBL, the values of $J_z^D + J_z^F$ are colored in Figure 4.6a. A higher correlation (i.e., points close to the regression line) is present when the values of $J_z^D + J_z^F$ are small. In contrast, the color scatters also highlight that a relatively lower correlation (i.e., points far from the regression line) is associated with the large magnitude of $J_z^D + J_z^F$. It indicates atmospheric forcing is a strong control on the PV evolution in the OSBL, consistent with previous observational studies (D'Asaro et al. 2011; Thomas et al. 2013). Additionally, a similar pattern and comparable magnitude are shown between the non-advective PV changes ($\partial q/\partial t + \boldsymbol{u} \cdot \nabla q$) and the non-advective PV fluxes ($J_z^D + J_z^F$) (Figures 4.6b-c). Both terms are highly variable in time, and dominated by processes with time scales of a few days. The negative PV is often observed when the PV destruction is produced by the buoyancy loss and/or downfront wind (Figure 4.3). However, a tight link between negative PV and destabilizing forcing at the central mooring is not expected, because locally-generated low PV waters might be advected horizontally or vertically.

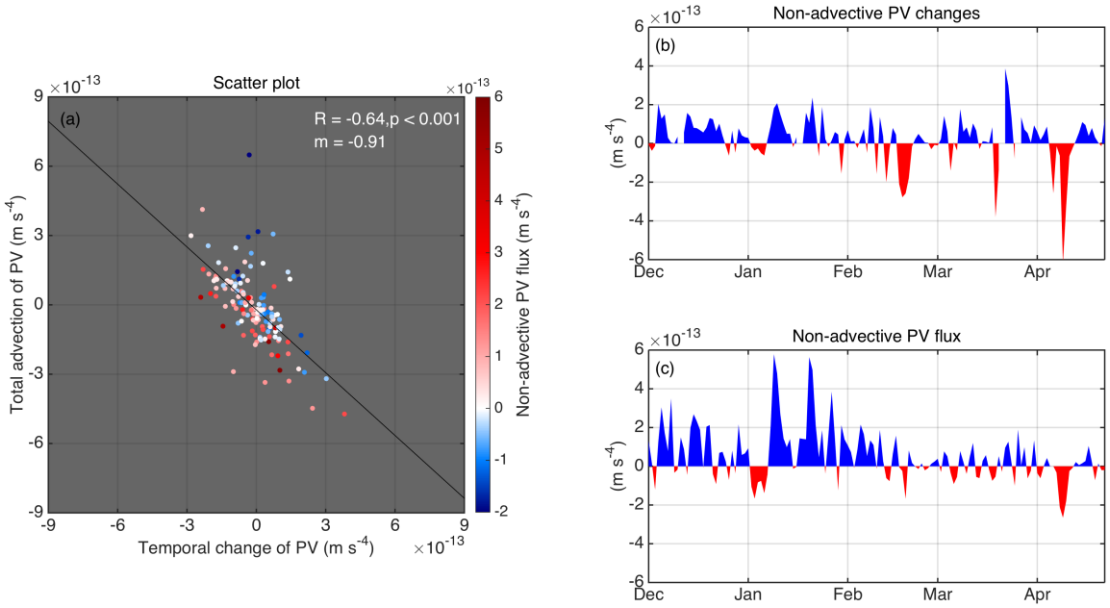


Figure 4.6: (a) Scatter plot of vertically integrated (all measurements in the OSBL) $\partial q/\partial t$ versus $\boldsymbol{u} \cdot \nabla q$ colored by the $J_z^D + J_z^F$, with the best-fit regression line in black. Wintertime series of (b) non-advective PV changes, $\partial q/\partial t + \boldsymbol{u} \cdot \nabla q$, (c) non-advective PV fluxes, $J_z^D + J_z^F$.

To have a closer look at the respective contribution in the PV budget, the time integrals of each term are calculated (Figure 4.7). The diabatic PV flux is still the largest contribution with a strong positive value; that is, it acts to weaken the stratification and hence PV. This is different from the annual mean of diabatic PV flux which indicates a buoyancy gain. The frictional PV flux also has a contribution to reducing PV, but it is not the one to play an important role anymore, because the upfront and downfront winds tend to average out on the long temporal scale over months. Finally, the material change in $q$ (i.e., the temporal change of PV $\partial q/\partial t$, the horizontal advection term $u_h \cdot \nabla_h q$ and vertical advection term $w\frac{\partial q}{\partial z}$) seems to oppose the effect of the diabatic and frictional processes; the horizontal advection is larger than the vertical advection in this case. These results are consistent with a recent numerical study in the North Atlantic, the eddy-resolving model of Maze et al. (2013), which found the amplitude of the frictional PV fluxes to be much smaller than that of the diabatic PV fluxes in a time-mean sense. Furthermore, Czaja and Hausmann (2009) carried out a global estimate of the PV flux with monthly climatologies on a 2° × 2° grid and found that the frictional and diabatic effects act in concert in the North Atlantic to drive the net PV exit.

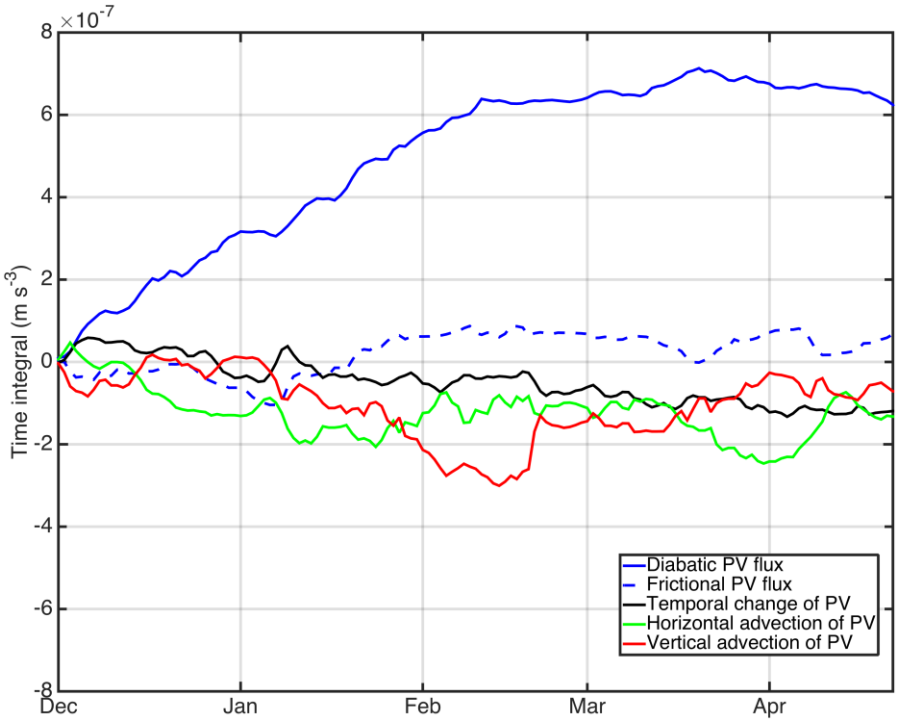


Figure 4.7: The cumulative time integral of diabatic PV flux ($J_z^D$, solid blue), frictional PV flux ($J_z^F$, dashed blue), temporal change of PV ($\partial q/\partial t$, solid black), horizontal advection of PV ($u_h \cdot \nabla_h q$, solid green) and vertical advection of PV ($w\frac{\partial q}{\partial z}$, solid red) from December 2012 to the end of April 2013 showing the cumulative contribution to the PV evolution in the OSBL.

The available CTD/ACM datasets allow for the mathematical framework in Section 4.3.2, which yields a solvable expression for $q$ at all mooring points and material change of $q$ at the central mooring site. When these assumptions are violated (and in practice they are never perfectly valid), the interpretation of either statistic (e.g. correlation coefficient in Sections 4.4.3 and 4.4.4), and of their mutual relation, becomes much more difficult. I acknowledge that the PV evolution contributions from submesoscale motions (~0.1-10 km) and the top 50 m water column not resolved by this framework and the mooring design could be significant and could lead to a better closure of the PV budget. However, the resulting time series (e. g., $Dq/Dt$ and $J_z^D + J_z^F$) are smooth enough to allow for physical interpretation (i.e., to distinguish two different dynamical regimes in the ML as will seen in Figure 4.8). To solidify this formula choice, the datasets should be revisited in future studies and can certainly be tested by submesoscale-resolving model outputs.

I next test the hypothesis that the OSBL is controlled by different dynamics in the

convective layer and the intermediate layer. Again, as already outlined, the OSBL can be subdivided into two layers based on the calculated CLD: the top convective layer $z > -h$, and the intermediate layer $-H < z < -h$. The latter is a region between the convective and the surface boundary layers. The PV budget analyses in these two layers are shown in Figure 4.8. In the convective layer, a slightly weaker (though still significant) correlation between temporal change of PV ($\partial q/\partial t$) and horizontal advection of PV ($\boldsymbol{u} \cdot \nabla q$) is observed ($R$ = -0.52, $p$ < 0.001; Figure 4.8a) compared to the correlation in the whole OSBL. These correlations highlight the fact that the diabatic and frictional processes have a larger impact on the PV evolution in the convective layer. This is further confirmed by the non-advective PV changes (i.e. $\partial q/\partial t + \boldsymbol{u} \cdot \nabla q$) matching well with the non-advective PV fluxes ($J_z^D + J_z^F$) (Figure 4.8b). In the conditions of downfront wind and cooling, a large fraction of non-advective PV decrease (blue color) is observed. Similarly, non-advective PV increase (red color) is commonly found when there are upfront winds and heating. Also, the non-advective PV changes tend to be small (white color) in the transition between destabilizing forcing and restratifying forcing. This further reflects the importance of diabatic and frictional processes as a leading-order source of PV changes. It is also worth noting that since a significant correlation is obtained between $\partial q/\partial t$ and $\boldsymbol{u} \cdot \nabla q$, it seems to indicate that the PV advection term is also significant in the convective layer.

In contrast, the correlation between $\partial q/\partial t$ and $\boldsymbol{u} \cdot \nabla q$ changes from -0.52 to -0.72 from the convective layer to the intermediate layer (Figure 4.8c), suggesting that the oceanic advective processes are a dominant control on the temporal change of PV below the convective layer. Small residuals ($\partial q/\partial t + \boldsymbol{u} \cdot \nabla q$), as seen by more white-color points in Figure 4.8d compared to Figure 4.8b, imply that the local fluctuation of PV is approximately balanced by the advective PV fluxes. Furthermore, no relationship is observed between the intermediate layer $\partial q/\partial t + \boldsymbol{u} \cdot \nabla q$ and $J_z^D + J_z^F$ from the ocean surface, further indicating that the impact of surface forcing is greatly suppressed below the convective layer. Recent simulations suggest that forced SI is likely to develop below the convective layer and restratify the boundary layer (Taylor and Ferrari 2010). I will further investigate this in Section 4.4.5.

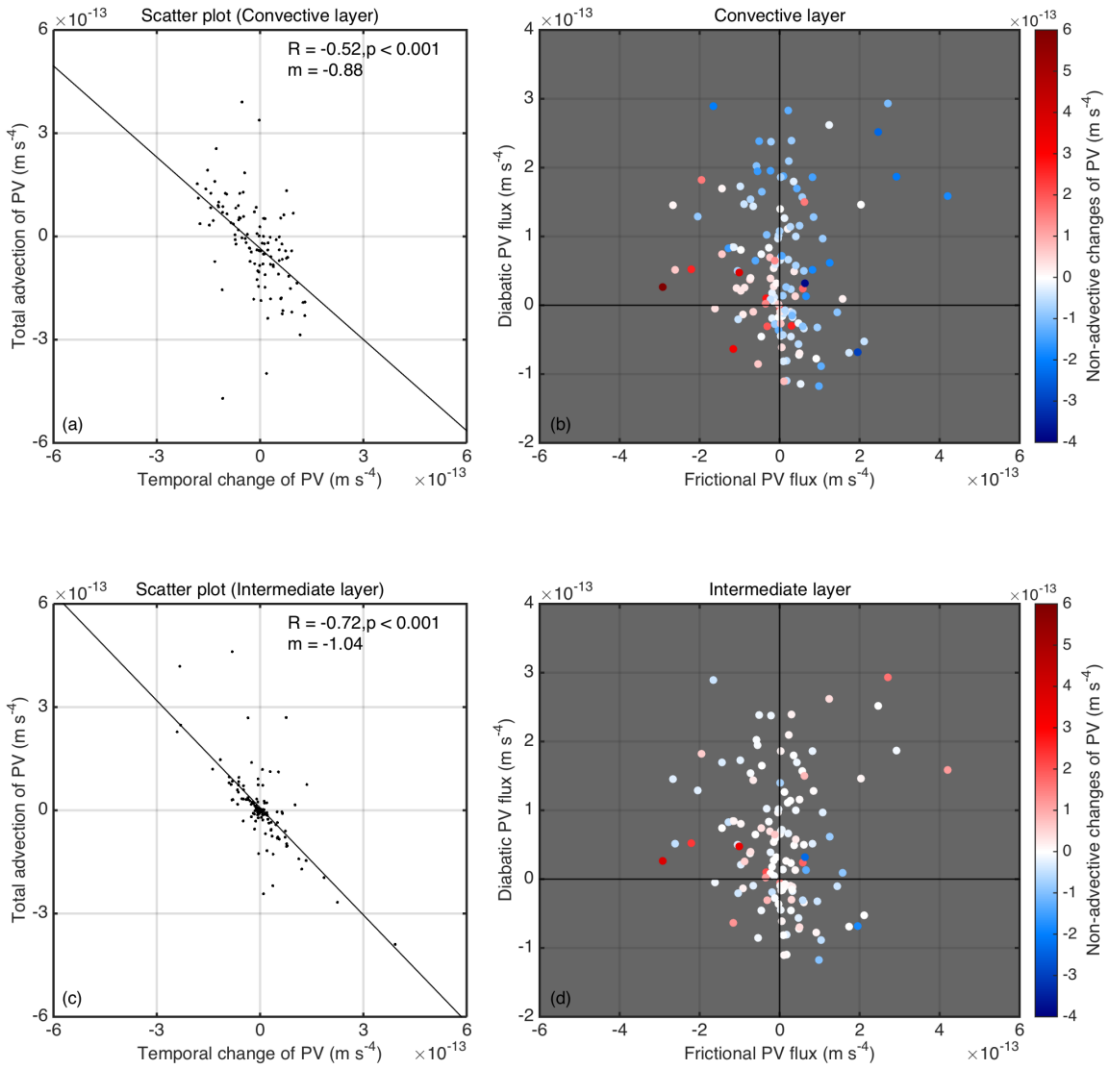


Figure 4.8: (a) Scatter plot of the vertically integrated (all measurements in the convective layer) $\partial q/\partial t$ versus $\boldsymbol{u}\cdot\nabla q$, with the best-fit regression line in black. (b) Scatter plot of $J_z^F$ versus $J_z^D$ colored by the vertically integrated (all measurements in the convective layer) $\partial q/\partial t + \boldsymbol{u}\cdot\nabla q$. (c) Same as (a) but for the intermediate layer. (d) Same as (b) but for the intermediate layer.

### 4.4.4 PV budget below the OSBL

The scatter plot between the temporal change of PV ($\partial q/\partial t$) and the advective PV fluxes ($\boldsymbol{u}\cdot\nabla q$) in the ocean interior (given by vertically integrating from 350 m to the base of the mixed layer) is shown in Figure 4.9a. The linear correlation coefficient between $\partial q/\partial t$ and $\boldsymbol{u}\cdot\nabla q$ is -0.81 ($p$ < 0.001) with the slope of the best-fit line exceeding 0.9, suggesting $\partial q/\partial t$ is well balanced by $\boldsymbol{u}\cdot\nabla_h q$. This is simply a manifestation of the PV conservation for adiabatic, frictionless motion in the ocean interior. The $\partial q/\partial t$ and $\boldsymbol{u}\cdot\nabla q$ exhibit much larger swings in magnitude than their

residuals (i.e., $\partial q/\partial t + \boldsymbol{u} \cdot \nabla q$) because their variations mirror one another. The vertical advection of PV is comparable in magnitude with the horizontal advection of PV, on the order of $10^{-13}$ m s$^{-4}$ (not shown), indicating the non-negligible role of vertical advection of PV in the ocean interior.

To further investigate the relationship between $\partial q/\partial t$ and $\boldsymbol{u} \cdot \nabla q$ in the ocean interior over the annual cycle, I calculate the coherence and phase between the two quantities in Figures 4.9b-c. High coherence is present in the band from about 5-10 days for $\partial q/\partial t$ and $\boldsymbol{u} \cdot \nabla q$. The horizontal advection shows higher coherence with the temporal changes of PV compared to the vertical advection (not shown). The cross spectrum phase also indicates the cancellation between $\partial q/\partial t$ and $\boldsymbol{u} \cdot \nabla q$.

Furthermore, low PV waters are often observed beneath the mixed layer in winter (e.g., March). For the ocean interior, the low PV waters are likely to be sustained by the horizontal advection from regions with deeper mixed layer.

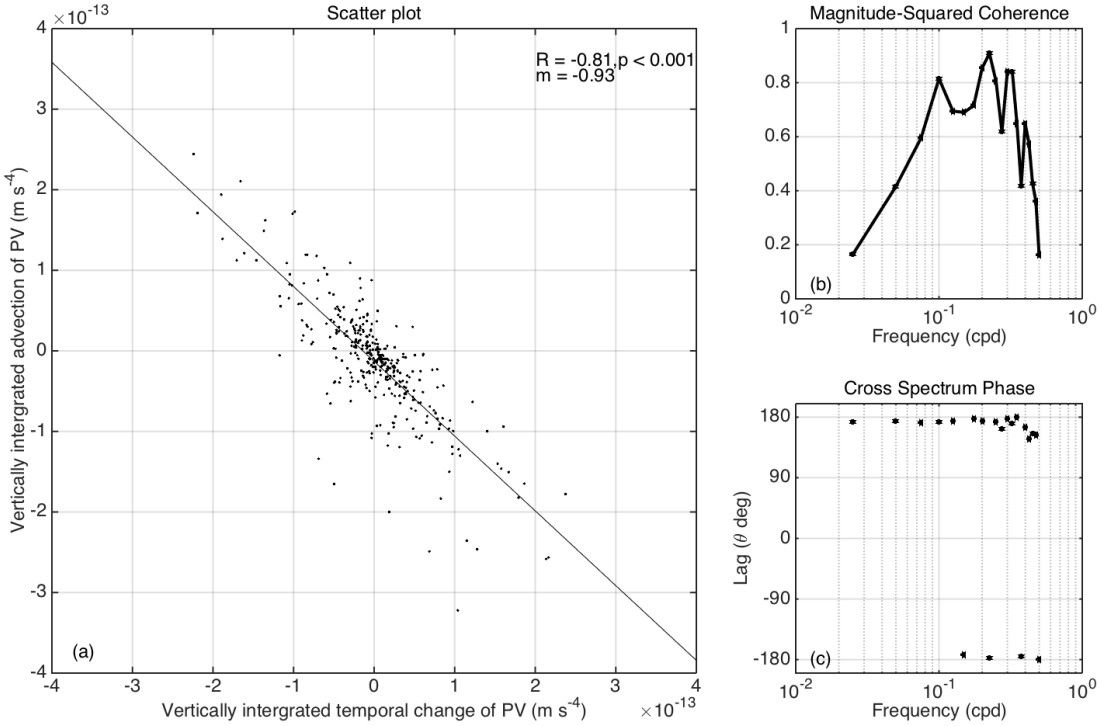


Figure 4.9: (a) Scatter plot of vertically integrated (from 350 m to the base of the mixed layer) $\partial q/\partial t$ versus $\boldsymbol{u} \cdot \nabla q$, with the best-fit regression line in black. (b) Magnitude squared coherence between $\partial q/\partial t$ and $\boldsymbol{u} \cdot \nabla q$, for the same periods in (a). (c) Cross spectrum phase in degree.

### 4.4.5 Submesoscale frontal instabilities in the OSBL

Further insight into the distinct dynamics in the two layers of the OSBL may be

obtained by classification of submesoscale frontal instabilities as described in Section 4.3.3. An important assumption here is that the largest lateral buoyancy gradient within the four triangle regimes of the inner cluster (horizontal resolution of 1.5 km) is chosen to calculate $\phi_{Ri_B}$. This is done because it gives the most intense submesoscale fronts and thus the frequency of symmetric instability in the area delimited by the inner cluster.

Submesoscale instability types in winter and early spring are identified via the balanced Richardson angle analysis, and the time series is divided into five panels (five different months; Figure 4.10). Overturning instabilities occur in the OSBL where PV is less than zero at the mooring site. Both GI and SI are prevalent within the mixed layer, triggered by the unstable stratification and strong baroclinicity, respectively. CI is seldom observed, reflecting weak mean flow and moderate mesoscale eddy activity within the region. Deep mixed layers (up to about 350 m) are common in periods of persistent GI, when small-scale convective turbulence is enhanced and destabilizes the OSBL. SI is often observed just below the area of GI (e.g., beginning of December, 25 December to 5 January), where the lateral buoyancy gradient is strong and vertical stratification is stable but still weak.

The ratio of $h/H$, determined by surface forcing, lateral buoyancy gradient and MLD, is another partially independent indicator of SI apart from the instability types identified by $\phi_{Ri_B}$. The ratio $h/H$ can be used to predict where SI would be more dominant than convection (Taylor and Ferrari 2010; Thomas et al. 2013; Thompson et al. 2016). When $h/H \ll 1$ much of the OSBL is dominated by SI restratification (i.e., slantwise convection), whereas for $h/H \sim 1$ the layer is dominated by vertical convective mixing (i.e., upright convection). Here I synthesize the relationship between $h/H$ and the identified SI-favorable conditions (Figure 4.11). I found that most of the SI-favourable events coincide with low values of $h/H$. The depths of convective and mixed layers are also indicated in Figure 4.10. Conditions favorable for GI reside within the convective layer and become rare below it, while flows with stable stratification but tend to be unstable to SI are often observed in the intermediate layer. Furthermore, the histograms of all instability types in the two layers show this feature more explicitly (Figure 4.12). I also note that there are conditions favorable for SI in the convective layer, but this is much less frequent compared to the intermediate layer. It is assumed that the observed properties are representative of the whole mixed layer. GI is more

likely to occur than SI in the part that not observed by moorings (i.e. top 50 m).

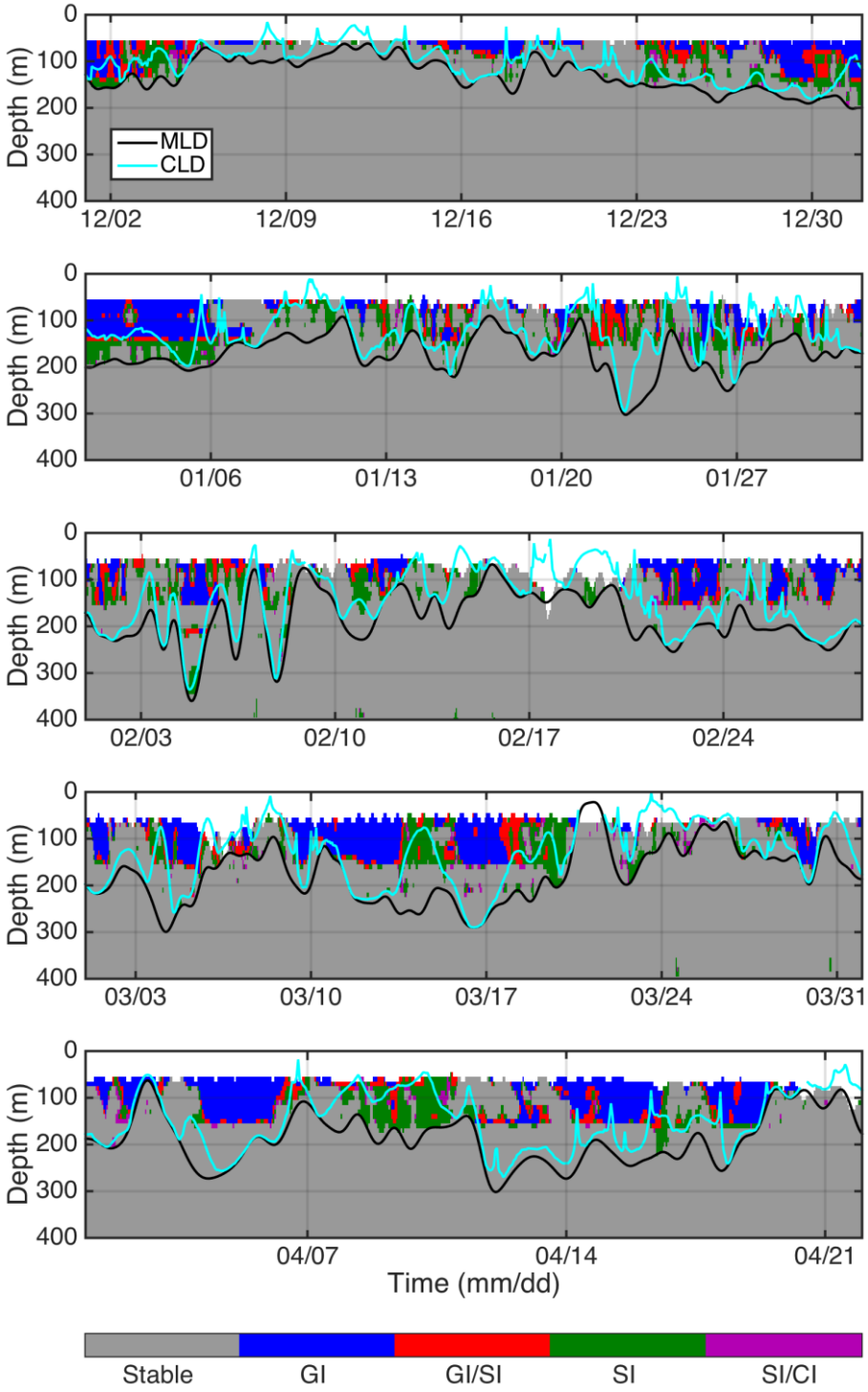


Figure 4.10: Winter time series of submesoscale instabilities occurring when $fq < 0$. Submesoscale instability categories include centrifugal (CI), symmetric (SI) and gravitational instability (GI). The MLD and CLD are superimposed as the black and cyan lines, respectively.

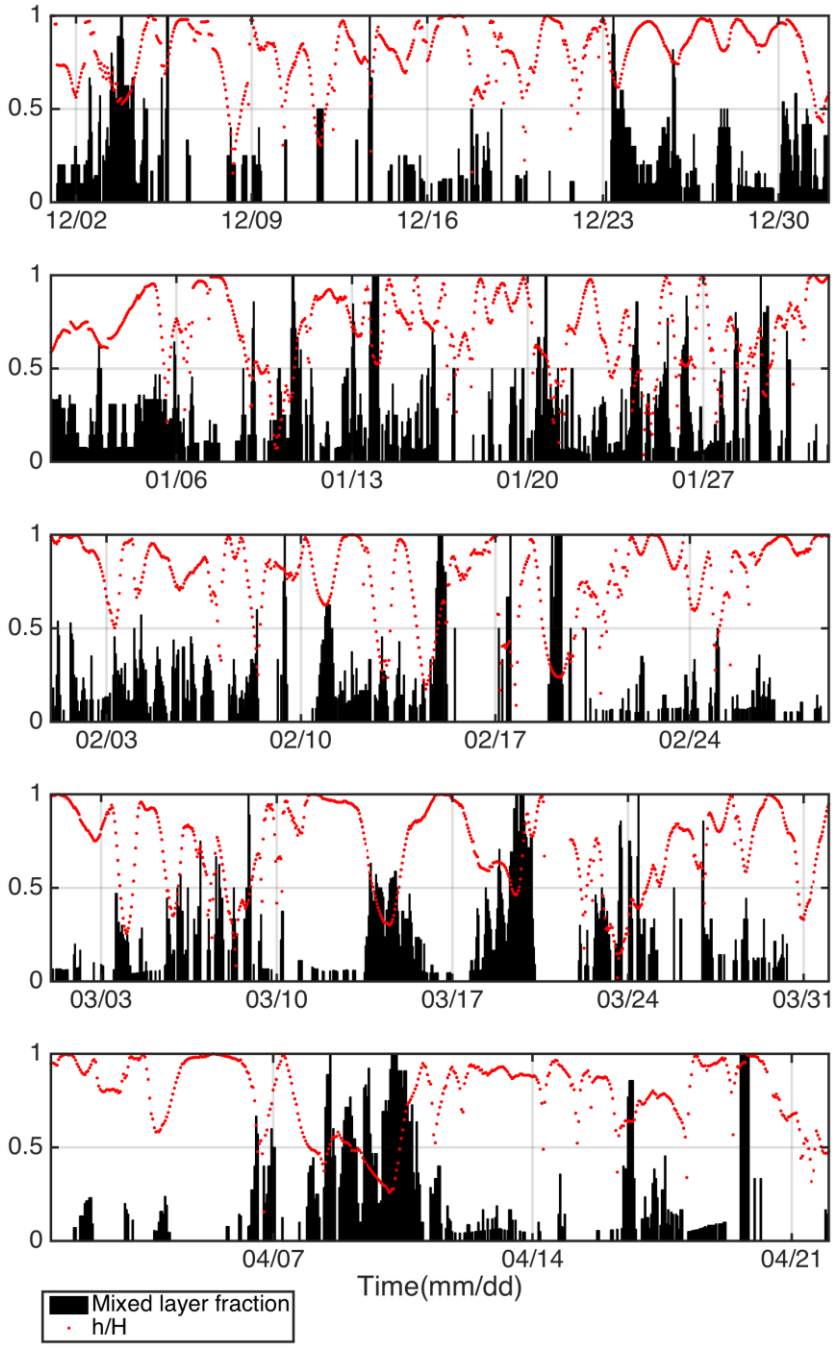


Figure 4.11: Winter time series of the ratio of CLD to MLD ($h/H$, red dots). The black bars represent the fraction of the mixed layer with conditions favorable for SI.

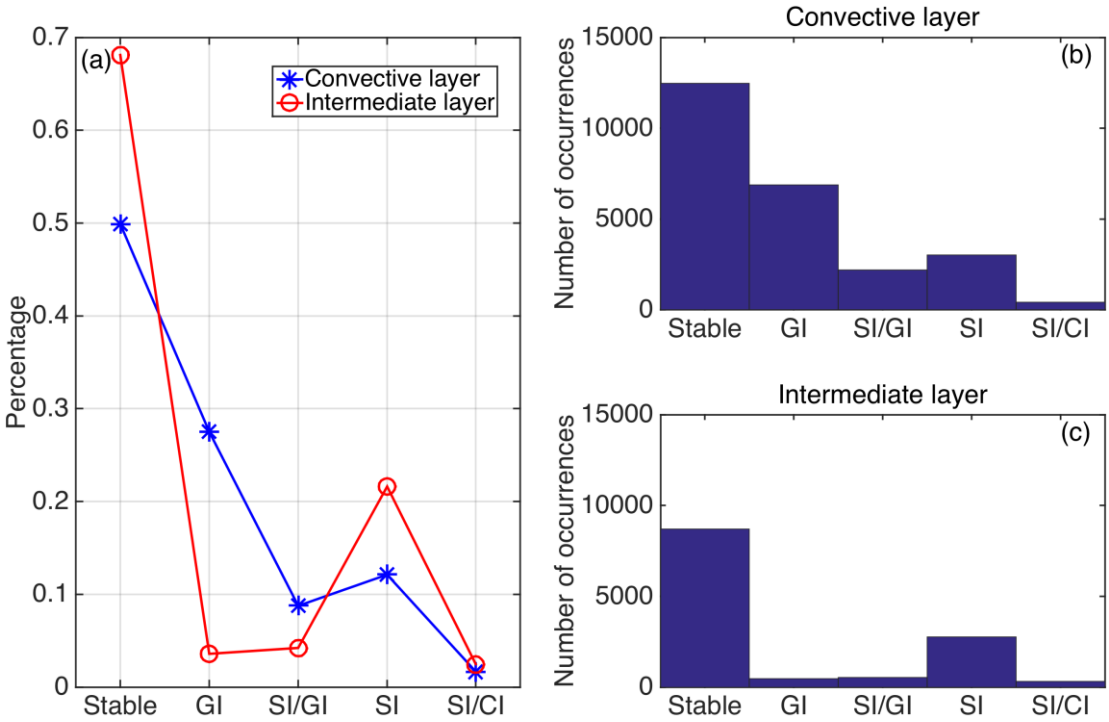


Figure 4.12: Histogram of the occurrence of the overturning instabilities in the convective and intermediate layers, respectively.

### 4.5 Discussion

In the previous sections, I have described the observed PV budget in the upper ocean, and have identified two dynamically distinct regimes in the OSBL from the PV perspective and instability analyses. In this section, I will discuss the dependence of SI on the destabilizing forcing in the study region.

Figure 4.13 shows explicitly the dependence of $h/H$ on atmospheric forcing in the scaling function of the CLD in Taylor and Ferrari (2010). This indicates that, first, $h/H$ decreases (i.e. convective layer becomes a smaller portion of the mixed layer) for a larger positive frictional PV flux generated by downfront winds, but displays a reduced correlation with the diabatic PV flux. Second, note that small $h/H$ occurs around a small value of the destabilizing diabatic PV flux, indicating that weak but destabilizing surface heat fluxes might pre-condition the water column to be susceptible to SI. This is expected from the slantwise convective theory (Taylor and Ferrari 2010). Furthermore, the known phenomenology of SI in the presence of destabilizing surface forcing has been used to parameterize the effects of unresolved SI on a resolved front (Bachman et al. 2017). The parameterization is designed to be sensitive to surface forcing. While these parameterizations have been successfully tested against a set of idealized numerical simulations, *in situ* validations have been difficult to achieve.

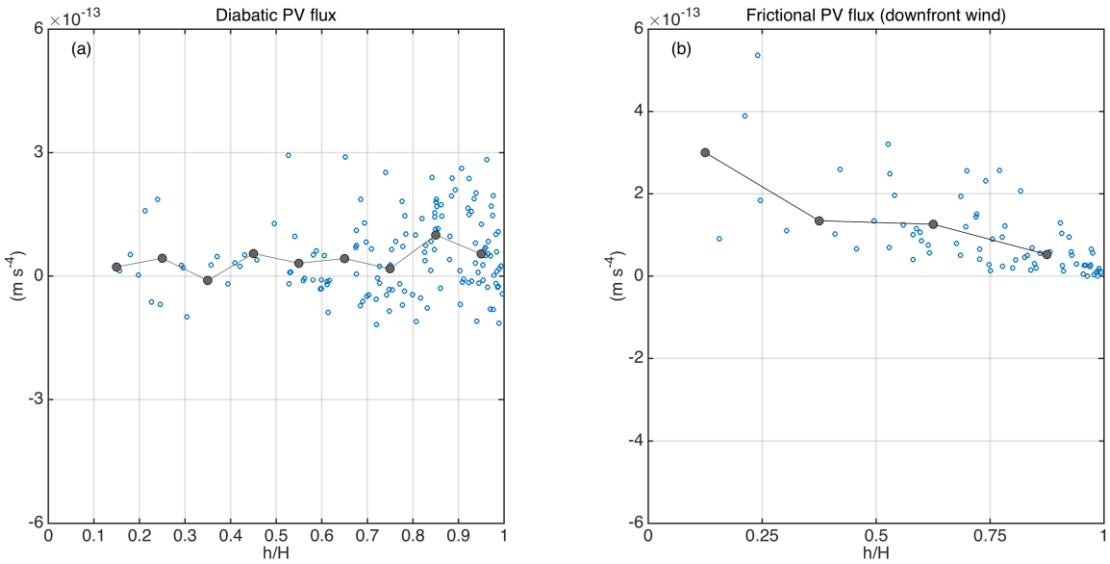


Figure 4.13: Relationship of the CLD to non-advective PV fluxes. The ratio $h/H$ as a function of the diabatic PV flux (a), positive frictional PV flux (b) in winter. Daily-average values for wintertime used. The mean value of the respective PV flux, discretized in respective $h/H$ bins, is given by the filled circles.

A closer look at a strong SI event reveals further characteristic details about SI structure in this region. Figure 4.14 shows time series (3-11 April) of surface flux (in terms of equivalent heat flux), instability types, mesoscale frontogenesis function and mesoscale strain rate. The surface flux is dominated by cooling from 4 to 7 April, during which period the buoyancy loss steadily decreases from its maximum value 200 W $m^{-2}$ to about 50 W $m^{-2}$. Not surprisingly, under such cooling at the sea surface, the PV at the mooring site is negative and unstable to GI. From 7 to 11 April, The EBF, driven by downfront wind, was much larger than the surface heat flux, with a peak equivalent to 650 W $m^{-2}$ of heat loss. Conditions favorable to SI are commonly observed during this period, suggesting a causal link between the surface forcing and the observed PV distribution. Furthermore, the depths of convective and mixed layers are also indicated in Figure 4.14. The small ratio of $h/H$ further supports the condition for SI to be the dominant mode of instability. The strong baroclinicity (i.e. strong horizontal buoyancy gradient) is likely to be associated with persistent frontogenesis induced by the strain field and large confluent flows, as the mooring site located approximately the middle of two mesoscale eddies based on the AVISO SLA data (Figure 4.15).

The case study suggests that SI is likely to be active in the conditions of downfront wind, especially at the time when the surface heat fluxes are weak. This is consistent

with previous studies (Thomas 2005; Thomas et al. 2013). The transition from unstable stratification to weakly stable stratification in the OSBL through destabilizing forcing, combined with lateral buoyancy gradients that arise via eddy straining and frontogenesis, provides conditions favorable for SI. I note that a more definitive measure of SI is to observe comparable geostrophic shear production and the turbulent dissipation rate (e.g., D'Asaro et al. 2011). It is beyond the scope of the present study to quantify the energy transfer associated with the SI.

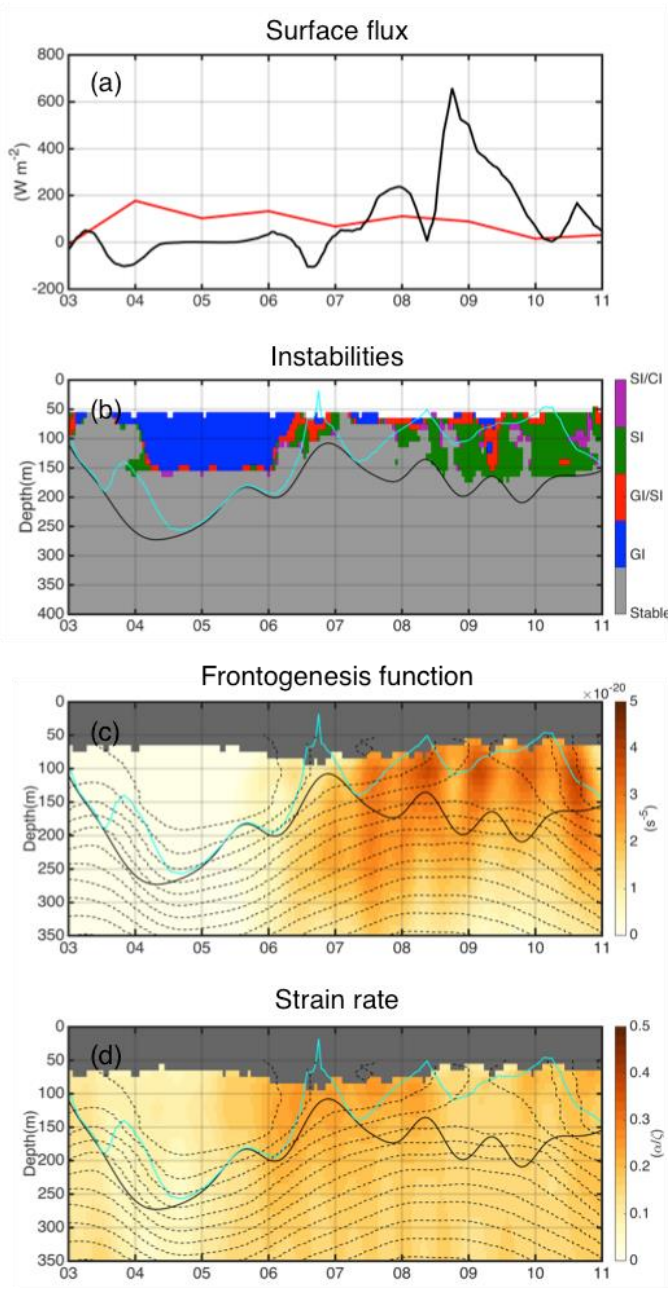


Figure 4.14: Observational evidence of SI on 3-11 April 2013. (a) The heat loss (red) and EBF, expressed in units of a heat flux (black). Positive values of the EBF and heat flux indicate conditions favorable for forced SI. (b) Submesoscale instability categories. (c) Frontogenesis function estimated from the outer mooring measurements. (d) Strain rate estimated from the outer mooring measurements. The MLD and CLD are superimposed in (b-d) as the black and cyan lines, respectively. Isopycnals are overlaid in (c-d) as dashed black lines.

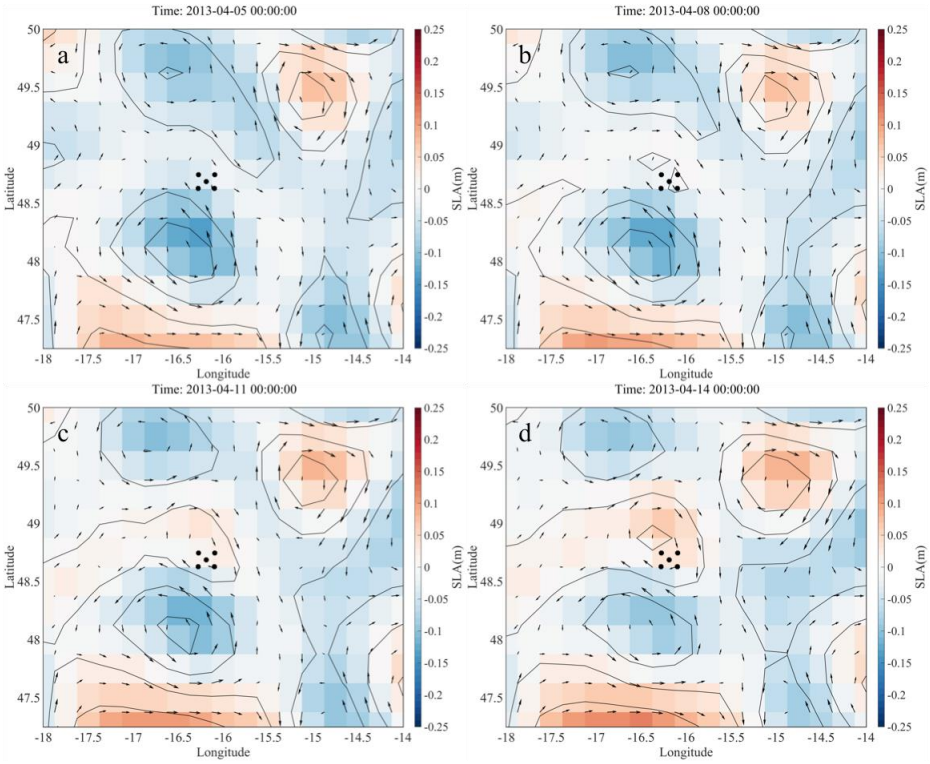


Figure 4.15: SLA anomaly maps with surface geostrophic current velocity (shown as black arrows) near the OSMOSIS site on (a) 5 April 2013, (b) 8 April 2013, (c) 11 April 2013 and (d) 14 April 2013. SLA anomaly contours are overlaid as black lines at intervals of 0.05 m, ranging from -0.25 to 0.25 m. Black dots indicate the OSMOSIS central and outer moorings.

### 4.6 Conclusions

I have presented, for the first time, an observational estimate of the PV budget in the upper ocean over an annual cycle, with a key focus on wintertime when the mixed layer is deep and submesoscale flows are active. The observational site is representative of the open ocean in a mid-latitude, mid-gyre region. The availability of high-fidelity time series allows me to diagnose the characteristics of the OSBL, and to conduct an investigation of the upper-ocean dynamics from the PV perspective, highlighting the respective roles of diabatic and frictional processes. My main conclusions can be summarized as follows:

(i) Diabatic and frictional PV fluxes both contribute significantly to PV evolution in the OSBL: diabatic PV flux has a higher impact on timescales of months, while frictional PV flux has a higher impact on shorter timescales (a few days).

(ii) The local rate of PV destruction in the OSBL during wintertime is set

through the upper boundary forcing, but also changed by horizontal and vertical advection.

(iii) Three-dimensional submesoscale instabilities play a major role in setting the annual cycle of mixed layer deepening and shoaling in the study area.

(iv) The OSBL may be described as a two-layer system: where GI dominates in a convective layer linked to buoyancy forcing, and SI is more prevalent in the part of the mixed layer below the convective layer linked to downfront wind forcing.

The variability in the diabatic and frictional processes has a significant impact on the evolution of PV in the OSBL. Diabatic forcing is the dominant contributor to the seasonal cycle of PV in the study region, determining a persistent deepening of the mixed layer in the fall-winter transition and an abrupt shoaling of mixed layer in the spring-summer transition. Frictional forcing, more intermittent in time, inputs PV into the ocean during periods of upfront wind, or induces conditions favorable for SI during periods of downfront wind. Additionally, in this study, the direct calculation of the frictional PV flux indicates the interaction between surface winds and submesoscale fronts can have an impact, either restratifying or destroying stratification, which is comparable to the diabatic PV flux, especially in winter. In the ocean interior, advection terms dominate the PV recirculation. This is consistent with the idea that below diffusive and viscous boundary layers, the diabatic and frictional terms can be largely ignored and PV acts like a conserved scalar (McIntyre 2015b).

Furthermore, my work also adds to the recent modeling (e.g., Taylor and Ferrari 2010) and observational (e.g., Thomas et al. 2013) evidence for the structure of the OSBL: active symmetric instabilities commonly occur between the upright convective layer and the more strongly stratified interior. The importance of non-advective forcing as a source of PV changes in the convective layer is suggested by the association of the PV reduction with downfront wind and surface cooling, and vice versa. The PV budget in the intermediate layer is similar to the ocean interior, with the leading order balance between the local temporal change of PV and the advection of PV, indicating the oceanic processes there are dominated by the frontal circulations rather than by surface forcing. The results of this study provide evidence that SI is active in a region (i.e., open ocean region with weak mean flows and moderate EKE) that is characteristic of a large portion of the ocean's surface in winter conditions.

# Chapter 5: The Annual Cycle of Wind-Generated Near-Inertial Internal Waves at the PAP site in the Northeast Atlantic

---

This chapter examines the annual cycle of wind-generated NIWs in the mooring site. In particular, a slab mixed layer model and intense measurements from one of the OSMOSIS moorings are used to study the downward propagation of the NIWs. The seasonal variability of near-inertial horizontal KE is also examined.

## 5.1 Abstract

The annual cycle of near-inertial waves (NIWs) is studied using observations from the OSMOSIS moorings located at the PAP site in the Northeast Atlantic Ocean in combination with a mixed layer slab model. Results show that near-inertial kinetic energy (KE) dominates the internal wave band, and is seen radiating predominantly downward in a few strong resonant wind events throughout the year. The elevated near-inertial KE in the upper ocean shows a good match with the wind work driving mixed-layer near-inertial motions estimated from both observations and the slab model. Near-inertial KE is enhanced by at least a factor of 2 in winter compared with that in summer. This seasonality is also reflected in rotary vertical wavenumber spectra of horizontal velocity and vertical shear. Furthermore, the rotary vertical wavenumber spectra exhibit a dominance of clockwise-with-depth energy, suggestive of downward energy propagation and a surface energy source. The substantial downward propagation of wind-generated NIWs may transfer energy to higher-frequency (i.e. higher than the local frequency), high-shear internal waves where dissipation could occur, and thus may play an important role in deep-ocean mixing in the study area.

## 5.2 Introduction

Near-inertial internal waves are a crucial process of the OSBL response to strong resonant wind blowing on the sea surface, and account for a major portion of internal wave energy and shear in the oceans (Pollard 1970; Fu 1981; D'Asaro 1995; Alford 2003a; Silverthorne and Toole 2009; Sun and Pinkel 2012). The energization of the near-inertial motions in the OSBL depends crucially on midlatitude storms (Pollard and Millard 1970; D'Asaro 1985; Zhai et al. 2005), which contain strong inertially rotating components. Once NIWs are excited, near-inertial KE has been shown to radiate downward from the mixed layer into the ocean interior through horizontal convergences and divergences pumping the stratified base of the mixed layer (Gill 1984). Alford et al. (2012) showed that the downward energy flux is comparable to the work done on near-inertial motions in the mixed layer by the wind at ocean station Papa in the North Pacific.

These downward-propagating NIWs play an important role in maintaining the abyssal stratification and energizing higher-frequency internal wave generation in the deep ocean (Gill 1982; Wunsch and Ferrari 2004; Jochum et al. 2013, Alford et al. 2016). More importantly, these higher-frequency internal waves will eventually

become unstable, and induce small-scale turbulence by wave breaking (Polzin 2010; Polzin and Lvov 2011). Kilbourne and Girton (2015) further show that 25% of the average energy flux at the base of the mixed layer might be dissipated before downward-propagating NIWs reach the bottom topography. Zhai (2015) have also shown that the bulk of wind-induced near-inertial energy is strongly latitudinally independent by using a slab model.

The objective of this Chapter is to examine the annual cycle of the downward propagation of wind-generated NIWs at the PAP site in the Northeast Atlantic. The KE contained within the NIWs, and its relationship to the surface wind forcing, is investigated in this study. Discussions of the relationship between the local dissipation in the ocean interior and vertical shear associated with the NIWs and higher-frequency internal waves are given.

The layout of this Chapter is as follows. Section 5.3 describes the data and analysis methods used in this Chapter. In Section 5.4, the reliability of the ECMWF reanalysis winds is demonstrated with the aid of a short period of observed winds near the study region and the slab model. Section 5.5 outlines the annual cycle and depth penetration of wind-generated NIWs at the PAP site. Summary and discussion are given in Sections 5.6.

## 5.3 Data and Methods

### 5.3.1 Data overview

The OSMOSIS mooring measurements and all other available datasets are described in detail in Chapter 2, and only the dataset specifically used in this Chapter will be briefly summarized here.

Measurements from the central mooring, which is the most heavily instrumented among the nine OSMOSIS moorings (also see Table 2.1), are mainly focused on in this Chapter to investigate the downward-propagating wind-generated NIWs in the upper ocean (50 - 520 m) at the PAP site. Data include (i) upper-ocean velocities, temperature and salinity measured by 13 CTD/ACM pairs on the central mooring, (ii) upper-ocean velocities measured by the upward-looking ADCP on the central mooring, (iii) winds measured by the K1 buoy, (iv) ECMWF reanalysis winds at the PAP site, and (v) dissipation estimated from the OSMOSIS gliders.

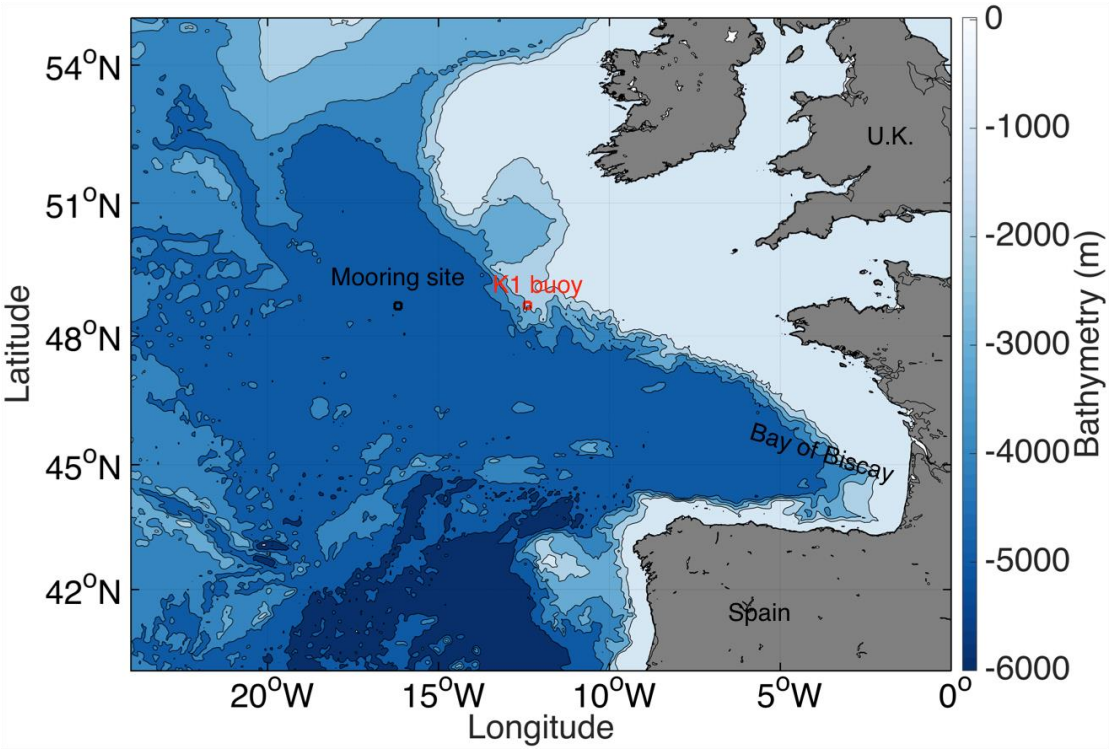


Figure 5.1: OSMOSIS study region in the Northeast Atlantic at the PAP site, September 2012 – September 2013. The European continent is shaded grey, and bathymetry is shown in the colormap on the right. The black and red squares denote the locations of the nine OSMOSIS moorings and the K1 buoy, respectively.

#### 5.3.1.1 Velocity measurements and processing

Horizontal velocity was measured on the central mooring via 13 ACMs and one ADCP in different temporal and vertical resolutions for a complete annual cycle (September 2012 to September 2013). The 13 ACMs spanned the depth interval of 50-520 m with vertical spacing of 20-50 m, and sampled every 10 minutes. The ADCP, with a 75-KHz unit looking upward from about 450 m, measured velocity in 8-m bins and formed ensembles every 60 minutes. Data bins near the ADCP sensor (400 – 450 m depth) and sea surface (0 – 100 m depth) were removed because of side-lobe interference.

Horizontal velocity measured by 13 ACMs was interpolated onto a uniform depth grid (10 m intervals between depths of 50 m and 520 m), and onto uniform 10 minute intervals between 5 September 2012 and 5 September 2013. These 10-minute interval horizontal velocity time series are used in rotary frequency spectral analyses (Figure 5.7). Subsequently, the 10-minute horizontal velocities were averaged onto hourly intervals to match the ADCP and wind measurements.

The ACMs have higher temporal resolution and larger depth range compared to the ADCP, and therefore will be mainly centered on in this Chapter. Nevertheless, the ADCP provides higher resolution in vertical and so is complementary to the ACMs. It will be seen in Section 5.5.3 that the high vertical resolution of the ADCP measurements are particularly valuable to resolve vertical wavenumber spectra, especially for vertical shear spectra (Figure 5.12).

#### 5.3.1.2 Wind dataset and processing

The northern guard buoy for the OSMOSIS moorings contained meteorological sensors, and was deployed at the PAP site on 10 September 2012. Unfortunately, the buoy sank shortly after deployment. The wind data are instead taken from the ECMWF ERA-Interim reanalysis surface wind fields (Dee et al. 2011). Zonal and meridional reanalysis winds are obtained at the grid point closest to the central mooring site with a time interval of 3 hours from 5 September 2012 to 5 September 2013.

A comparison between observed and reanalysis winds at the PAP site is therefore impossible to achieve. Alternatively, wind measurements from the K1 buoy, about 278 km away from the OSMOSIS mooring site (Figure 5.1), are used to validate against the reanalysis wind fields. The K1 buoy sampled at hourly intervals from 5 September to 28 December 2012.

The reanalysis winds were interpolated onto the hourly intervals to match the observed horizontal velocities and winds. Wind speed was converted to stress using speed-dependent drag coefficient (Large and Pond 1981). Furthermore, the spectra of wind stress were computed for each component of the two wind time series. The record from 5 September to 28 December 2012 was separated into 38 three-day half-overlapping windows.

### 5.3.2 Near-inertial motions and wind work

Near-inertial velocities can be expressed as a complex quantity

$$Z_{in} = u_{in} + iv_{in}, \tag{5.1}$$

where $Z = u + iv$ is the complex form of horizontal velocity, and the subscript '$in$' denotes near-inertial component. Near-inertial motions are defined as the velocity in frequency band between $\{0.8,1.2\}\ f$ in this study (also see Figures 5.2 and 5.7). Near-inertial velocities are isolated by means of a forth-order Butterworth filter applied in the time domain. The filter is applied twice, once forward and once backward, to minimize distortion of phase. Following bandpassing, near-inertial KE is quantified as

$$KE_{in} = \frac{1}{2}\rho_0|Z_{in}|^2. \quad (5.2)$$

Additionally, the dot product of the near-inertial surface winds and mixed-layer near-inertial currents is used to determine the wind work on mixed-layer motions,

$$\Pi_{wind} = \boldsymbol{\tau}_{in} \cdot \boldsymbol{u}_{in}. \quad (5.3)$$

This formalism for estimating the energy flux from the wind to NIWs was introduced by D'Asaro (1985). The mixed-layer near-inertial currents are taken from the shallowest available ACMs and ADCP record.

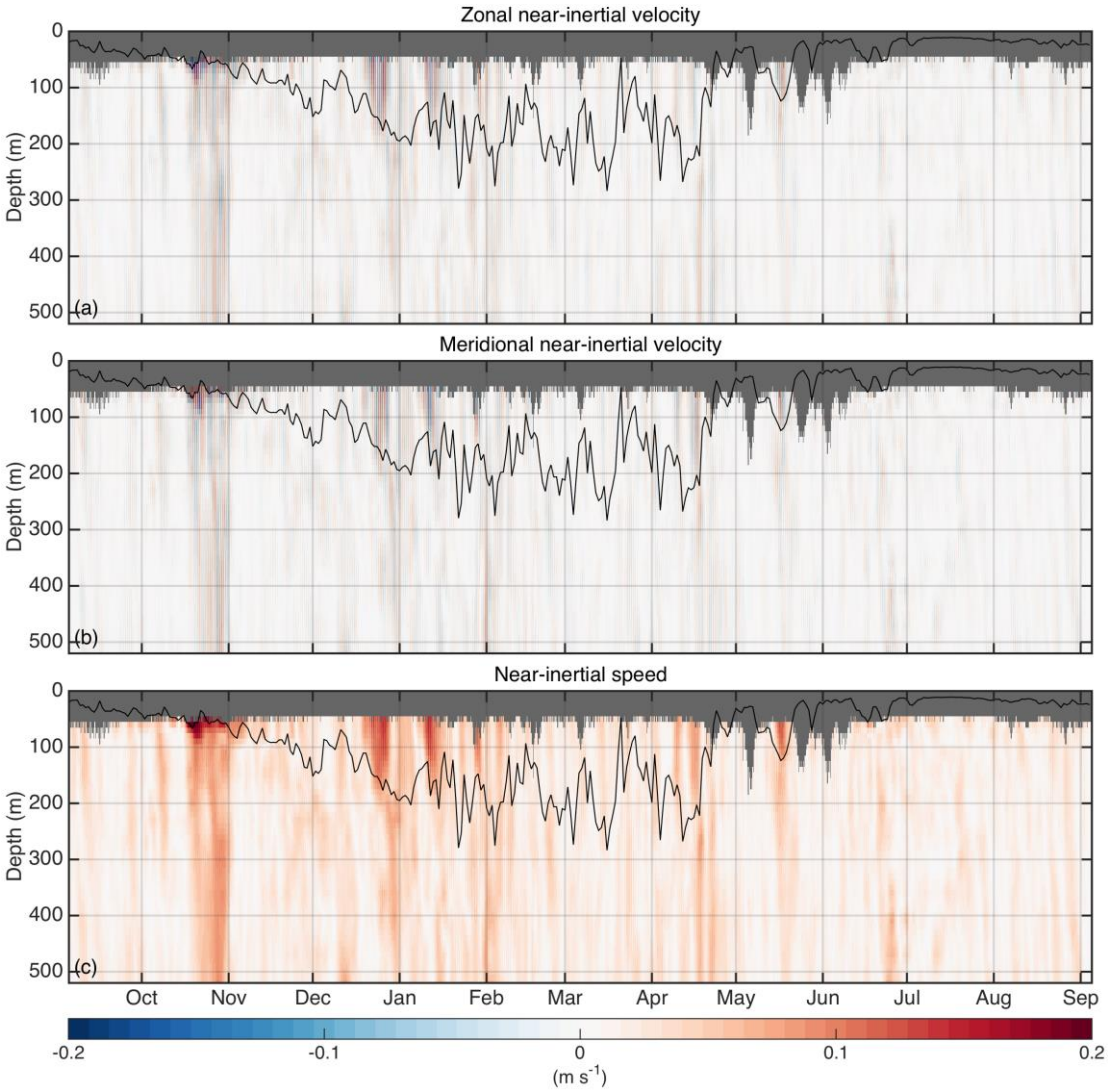


Figure 5.2: (a) Zonal, (b) meridional and (c) the total near-inertial velocities obtained by bandpassing (see text) for the entire year (September 2012 – September 2013) from the ACMs measurements. Black lines in (a-c) indicate the MLD. Depths not sampled by the deployed instrumentation in are colored in grey.

### 5.3.3 Wentzel-Kramers-Brillouin scale

In the ocean, the amplitude and wavenumber of internal waves change with the varying vertical stratification due to refraction as waves propagate vertically through a nonhomogeneous medium (Leaman and Sanford 1975). 'Wentzel-Kramers-Brillouin (WKB) scale' and 'WKB stretch' are usually applied to correct for the influence of vertical variations of the Brunt–Väisälä frequency on the vertical propagation of internal waves (e.g., Alford et al. 2012, and many others). Here, each time series of horizontal velocity is WKB scaled using annual-mean climatological buoyancy frequency computed at the central mooring (Figure 5.3).

To account for amplitude changes, WKB-scaled near-inertial horizontal velocity is computed as

$$Z_{in}^{WKB}(z) = Z_{in}(z)/[N(z)/\bar{N}]^{1/2}, \tag{5.4}$$

and WKB-scaled near-inertial KE is computed as

$$KE_{in}^{WKB} = \frac{\bar{N}}{N(z)} KE_{in}, \tag{5.5}$$

where $N(z)$ is the buoyancy frequency, $\bar{N}$ = 2.8 × $10^{-3}$ $s^{-1}$ is the mean climatological stratification computed between 50 and 520 m.

To account for vertical wavenumber changes, WKB-stretched depth is computed as

$$z^{WKB} = \int_{50}^{z} \frac{N(z)}{\bar{N}} dz, \tag{5.6}$$

where $z^{WKB}$ is the stretched coordinate. Quantitative calculations such as the vertical wavenumber spectrum are computed in the stretched coordinates.

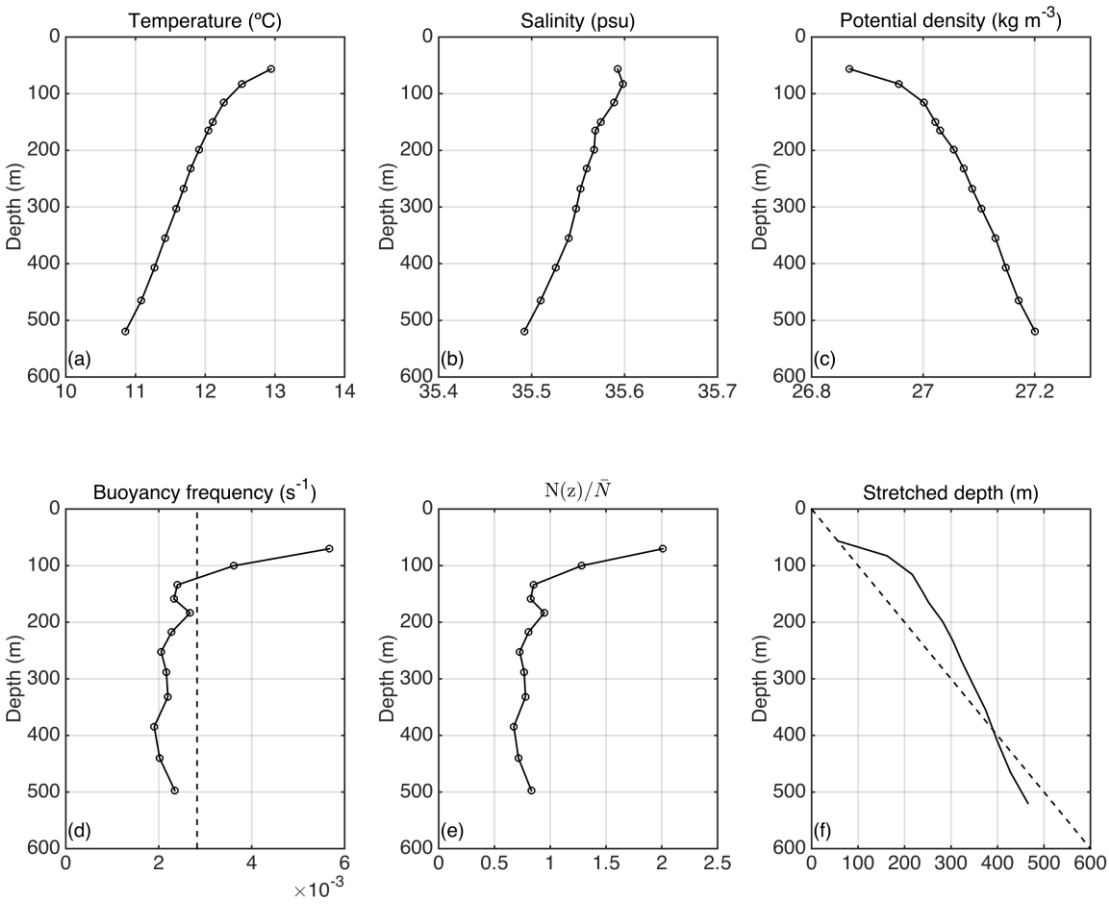


Figure 5.3: WKB scaling and stretching calculations. Year-mean (a) temperature, (b) salinity, (c) potential density, and (d) buoyancy frequency at the central mooring site. Dashed line in (d) indicates the mean buoyancy frequency from 50 - 520 m. (e) The WKB scaling factor $N(z)/\bar{N}$. (f) WKB-stretched depth. The dashed line in (f) indicates the unstretched depth for reference.

### 5.3.4 Spectral analysis

#### 5.3.4.1 Rotary frequency spectrum

Horizontal velocity can be decomposed into rotary components, which is particularly useful in separating near-inertial energy from other velocity components (Mooers 1973). Following Gonella (1972), rotary frequency spectra of horizontal velocity are estimated from time series of measurements from the ACMs (10-minute) and the ADCP (hourly), respectively. To do so, the depth-resolved time series of horizontal velocity are first WKB-scaled. Rotary spectra are computed at each depth using the sine multitaper method (Riedel and Sidorenko 1995), and then averaged together over depth. The counter-clockwise (CCW) and clockwise (CW) components of the frequency spectrum are presented in Figure 5.7.

#### 5.3.4.2 Rotary wavenumber spectrum

The understanding of the vertical propagation of NIWs through the water column can be gained by computing vertical wavenumber spectra of horizontal velocity and vertical shear. As for frequency spectra, the rotary vertical wavenumber spectra of horizontal velocity and vertical shear are also calculated from the ACMs and the ADCP measurements, respectively. Following, e.g. Leaman and Sanford (1975), several steps are taken to calculate the vertical wavenumber spectra: first, vertical averages of each horizontal velocity profile are removed; second, the record-mean horizontal velocity is removed at each depth; third, horizontal velocity is scaled under the WKB scaling as described in Section 5.3.3; finally, gaps in the time records are zero-filled. These gaps are mainly caused by mooring motion, and only account for less than 1% of the mooring record.

The rotary spectral decomposition is computed for each velocity profile, and the resulting spectral estimates are averaged over periods of interest (the whole year, winter and summer) and shown in Figures 5.11-12.

### 5.3.5 The slab model

Directly estimating wind work on the mixed-layer motions would require simultaneous measurements of the mixed-layer near-inertial currents and wind stresses at the sea surface. These are difficult to achieve and rarely available for in-situ observations, especially for time periods over months. A simple slab model, developed by Pollard and Millard (1970), has been found particularly appropriate for reproducing near-inertial motions in the mixed layer from time series of wind alone (Alford 2003b; Plueddemann and Farrar 2006). Essentially, the slab model represents reduced physics in the mixed layer by assuming properties are vertically uniform (vertical property gradients within the surface mixed layer are small compared to the gradients between the mixed layer and the upper pycnocline) and horizontal homogeneous. The corresponding equations (i.e. the vertically integrated momentum equations) are expressed as

$$\frac{du}{dt} - fv = \frac{\tau_x}{H\rho} - ru, \tag{5.7a}$$

$$\frac{dv}{dt} + fu = \frac{\tau_y}{H\rho} - rv, \tag{5.7b}$$

where $r$ is damping constant that parameterizes the transfer of energy from the mixed layer to the ocean interior; $\tau_x$ and $\tau_y$ are the zonal and meridional components of wind

stress on the ocean surface, respectively; $H$ is the MLD, and $\rho$ is the density of sea water. Based on previous work (e.g., D'Asaro 1985; Alford 2001), $r^{-1}$ is usually set to be 2-20 days. Here I use a damping factor $r = 0.04f$ ($r^{-1}$ ~ 16.7 days), as determined empirically by fitting slab model output to ACMs-measured currents.

The complex form of Equation 5.7 is more widely used, and expressed as

$$\frac{dZ}{dt} = -\omega Z + \frac{T}{H}, \tag{5.8}$$

and

$$T = \frac{\tau_x + i\tau_y}{\rho}, \tag{5.9}$$

$$\omega = r + if, \tag{5.10}$$

where $Z = u + iv$ is the horizontal velocity, $T$ is the surface wind stress divided by the reference density. Modeled mixed-layer velocity is proportional to the inverse of the MLD, which is normally taken from a climatology (D'Asaro 1985; Alford 2001, 2003b; Watanabe and Hibiya 2002; Jiang et al. 2005). Kilbourne and Girton (2015) suggest that climatological MLDs significantly misrepresent the ocean response to impulsive wind forcing when the upper-ocean buoyancy gradient is small. Therefore, the 10-day smoothed MLD estimated from the OSMOSIS gliders is used for all slab-model calculations here. The slab model is solved using the traditional time-stepping method in D'Asaro (1985), which gives very similar results to the spectral solution (Alford 2003b).

Following D'Asaro (1985), the solution of $Z$ has two components: 'Ekman' and inertial,

$$Z = Z_E + Z_I. \tag{5.11}$$

The first term on the RHS of Equation 5.11, defined as

$$Z_E = \frac{T}{\omega H}, \tag{5.12}$$

denotes a steady Ekman transport to the right of the wind. The second term on the RHS of Equation 5.11,

$$Z_I = Z - Z_E, \tag{5.13}$$

is associated with anticyclonic circular motions at the local inertial frequency. Given the wind stress at times $t$ and $t-1$

$$Z_{I_t} = Z_{I_{t-1}} e^{-\omega\Delta t} - \frac{\Delta T}{H\omega^2}(1 - e^{-\omega\Delta t}). \tag{5.14}$$

Here, $Z_I$ responds primarily to inertial-frequency wind motions that rotate inertially, that is, CW (CCW) in the Northern (Southern) Hemisphere.

It is worth noting that the slab model is usually used to model mixed-layer currents from observed winds, because the long-term observed mixed-layer velocity data are more likely unavailable. However, the situation is opposite here. Reanalysis winds are used to drive the mixed-layer slab model, and then to compute the flux using the reanalysis winds and the model mixed-layer currents in Equation 5.3. These model results are compared with the direct calculation of the flux by reanalysis winds and observed mixed-layer velocities (Section 5.5.2). Furthermore, I also evaluate the slab model using both the K1-buoy observed and reanalysis winds to validate the reanalysis winds (Section 5.4). Note that observed winds are only available from 5 September to 28 December 2012.

## 5.4 Validation

Before presenting the results, the reliability of the ECMWF reanalysis winds will be demonstrated in several ways. First, correspondence between the reanalysis and K1-buoy winds will be shown via direct comparison of the time series and by spectral analysis. In addition, the mixed-layer currents and the resultant fluxes from the slab model driven by the reanalysis winds will be compared to those estimated from the observed mixed-layer near-inertial currents and winds.

### 5.4.1 Comparison of reanalysis and buoy winds

The comparison and spectra of the reanalysis and observed winds are shown in Figure 5.4. The zonal and meridional wind stresses estimated from the ECMWF reanalysis product match fairly well with the observed winds at the K1 buoy. Observed winds exhibit more high-frequency variability than reanalysis winds, which typically has coarser temporal resolution. The spectra indicate that the 3-hourly reanalysis wind time series are reduced in amplitude (relative to observed winds) at frequencies higher than about $10^{-1}$ cph, which is largely an artefact of the interpolation. For frequencies lower than $10^{-1}$ cph, reanalysis and observed winds have approximately equal spectra. Also noteworthy, reanalysis winds are highly coherent ($> 0.8$) with observed winds for temporal scales over a few days, but are not significantly coherent at the inertial frequency (not shown).

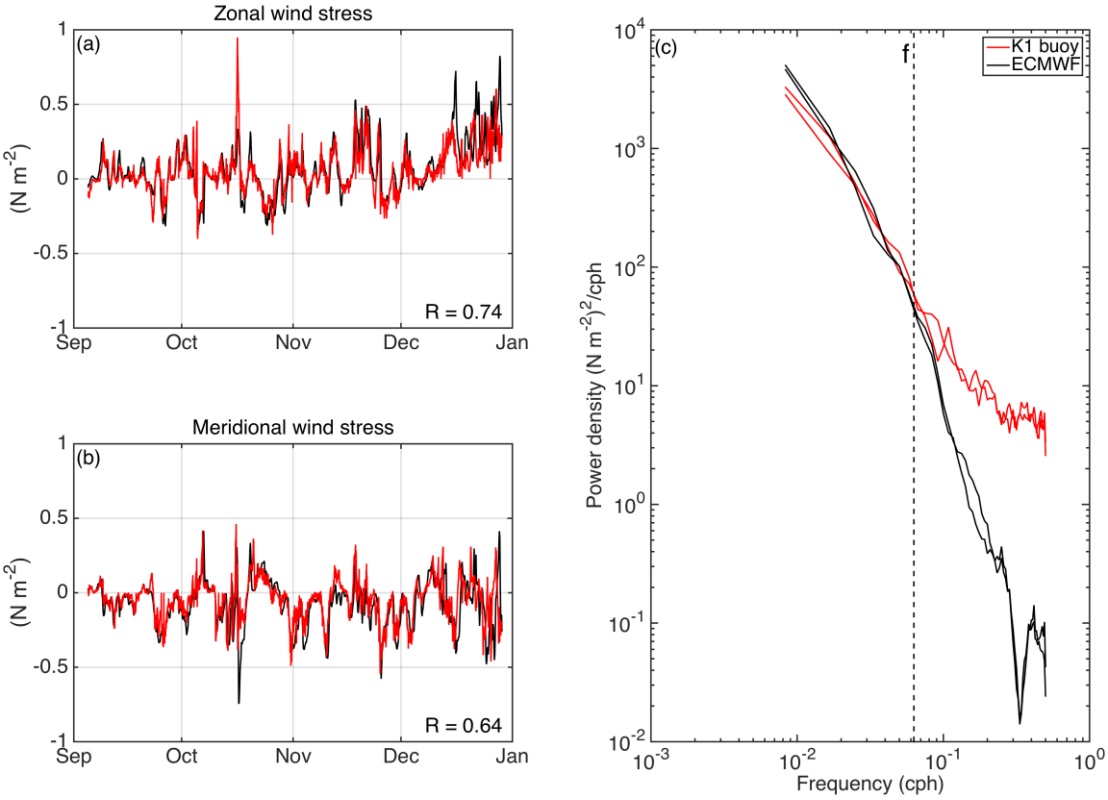


Figure 5.4: Comparison of the ECMWF reanalysis winds (black) with observed winds (red) from the K1 buoy from September 2012 to January 2013. Time series of (a) zonal and (b) meridional wind stress. (c) Power spectra of wind stress from reanalysis and observed winds. The local inertial frequency is shown by the dashed vertical line in (c).

### 5.4.2 Comparison of reanalysis and K1-buoy energy fluxes

The next step is to demonstrate that the mixed-layer currents resulting from the slab model are consistent with observed mixed-layer near-inertial currents, and their respective energy fluxes are comparable in phase and magnitude. The comparison results and a closeup plot are shown in Figures 5.5 and 5.6, respectively.

The cumulative wind work estimated from the slab model has the same order of magnitude as results estimated from observations, with a value about 3 kJ $m^{-2}$ (Figure 5.5b). The slab model forced by either reanalysis or K1-buoy winds is able to largely reproduce the wind-work evolution estimated from the respective direct calculations. Note that the slab model always shows a persistently positive KE flux, resulting in a positive transfer of energy from the wind to mixed-layer motions. Two distinct NIWs events are identified (Figure 5.5c), during which significant increase in the cumulative wind work can be seen.

Wind work in terms of energy flux and the associated cumulative wind work

estimated from observed currents and observed winds, reanalysis winds, and the slab model driven by the reanalysis winds all give comparable results and very similar trend (Figures 5.6a-b). The difference in wind work between reanalysis and buoy-observed winds might be caused by the reanalysis winds cannot capture high-frequency (i.e. higher than $f$) signals. Observed and modeled mixed-layer near-inertial velocities show good agreement in phase and magnitude (Figure 5.6c). Near-inertial meridional velocity indicates a near-inertial packet radiating downward to about 520 m over the next few days (28-31 December 2012), with the magnitude of near-inertial velocity reaching 0.1 m $s^{-1}$ (Figure 5.6d).

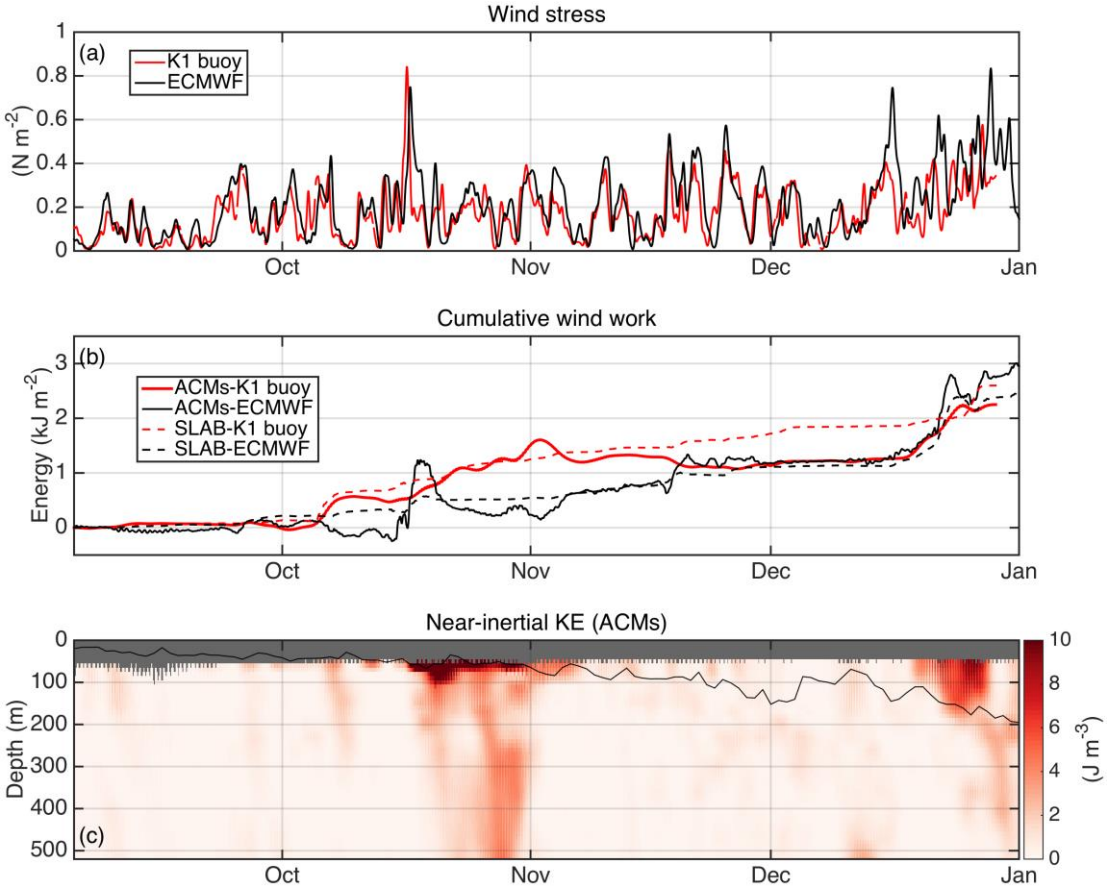


Figure 5.5: (a) Time series of wind stress estimated from the K1 buoy (red) and the reanalysis (black) winds. (b) The time integral of the energy flux into near-inertial motions $\int \Pi_{wind} dt$, computed from observed mixed-layer near-inertial currents and observed (red solid line) and reanalysis winds (black solid line), and from the slab model driven by observed (red dashed line) and reanalysis (black dashed line) winds. (c) Near-inertial KE measured by the ACMs. Black lines in (c) indicate the MLD. Depths not sampled by the deployed instrumentation in are colored in grey.

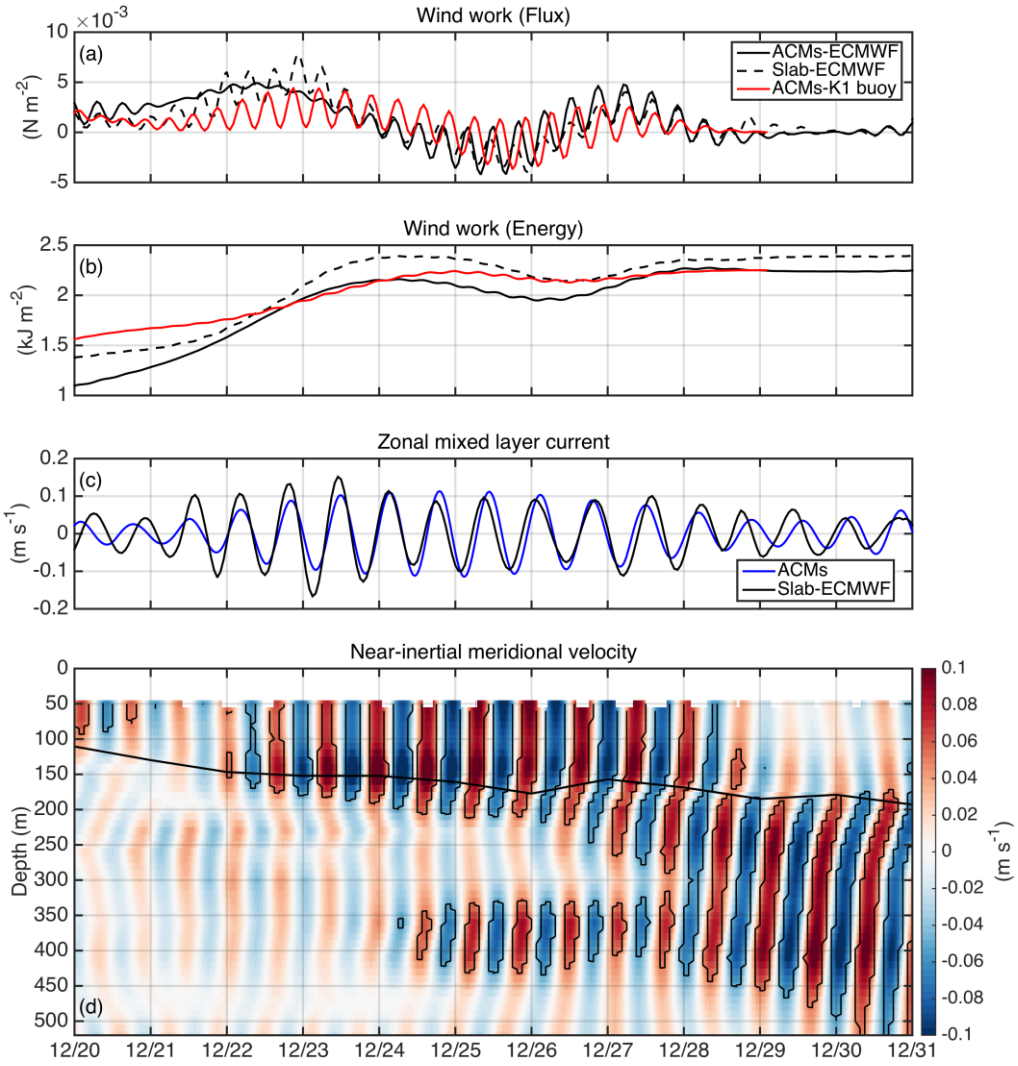


Figure 5.6: Observed and modeled wind work and upper-ocean currents during one NIWs event (20 - 31 December 2012). (a) Energy flux into near-inertial motions ($\Pi_{wind}$) from observed mixed-layer near-inertial currents and reanalysis winds (black solid line), observed mixed-layer near-inertial currents and observed winds (red solid line), and slab model driven by reanalysis winds (black dashed line). (b) The time integral of (a) showing the cumulative energy input to the mixed layer from each flux estimate. (c) Zonal mixed-layer near-inertial current from the top ACM sensor (blue), and zonal mixed-layer current estimated from the slab model driven by reanalysis winds (black). (d) Near-inertial meridional velocity from the ACMs. Black contours mark the velocity of 0.05 m $s^{-1}$.

## 5.5 Results

### 5.5.1 Characterization of NIWs at the PAP site

The depth-averaged rotary frequency spectra of WKB-scaled horizontal velocity $Z^{WKB}$ at the central mooring are shown in Figure 5.7. The spectra are highly resolved by the high temporal resolution of the yearlong measurements from the ACMs. The striking feature is the prominent peak rising near the inertial frequency (so-called inertial peak) for CW motions but not for CCW motions, indicating near-inertial flows are strongly CW polarized at the PAP site. This is consistent with the general characteristics of NIWs in the Northern Hemisphere (Alford et al. 2016). Furthermore, the CW spectral estimates are significantly larger than the CCW estimates at lower frequencies in the internal wave band (e.g., $M_4$ tidal frequency to 0.8 $f$), as expected for linear internal waves.

Rotary spectra of $Z^{WKB}$ at the PAP site match fairly well with the universal continuum internal wave spectrum proposed by Garrett and Munk (1975) (as modified by Cairns and Williams 1976, hereafter referred as GM76). Spectrum density peaks are also present at the $M_2$, $M_4$, $K_1$ tidal frequencies, where CW polarization is also found. Geostrophically balanced flows largely span the range of frequencies approximately lower than the diurnal tides ($K_1$), but display no obvious polarization.

Returning to Figure 5.2, which shows the resulting near-inertial velocity measured from the ACMs, NIWs are an important component of the velocity fields at the study region, especially in the mixed layer. Near-inertial velocities with magnitudes of 0.05-0.15 m/s are commonly seen throughout the year. This is comparable in magnitude with the global average velocity of NIWs, which is about 0.1 m $s^{-1}$ (Park et al. 2005; Chaigneau et al. 2008). The strongest near-inertial velocities usually occur in wintertime of the year, dominated by events of a few days duration.

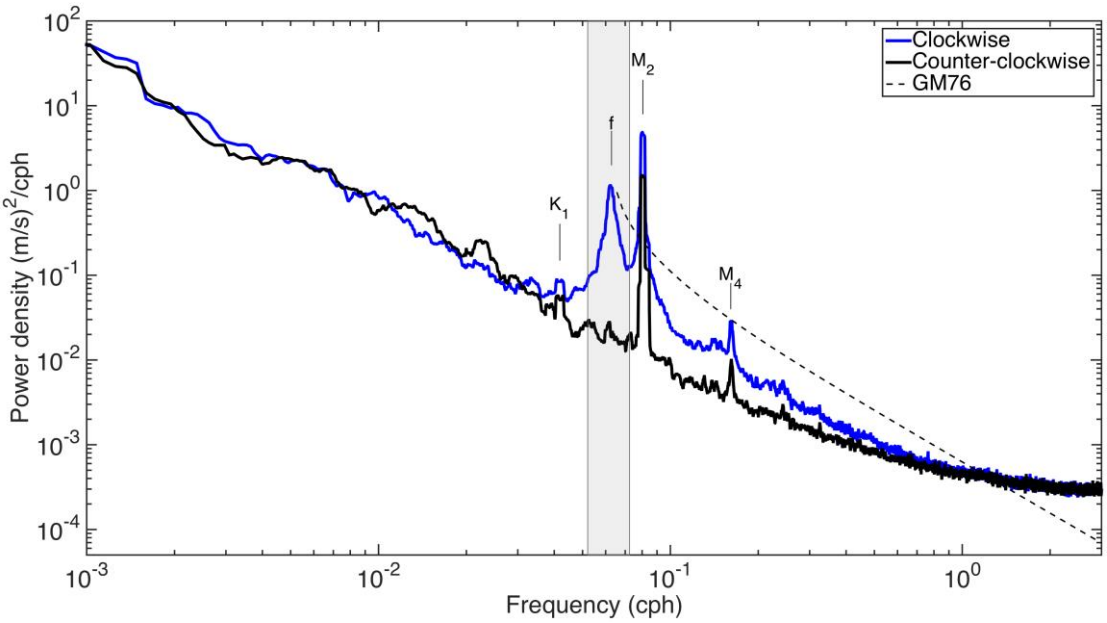


Figure 5.7: Rotary frequency spectrum of WKB-scaled horizontal velocity measured by the ACMs on the central mooring with the time period September 2012 – September 2013. The CW and CCW components of the spectrum are blue and black, respectively. The GM76 model spectrum is indicated by a black dashed curve. The inertial peak (1/15.91 cph), $M_2$ (1/12.42 cph), $K_1$ (1/23.93 cph) and $M_4$ (1/6.21 cph) tidal peaks are marked. The light grey shaded regions indicate the near-inertial band used in bandpass filters to isolate near-inertial signals.

To have a closer look at the depth dependence of the vertical propagation of NIWs on frequency, the region near $-f$ versus depth is plotted in Figure 5.8. A broad range of frequencies, $-$ (0.97-1.03) $f$, can be seen at depth above 200 m, which is in the mixed layer for part of the record, then the peak sharpens before broadening again at both lower and higher frequencies in the water column. These features are captured by both the ACMs and the ADCP. However, no clear blue shift to higher frequencies is observed in the depth range between 50 and 520 m at the PAP site, indicating NIWs might be strongly influenced by local sources. Near-inertial motions propagated from higher latitudes might be still possible, but I am unable to comment on that based on available measurements. The inertial peak is in the range of -(0.97-1.03) $f$, most likely affected by background vorticity field.

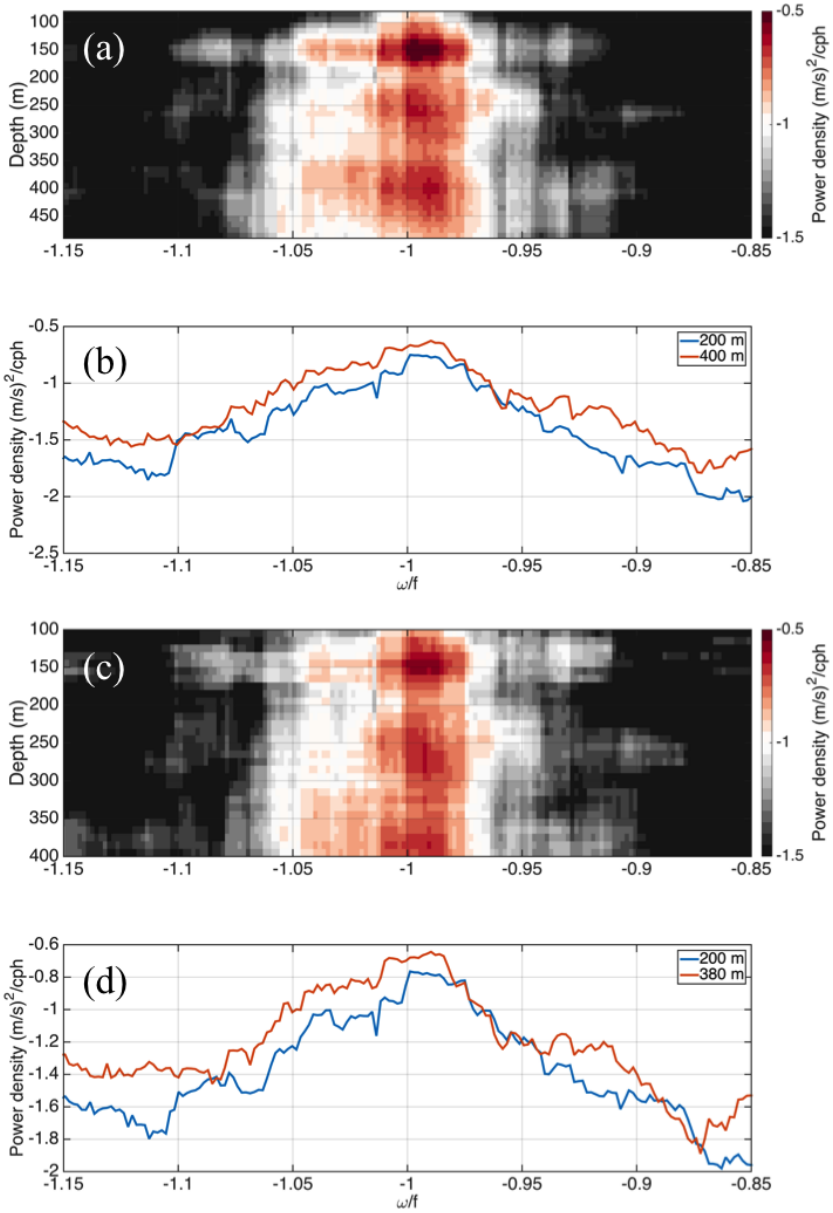


Figure 5.8: (a) Rotary frequency spectrum of WKB-scaled velocity estimated from the ACMs vs depth, zoomed in around the CW near-inertial frequency. The horizontal axis is normalized by $f$. (b) Line plots of the spectrum at the 200 and 400 m depths. (c) Same as (a) but for ADCP velocity. (d) Same as (b) but for ADCP results at the 200 and 380 m depths.

The contribution of near-inertial signals to the total KE at the PAP site is examined by averaging over the year-long record, consisting of the near-inertial, semidiurnal, mean-flow, eddy, and the total KE (Figure 5.9). The annual mean of the total KE attains a maximum value of approximately 28 J $m^{-3}$, and the amplitude gradually decreases with depth, reaching about 16 J $m^{-3}$ at 520 m depth. The total KE is overwhelmingly

dominated by EKE, which is one order of magnitude larger than other components. This is really not surprising because geostrophic mesoscale eddy fields account for a major portion of the ocean KE (Ferrari and Wunsch 2009).

Near-inertial signals are the second largest component and show a strong surface intensification, with the amplitude exceed 2 J $m^{-3}$ at 50 m and steadily decrease from 50 m to 200m, below which the near-inertial KE remains uniformly low around 0.4 J $m^{-3}$. The surface intensification of near-inertial KE indicates NIWs at the PAP site are likely linked to a source near the surface. In contrast, Semidiurnal KE does not exhibit much variation with depth, and is comparable in magnitude with the KE associated with the mean flow, with a depth mean value of approximately 0.15 J $m^{-3}$. Near-inertial KE is substantially larger than the KE associated with semidiurnal tides, indicating near-inertial signals are the most energetic component in the internal wave field in the study area.

Though some energy of NIWs might be dissipated to shear-driven turbulence at the base of the mixed layer, the surface intensification of near-inertial KE is also likely caused by WKB refraction. The WKB-scaled quantities are plotted in Figure 5.9b, and show much less of this feature (i.e. KE decays with depth at the top 200 m). The respective contributions from each component are quantitatively similar to these before WKB-scaled.

In summary, NIWs at the PAP site are strongly characterized by clockwise-polarized velocities, and dominate the KE in the internal wave spectrum, with velocities reaching up to 0.15 m $s^{-1}$. The dominance of NIWs in the internal wave spectrum is consistent with prior work (Ferrari and Wunsch 2009). I next investigate the relationship between wind work and these energetic NIWs in the upper ocean.

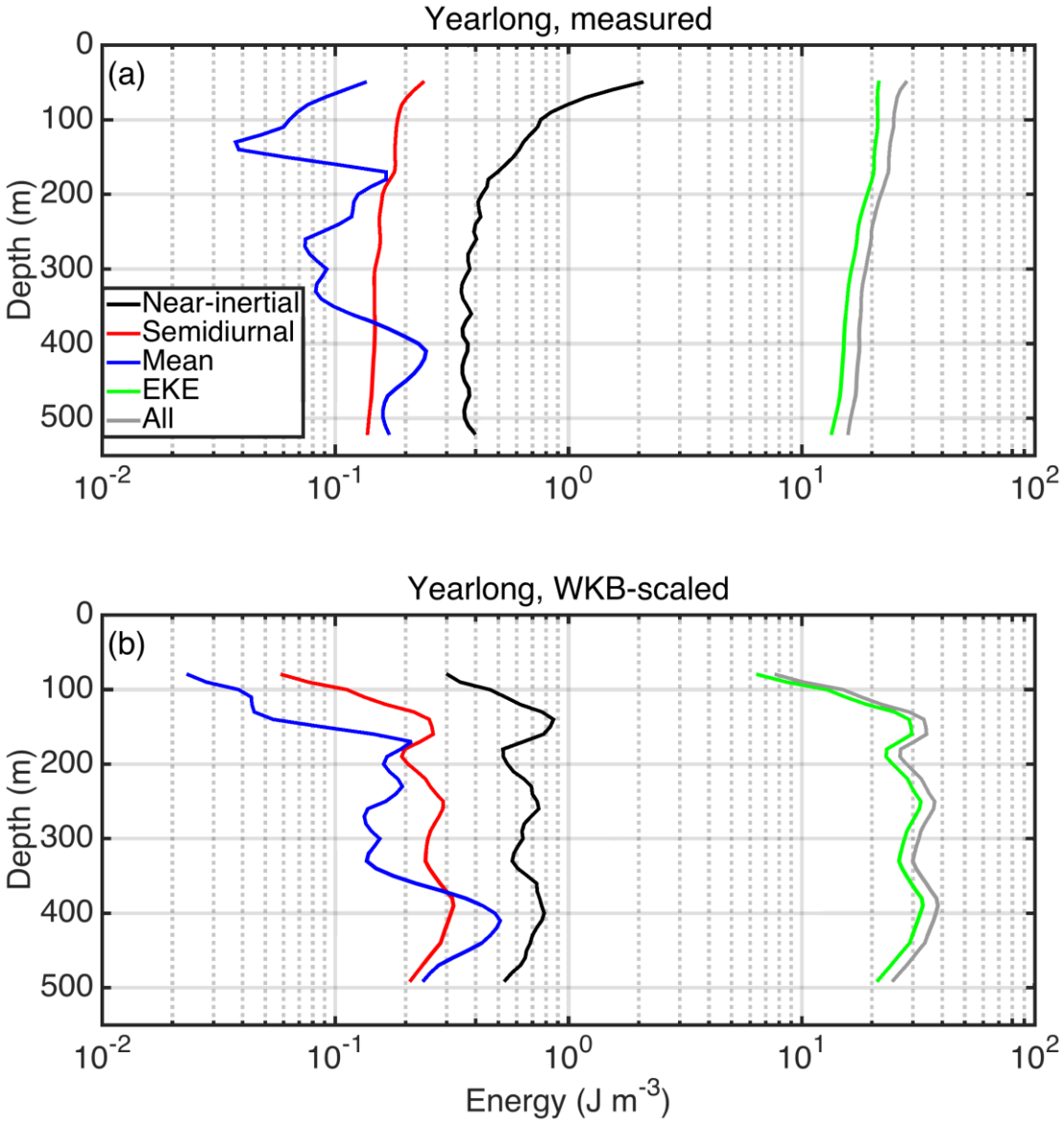


Figure 5.9: (a) Observed and (b) WKB-scaled year mean KE profiles. The total KE is shown by the grey line, and the four components (near-inertial, semidiurnal, mean and EKE) are indicated by the black, red, blue and green lines, respectively.

### 5.5.2 The annual cycle of the wind energy flux and near-inertial KE

Wind work in terms of energy flux (i.e. wind-forced mixed layer energy flux), the time integral of energy flux, and observed near-inertial KE are shown in Figure 5.10. Wind work is very temporally intermittent, with most of wind input dominated by a few events, consistent with near-inertial velocities. Wind energy flux is highly variable during each event, so the cumulative wind work is also computed. The cumulative wind work $\int \Pi_{wind} dt$ shows a distinct 'staircase' structure during the periods of strong resonant forcing. This phenomenon is also reproduced well by the slab model forced

by reanalysis winds. The increase of cumulative wind work coincides well with the elevated near-inertial KE (e.g., end October; end December; mid January) in the upper ocean, especially in the mixed layer. The enhancement of near-inertial KE in the mixed layer seems to decay with depths, the manner in below the mixed layer shown as a set of discrete downward and rightward swaths, suggestive of downward radiation. This vertical decay might be caused by refraction. A similar pattern of near-inertial KE can be also seen from ADCP data (not shown).

The RMS of near-inertial KE from the ACMs measurements is O (1 J $m^{-3}$), with peak values of O (10 J $m^{-3}$). The yearly time integral of wind work, estimated from ACMs current and reanalysis winds, reached to about 8 kJ $m^{-2}$, a factor of 5 smaller than values of ~40 kJ $m^{-2}$ observed at ocean station Papa in the Northeast Pacific which is at a similar latitude and also on the eastern side of an ocean basin (Alford et al. 2012). Shallow MLD (~100 m in winter) at the Papa station is likely to be the main reason of this difference. Both wind work and near-inertial KE show enhanced values in winter and spring (i.e. from December to May), indicating a seasonal cycle of wind-generated NIWs. Interestingly, these enhanced near-inertial KE events also have a good correspondence with strong wind stress (not shown), although many instances of strong wind stress in periods with weak NIWs and wind work are also observed.

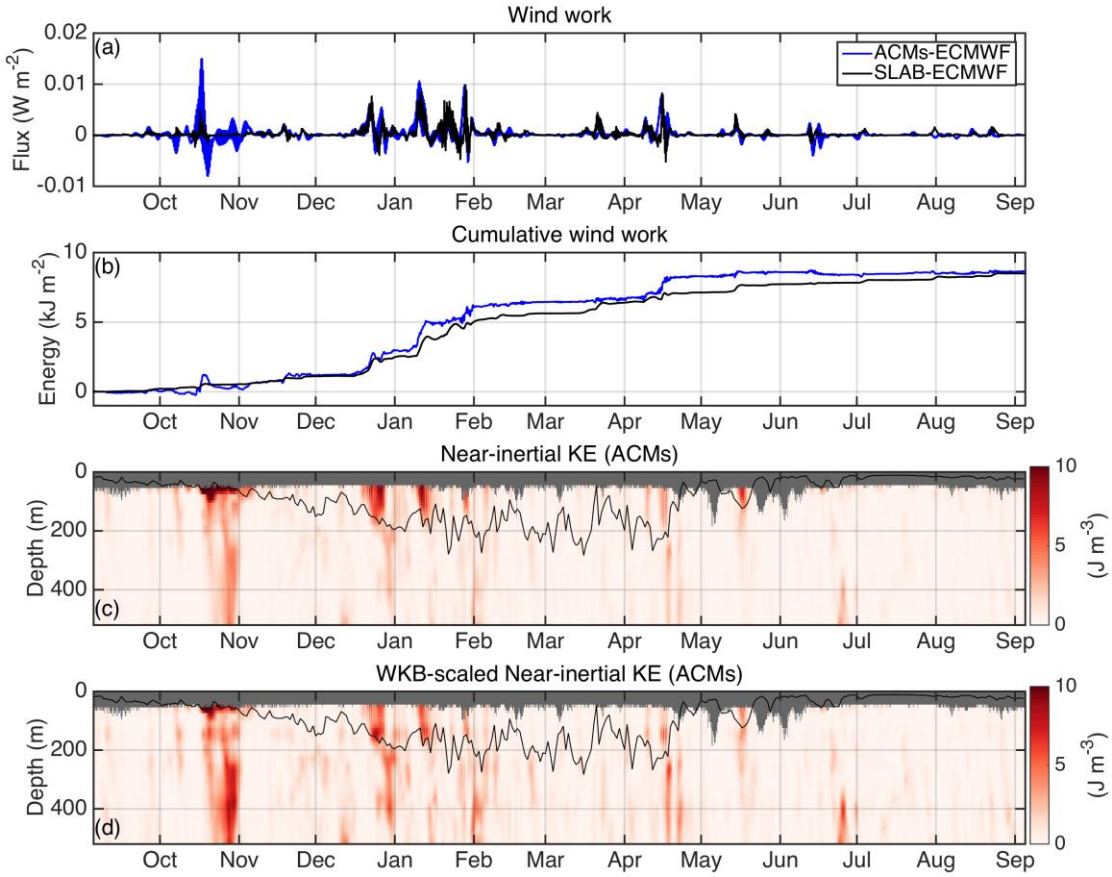


Figure 5.10: (a) Wind energy flux into near-inertial motions $\Pi_{wind}$ computed from the ECMWF reanalysis winds and observed mixed-layer near-inertial currents (blue), and from the slab model driven by the reanalysis winds (black). (b) The time integral of (a) showing the cumulative energy input to the mixed layer from each flux estimate for the central mooring deployment period. (c) Near-inertial KE observed from the ACMs at the central mooring. (d) WKB version of the near-inertial KE in (c). Black lines in (c-d) indicate the MLD. Depths not sampled by the deployed instrumentation in are colored in grey.

### 5.5.3 Seasonality

#### 5.5.3.1 Vertical wavenumber spectra of observed velocity

The rotary vertical wavenumber spectra of the WKB-scaled near-inertial velocity $Z_{in}^{WKB}$ are shown in Figure 5.11. The spectra reveal that the near-inertial velocities are red in vertical wavenumber, and dominated by CW turning with depth motions (looking down from above), indicative of downward propagating energy of low-frequency internal waves. This is especially true for vertical scales larger than 100 m (i.e., vertical wavenumber smaller than $10^{-2}$ cpm), consistent with typical vertical wavelength of

NIWs (Alford et al. 2016). The year-mean rotary spectra are generally in good agreement with the GM76 for vertical scales larger than 100 m, with dominance of the CW component from both the ACMs and the ADCP measurements. However, for vertical scales smaller than O (100 m), the spectra seem to be better resolved by the ADCP measurement, as suggested by the ACMs spectra much smaller than GM76. It is most likely due to the relatively lower vertical resolution of the ACMs measurements compared to the ADCP measurements on the central mooring.

The spectra also exhibit marked differences between winter and summer: NIWs energy is significantly higher in winter than in summer. This seasonal difference is reflected in the amplitude of the spectrum density, mostly at vertical scales larger than 100 m. Consistent with the year-mean spectra, the CW energy is greater than the CCW energy in both seasons. In winter, the CW spectra are clearly higher than the GM76 spectrum and the CCW spectra are slightly lower than that. In summer, the CW spectra roughly match the GM76 spectrum, and the CCW spectra are much lower than that.

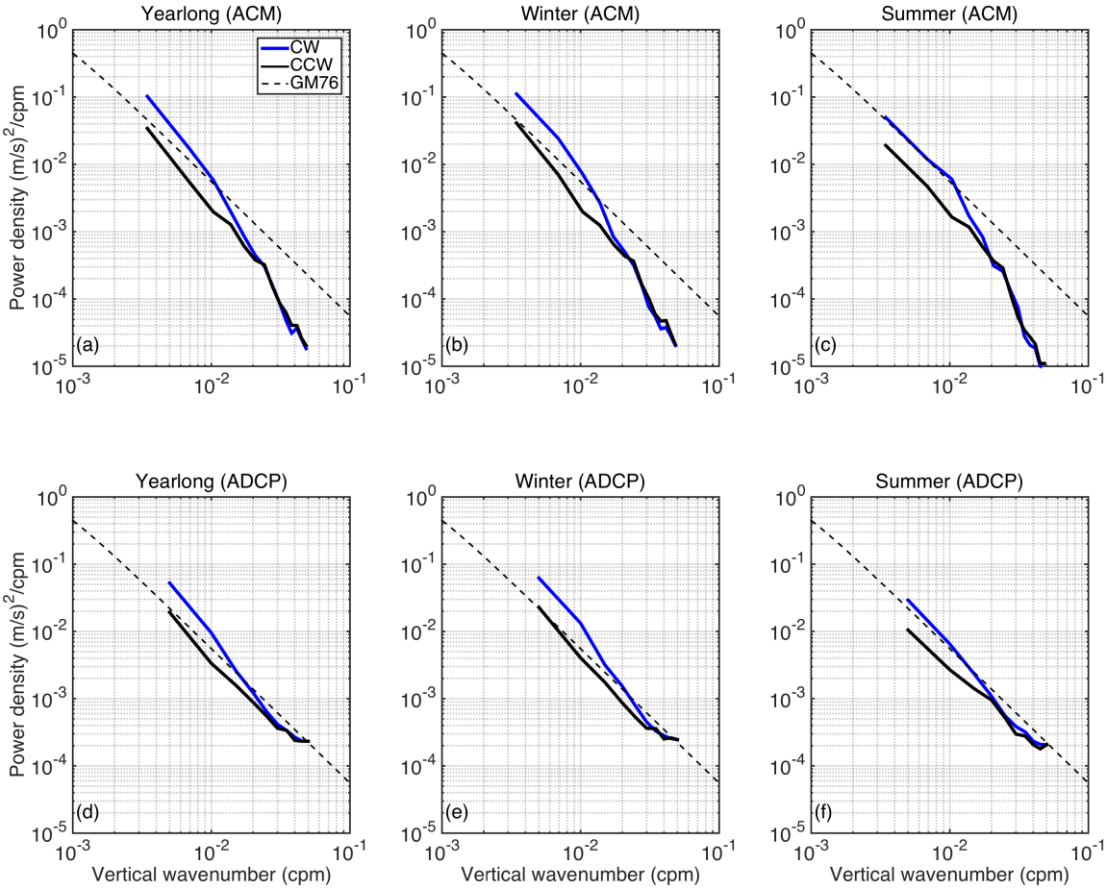


Figure 5.11: Rotary vertical wavenumber spectra of the WKB-scaled near-inertial velocity profiles from (top) the ACMs and (bottom) the ADCP measurements, showing the CW (blue) and the CCW (black) components. The GM76 spectrum is indicated with black dashed line. The (left) year-long, (middle) wintertime and (right) summertime horizontal velocity spectra are calculated as the mean of respective period.

### 5.5.3.2 Vertical wavenumber spectra of observed vertical shear of horizontal velocity

The rotary vertical wavenumber spectra of the WKB-scaled vertical shear are also computed from the ACMs and ADCP measurements, respectively (Figure 5.12). The results from ACMs and ADCP display a quite different shape, mostly due to ADCP's ability to resolve higher vertical wavenumber. The vertical wavenumber spectra of shear accentuate the higher vertical wavenumbers compared with velocity spectra (Alford et al. 2016). Therefore, I will focus on the spectra estimated from ADCP measurements.

The shear spectra containing near-inertial wave signals significantly depart from the spectral levels predicted in the GM76 of the typical background internal wave field. Much of the energy at ~80-300 m vertical wavelengths comes from the near-inertial

peak. The vertical wavenumber shear spectra estimated from the ADCP data are blue for vertical wavelengths larger than about 80 m, and red over the vertical scale range from 50 to 80 m. This feature holds true for both summertime and wintertime data subsets. In contrast, the GM76 is white at this range and does not resolve NIWs well. However, the feature of vertical wavenumber spectra of shear with a hump in the wavenumber range above the white GM76 spectrum is not well captured by the ACMs data, which have lower resolution compared with the ADCP data.

Consistent with rotary vertical wavenumber spectra of the WKB-scaled near-inertial velocity, the CW component of vertical shear in winter contains more energy than the summertime CW component at typical near-inertial vertical scales O (100 m). It is also noteworthy that the CCW components (i.e. upward energy propagation) in winter and summer are similar in magnitude.

In summary, these spectra confirm that NIWs are dominated by downward-propagating waves, and more energetic in winter than in summer. In addition, discrete current meters at single depths find it difficult to capture the vertical structure of NIWs.

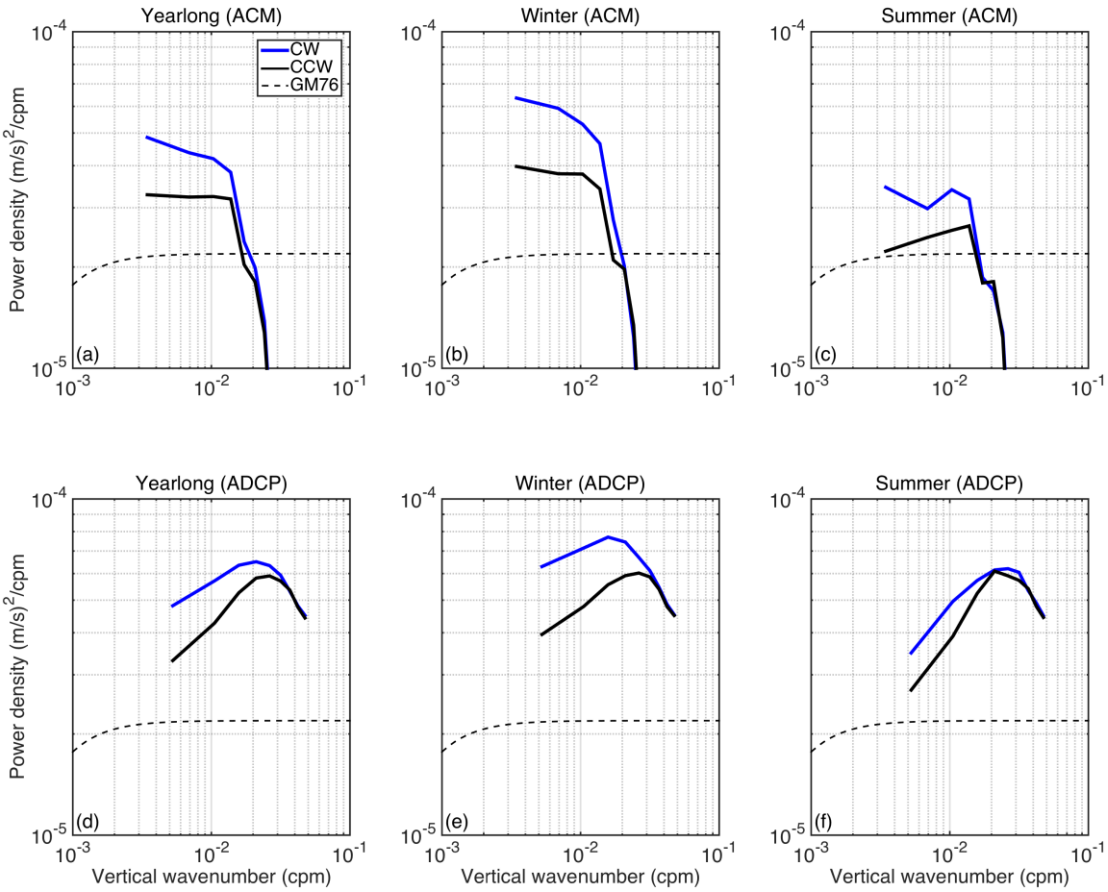


Figure 5.12: Rotary vertical wavenumber spectra of the WKB-scaled vertical shear profiles from (top) the ACMs and (bottom) the ADCP measurements, showing the CW (blue) and the CCW (black) components. The GM76 spectrum is indicated with dashed line. The (left) year-long, (middle) wintertime and (right) summertime vertical shear spectra are calculated as the mean of respective period.

### 5.5.3.3 Energy profile

The seasonality of NIWs is also reflected in the KE profiles (Figure 5.13). Near-inertial KE in winter is similar in shape but generally a factor of 2 larger than that in summer. The maximum value of wintertime near-inertial KE is about 1.5 J m$^{-3}$ at 50 m depth, much larger than KE associated with semidiurnal tides and mean flows. The typical near-inertial KE displays a strong intensification in the upper 200 m of the water column in winter, and upper 100 m in summer, roughly coinciding with their respective mean MLD. In summer, when wind forcing is weak, near-inertial KE is similar in magnitude with KE associated with semidiurnal tides and mean flows, especially for the WKB-scaled values. Furthermore, the KE associated with mean flows are comparable with semidiurnal KE, both in summer and winter.

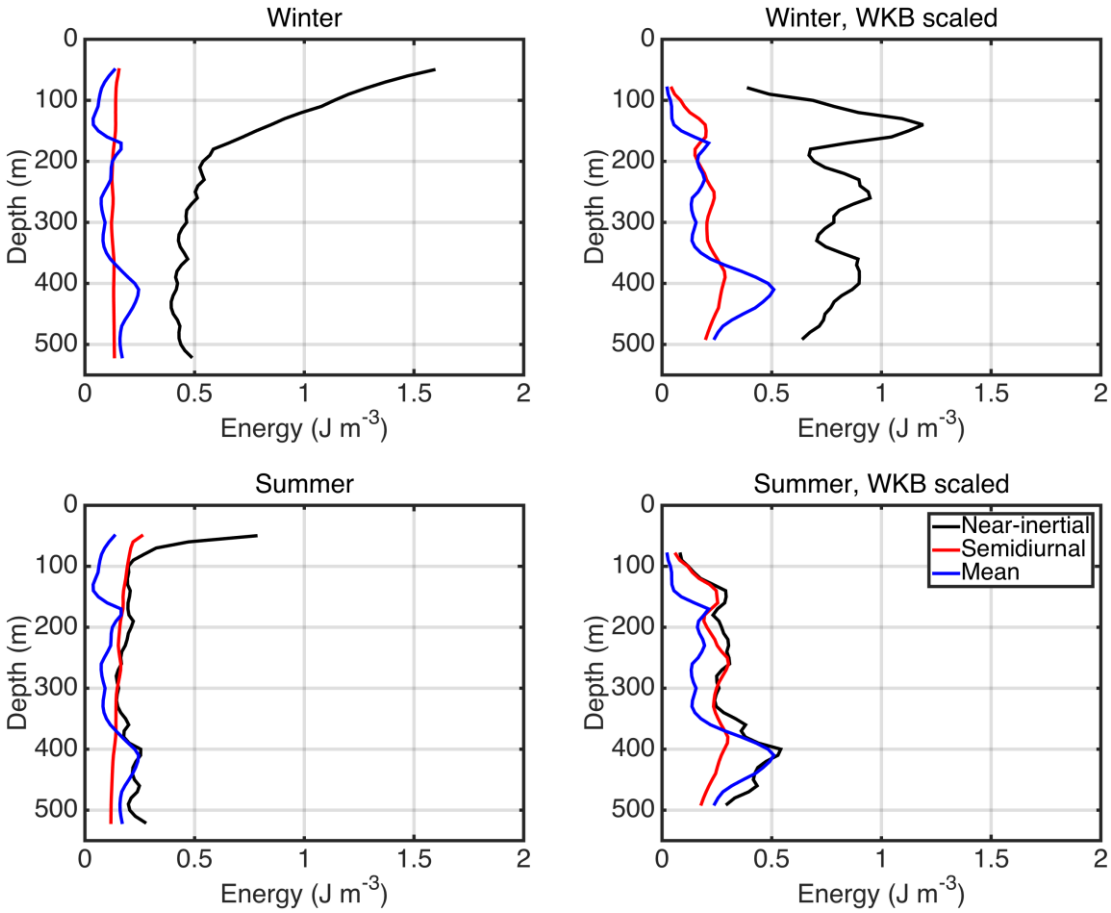


Figure 5.13: KE profiles for (top) winter and summer (bottom), (left) observed and (right) WKB-scaled.

### 5.6 Summary and discussion

This Chapter describes year-long observations of downward-propagating wind-generated NIWs in the upper 50-520 m of the water column, and demonstrates the variability in the character with season. Near-inertial KE is surface-intensified and dominated by downward-propagating component at large vertical scales (> 100 m), supporting the hypothesis that NIWs are mainly surface wind generated at the study region. I also present observational evidence that NIWs undergo a seasonal cycle at the PAP site in the upper ocean: they are much stronger in winter than in summer. Wintertime shows marked downward radiation extending at least to the bottom of our record at 520 m. An important consequence is that enhanced NIWs activity in the winter mixed layer is expected to transfer more energy downward. While the present results are relatively modest in scope, the NIWs at the study region illustrate a possible energy pathway that could be important for diapycnal mixing in the deep ocean. These findings

add observational evidence of downward-propagating NIWs in the Northeast Atlantic, and may lead to better understanding of the energetics of the ocean circulation.

Further investigation is therefore required to calculate the percentage of the energy put into mixed-layer near-inertial motions by the wind that transits 520 m and therefore potentially reaches the ocean interior. The estimate of the downward flux of energy flux carried by the NIWs can be done in a variety of methods. For example, following Alford et al. (2012), vertical energy flux can be computed directly from the mean downgoing WKB-scaled near-inertial KE below the mixed layer multiplying the mean group velocity. In doing so, only downward propagating rather than total energy should be used because upward-propagating waves could be generated from somewhere else and hence should not be compared with the local wind work.

The wind-generated NIWs at the PAP site seem to have a similar seasonality with submesoscale fronts (Buckingham et al. 2016; Thompson et al. 2016). The strong vertical vorticity and horizontal buoyancy gradients conspire to significantly modify the evolution of the NIWs based on previous numerical studies (Whitt and Thomas 2015; Thomas 2017). NIW-mean flow interactions associated with vertical vorticity may also trigger wave-wave interactions that transfer KE from the inertial peak to higher frequencies (Wagner and Young 2016). Furthermore, fine-scale shear is thought to play a key role in the dissipation of the internal wave field, leading to production of small-scale mixing in the ocean. As a quick comparison vertical shear measured by the ADCP and the dissipation rate estimated from the OSMOSIS gliders is shown in Figure 5.14. Both estimates are the average from 300-500 m. However, the relationship is imperfect, reflecting the complexity of small-scale turbulence below the mixed layer. The evidence for the transfer of energy from low-frequency inertial waves to high-frequency wave should be investigated in future. To do so, requires simulation of the three-dimensional near-inertial wave ray paths though a flow field resembling the observed background conditions.

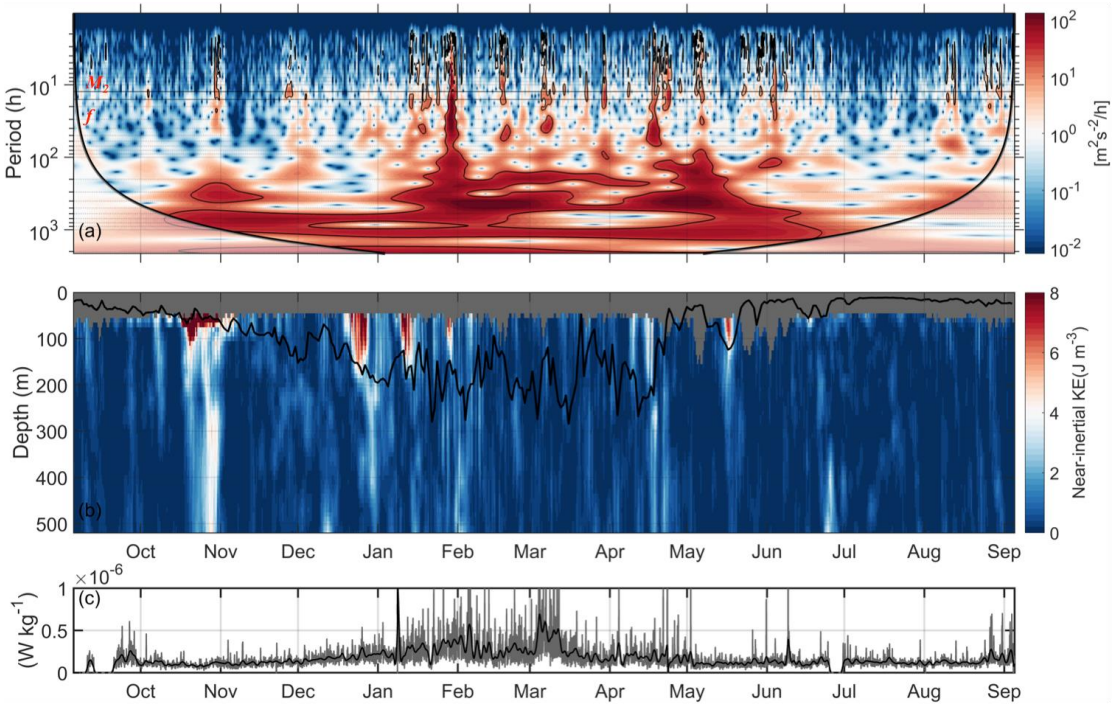


Figure 5.14: (a) A continuous wavelet analysis of the vertical shear measured at 300 – 500 m. The black contours marks the 5% significance level. The light shaded area shows the edges that may be affected by the cone of influence. (b) Near-inertial KE estimated from the ACMs and (c) raw (grey) and daily (black) values of dissipation rates estimated from the OSMOSIS gliders. Black lines in (b) indicate the MLD. Missing values in (b) are colored in grey.

# Chapter 6: Conclusions and future work

This chapter summarizes the main findings of this PhD research, the outstanding questions, and the recommendations for future work.

## 6.1 Overview of key findings

Submesoscale flows (1-10 km) have been recognized as playing a key role in the evolution of the OSBL over the last few decades (Thomas et al. 2008; Klein and Lapeyre 2009; McWilliams 2016). The year-long OSMOSIS mooring observations of temperature, salinity, pressure and horizontal velocity from the Northeast Atlantic provide a unique dataset to explore an annual cycle of the submesoscale dynamics in the open ocean. As argued throughout this thesis, submesoscale dynamics play a key role in determining the evolution of the OSBL in the study region, both for deepening and shoaling periods.

In the first part of this thesis, mooring observations are analyzed to study the impact of mesoscale and submesoscale flows on the buoyancy budget of the local thermocline down to 500 m. Vertical velocities inferred using the non-diffusive density equation are substantially stronger at submesoscales than at mesoscales. Observations suggest that elevated submesoscale vertical velocities and rates of restratification are associated with mesoscale frontogenesis, which drives enhanced submesoscale lateral buoyancy gradients and induces ageostrophic secondary circulations. Vertical velocity also increases when mesoscale eddies pass through the domain and drives a positive buoyancy flux. The presence of mesoscale features is likely to play a role in energizing submesoscale flows with pronounced vertical velocity signatures. This result is of importance considering mesoscale frontogenesis as a regular precursor of the submesoscale turbulence that restratifies the upper ocean.

In the latter part of this thesis, I employed a theoretical framework of the flux form of the PV equation for quantifying the competing processes in deepening and shoaling of the OSBL. The respective contributions of diabatic and frictional processes to the PV budget in the OSBL differ on temporal scales. Persistent atmospheric cooling in the wintertime is the dominant process in deepening the OSBL and reducing the PV, by triggering GI. In contrast, on shorter time scales (i.e., a few days), frictional processes have a comparable impact on the OSBL as the diabatic processes. In particular, downfront winds often precondition the water column unstable to SI, which can restratify the OSBL rapidly (on the order of a day) and limit the reduction of PV. These results in Chapter 4 highlight the importance of representing submesoscale overturning instabilities within climate-scale ocean models.

In the final part of this thesis, the downward propagation of wind-generated NIWs is examined at the mooring site. Measurements from ACMs and ADCP on the central

mooring give consistent characteristics of NIWs. Near-inertial KE dominates the super-inertial band, and is seen radiating predominantly downward in a few strong resonant wind events throughout the year. It is possible that the substantial downward propagation of wind-generated NIWs transfer energy to higher-frequency (i.e., higher than the local frequency), high-shear internal waves where dissipation could occur. It has recently been suggested that the intense lateral density gradients modify the physics of NIWs and facilitate irreversible energy exchanges between NIWs, balanced motions and small-scale turbulence. In this scenario, NIWs can be susceptible to a parametric subharmonic instability (PSI) at fronts, mostly likely at the base of the mixed layer. If this is the case, the inertial shears at the base of the mixed layer should be strongest and much of the dissipation of near-inertial motions is thought to occur (Plueddemann and Farrar 2006). An extension of the analysis presented in this thesis is required in order to understand NIWs evolve and interact with submesoscale fronts. The OSMOSIS mooring observations are sufficient to support this future study.

## 6.2 Towards a comprehensive representation of submesoscale dynamics in ocean models

A comprehensive climate model would require the best possible representation of the underlying physics. However, the current climate-scale ocean models only reproduce a subset of the relevant ocean dynamics because of their coarse grid resolution, and also they are subject to large and unquantified parameterization uncertainties at the subgrid scale (Murphy et al. 2004).

*Mixed-layer BCI*: To date, mixed-layer BCI has thus far received the most attention and is relatively better understood compared with other submesoscale instabilities such as SI. The mixed-layer BCI releases the APE and moves the lighter water of the front up and over the heavier water to tilt isopycnals toward the horizontal, restratifying the ML. The relaxation of isopycnal back towards the horizontal associated with mixed-layer BCI has a time scale of a few days, slower than the equilibration to marginal stability that happens during SI which is O (1 day), but faster than mesoscale variations. A growing amount of evidence suggests that even in the summer when mixed layer is shallow, the mixed-layer BCI damps out by restratifying the mixed layer so that submesoscale flows remain weak. However, it is worth noting that the mixed-layer deformation radius scales with MLD, so the instability scale is smaller when the mixed layer is shallow in summer, which can be as small as 10-100 m. Therefore, it is likely

that a fixed modeling or observational resolution do not resolve the mixed-layer BCI scale in summer.

Mixed-layer BCI has been shown to be a dominant energization mechanism for submesoscale flows in strong frontal regions such as the western North Atlantic (Callies et al. 2015). Fox-Kemper et al. (2008) derive a parameterization for the restratification process by mixed-layer BCI (so-called mixed layer instabilities in their paper) in terms of an overturning streamfunction involving the MLD and the amplitude of lateral buoyancy gradients. The existing parameterization neglects the influence of mesoscale frontogenesis. This is a serious limitation of the parameterization.

At the OSMOSIS mooring site, a more quiescent region of the ocean, mixed-layer BCI is most likely to contribute to mixed-layer restratification from existing parameterizations and estimates of the MLD. Applying the parameterization for the restratification process by mixed-layer BCI to a regional study is difficult because the empirical parameters based on numerical simulations might fall in a specific area. The OSMOSIS measurements provide lateral buoyancy gradients at different horizontal resolutions and MLD in different criterion, and could be used in sensitivity studies.

Furthermore, the submesoscale impact on mesoscale KE is still not considered in parameterizations. Recent numerical and satellite studies (e.g. Qiu et al. 2014; Sasaki et al. 2017) suggest submesoscale inverse KE cascade might be the main mechanism for mesoscale seasonality in high KE regions, such as the Kuroshio Extension and the western and eastern subtropics. In other regions like subarctic regions, the KE seasonality is mainly produced by larger-scale instabilities with scales of 100 km and not so much by mixed-layer BCI. These effects vary from area to area is a particularly difficult features to capture as a parameterization in a global-scale ocean model.

*SI*: Numerical simulations with an O (1 km) grid that resolve submesoscale fronts and wintertime mixed-layer eddies typically do not resolve SI. Without high enough resolution (e.g., 200 m horizontal resolution), the geostrophic shear might be just diffused by grid-scale numerical dissipation before becoming unstable.

Bachman et al. (2017) proposed a parameterization for the effects of SI on a resolved front. The parameterization is designed to be sensitive to surface forcing by buoyancy loss and/or downfront winds, and the OSBL is considered as a two-layer system (i.e., convective layer and forced SI layer) with distinct dynamics. While these parameterizations have been successfully tested against a set of idealized numerical simulations, *in situ* validations have been difficult to achieve. Results in Chapter 4

suggest that destabilizing surface forcing is a necessary, but not sufficient condition for SI.

Furthermore, how the parameterization should behave when the total surface forcing is destabilizing but one of the components is stabilizing is not clear yet. It is also not clear yet about how SI changes over seasons.

### 6.3 Towards a global view of submesoscale flows

Recent simulations and observations are revolutionizing our picture of the submesoscale dynamics and effects, and reveal that three-dimensional frontal processes fundamentally change the physics of the OSBL. However, capturing submesoscale variability on a global scale remains a critical challenge that requires the development of new approaches to observation. It is anticipated to emerge from the upcoming Surface Water and Ocean Topography (SWOT) mission. The SWOT is expected to measure the global sea surface height (SSH) field with a spatial resolution of O (10) km, which is much higher than the nadir-looking altimeters currently employed.

A major challenge will be to distinguish between SSH anomalies associated with balanced flows and those induced by inertia-gravity waves. Care must be taken when applying the geostrophic balance to infer surface currents in the submesoscale range, and the repeat cycle will be too long to identify inertia-gravity waves based on their high frequencies. Qiu et al. (2017) show that the transition length scale separating balanced geostrophic flows and unbalanced internal waves strongly depend on the energy level of local mesoscale eddy variability, varying from 15 km in the Kuroshio region to 200 km near North Equatorial Current. The OSMOSIS mooring observations could provide a regional study to test how much SSH variance at the submesoscale and the associated scale dependence of the SSH variance. Progress may be possible by estimating the dynamic height anomalies between the OSMOSIS moorings, and comparing with the SSH anomalies captured from current satellites.

### 6.4 Future work

Several possible future steps will be discussed in this section. The first focuses on the vertical velocity estimation under the framework of the QG dynamics (Chapter 3). The ageostrophic circulation develops in response to the increasing lateral buoyancy gradient driven by frontogenesis and is well captured by the QG-omega equation. The QG-omega equation eliminates the time derivative between the buoyancy equation and the PV equation, representing steady approximations to the vertical velocity. This

would aid in eliminating the effects by wave-like structures in the calculation of vertical velocity.

Another potential for future work is the further investigation of the signature of SI based on the mooring data (Chapter 4). From the PV perspective, conditions favourable for SI are set up by surface cooling and/or downfront winds. This feature was well captured by the OSMOSIS moorings. The first stage of the further investigation would be to calculate the anomaly of the central mooring properties from an inner-mooring average. Overturning circulations or filaments below the convective layer but above the base of thermocline would be strong signatures that are underpinned by SI dynamics. Furthermore, observations also show that SI often occurred throughout the mixed layer just after persistent surface cooling. Further progress can be made by having a closer look at these events, and possibly an idealized ocean model could be used to show GI preconditioning the ocean susceptible to SI is a dynamically robust feature in the upper ocean. Lastly, the challenges in interpreting PV budget from the OSMOSIS mooring data are significant. In this dataset, I am unable to include the PV evolution in the top 50 m depth, where PV destruction is highly likely to occur due to convective mixing triggered by buoyancy loss to the atmosphere during winter. It might be the reason that the PV budget is not well closed. Future field campaigns will therefore need to be designed in order to address whether winds or air-sea fluxes primarily drive upper ocean PV evolution. Despite these limitations, the present results support existing theoretical (Thomas and Lee 2005; Taylor and Ferrari 2010) and modeling (Thomas and Taylor 2010) efforts suggesting steady winds at ocean fronts play an important role and underscore the need for accurate representation of submesoscale instabilities within climate-scale ocean models. Further, numerical outputs from a submesoscale -resolving model could be used to test and retain methodologies (e.g., vertical advection of PV) used in Chapter 4.

Finally, the slab model (Chapter 5) replaces important physics with simple parameterizations, and cannot simulate or accommodate the sudden changes in the MLD during strong forcing. Alternatively, the PWP model (Price-Weller-Pinkel) includes physically-based vertical mixing of momentum and buoyancy but continues to neglect the lateral gradients responsible for wave radiation. PWP lacks the numerical simplicity and possibility of analytic solution and longer PWP simulations require high-frequency heat and freshwater fluxes. Comparison between the two models here is a vital step for evaluating the importance of MLD evolution during a forcing event.

Furthermore, the evolution of MLD from the PWP model can be used to separate the stratification driven by air-sea heat and momentum fluxes from the glider/mooring observed ocean stratification. In doing so, to separate the effects of one-dimensional vertical processes from other three-dimensional processes captured in the observations.

# Appendix: Dataset of ACM/CTD

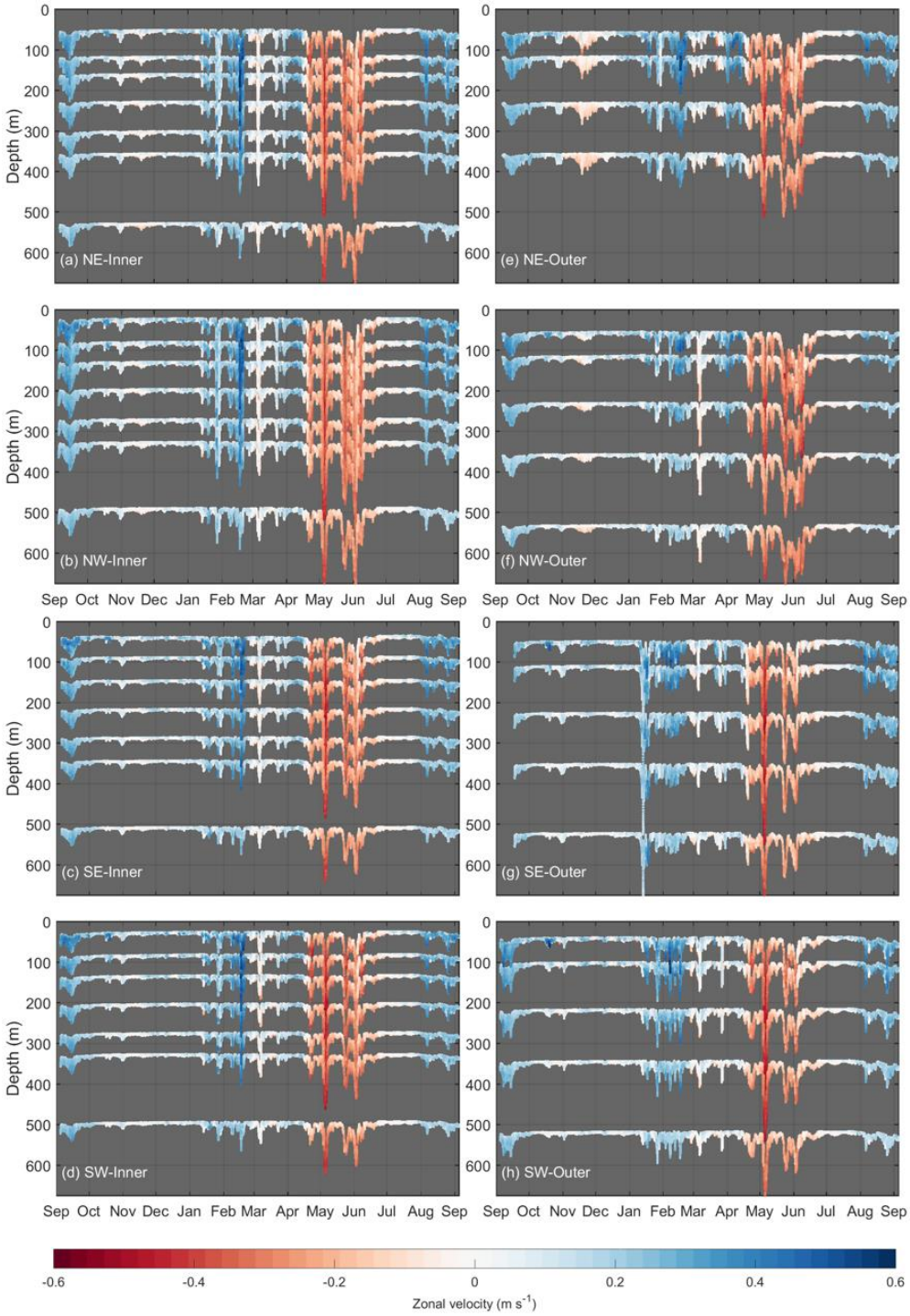


Figure A1: Observation of zonal velocity (m $s^{-1}$) as a function of time (months) and depth (m) on sensors on the (a) NE-Inner mooring, (b) NW-Inner mooring, (c) SE-Inner mooring, (d) SW-Inner mooring, (e) NE-Outer mooring, (f) NW-Outer mooring, (g) SE-Outer mooring and (h) SW-Outer mooring.

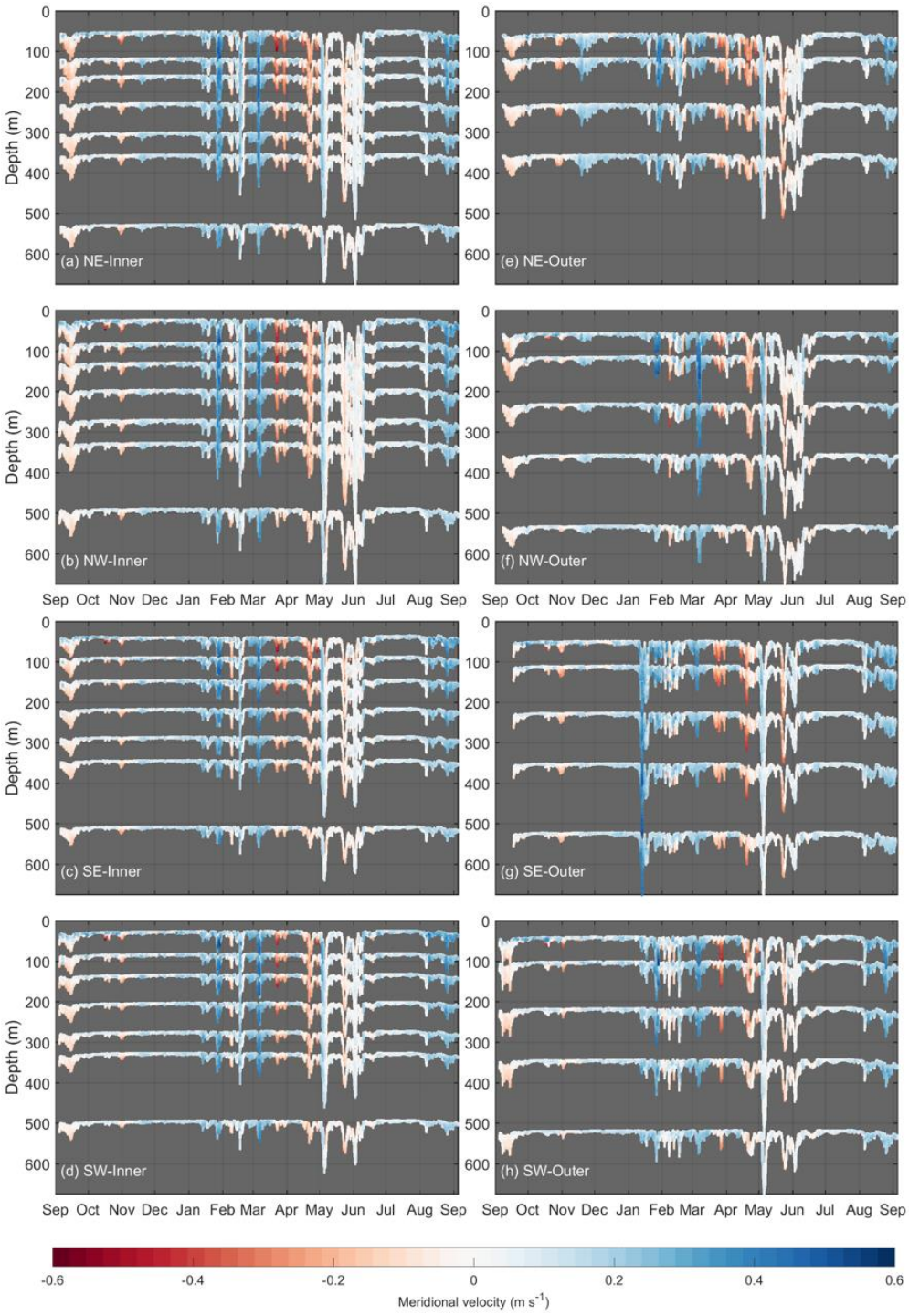


Figure A2: Observation of meridional velocity (m $s^{-1}$) as a function of time (months) and depth (m) on sensors on the (a) NE-Inner mooring, (b) NW-Inner mooring, (c) SE-Inner mooring, (d) SW-Inner mooring, (e) NE-Outer mooring, (f) NW-Outer mooring, (g) SE-Outer mooring and (h) SW-Outer mooring.

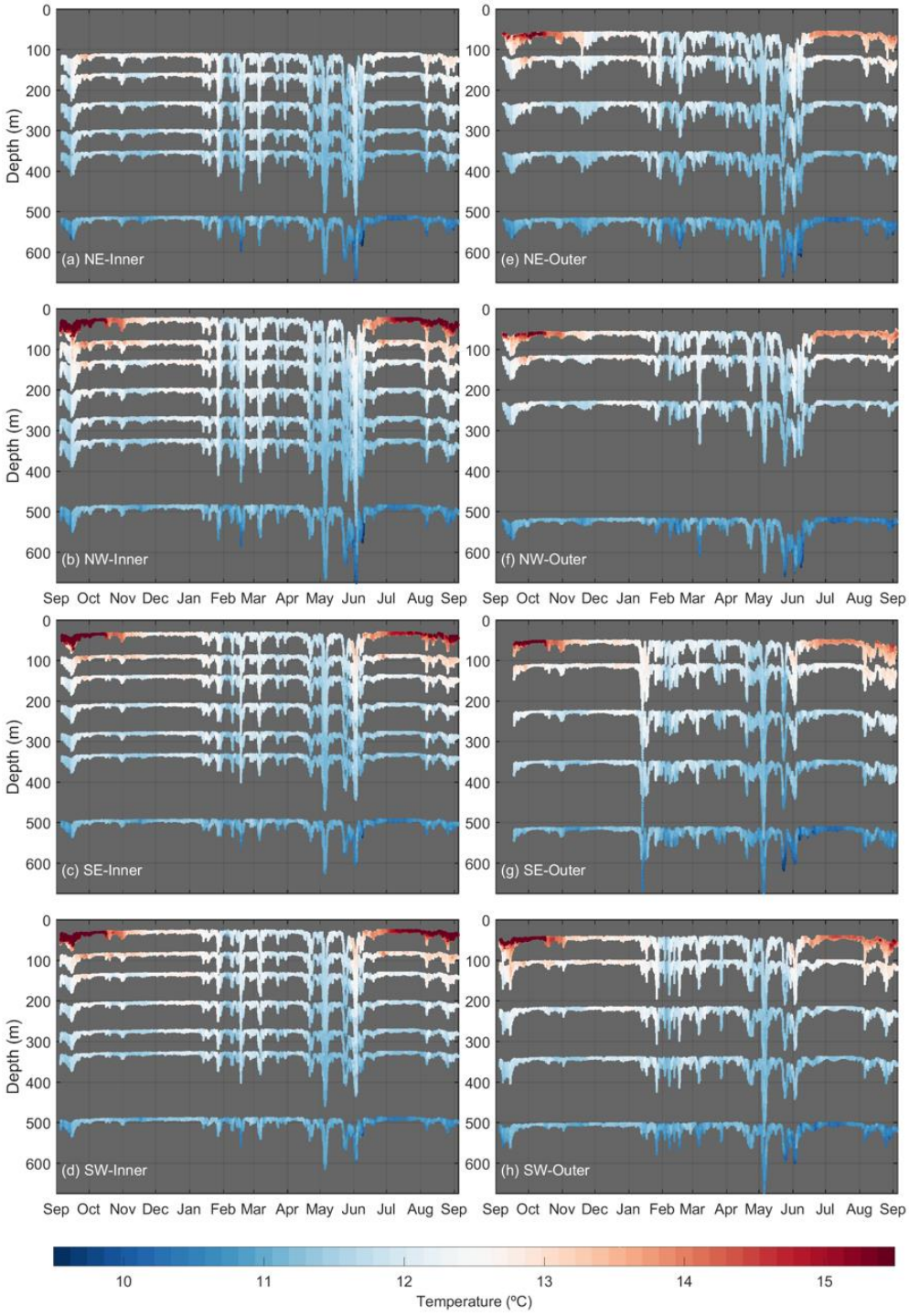


Figure A3: Observation of temperature (°C) as a function of time (months) and depth (m) on sensors on the (a) NE-Inner mooring, (b) NW-Inner mooring, (c) SE-Inner mooring, (d) SW-Inner mooring, (e) NE-Outer mooring, (f) NW-Outer mooring, (g) SE-Outer mooring and (h) SW-Outer mooring.

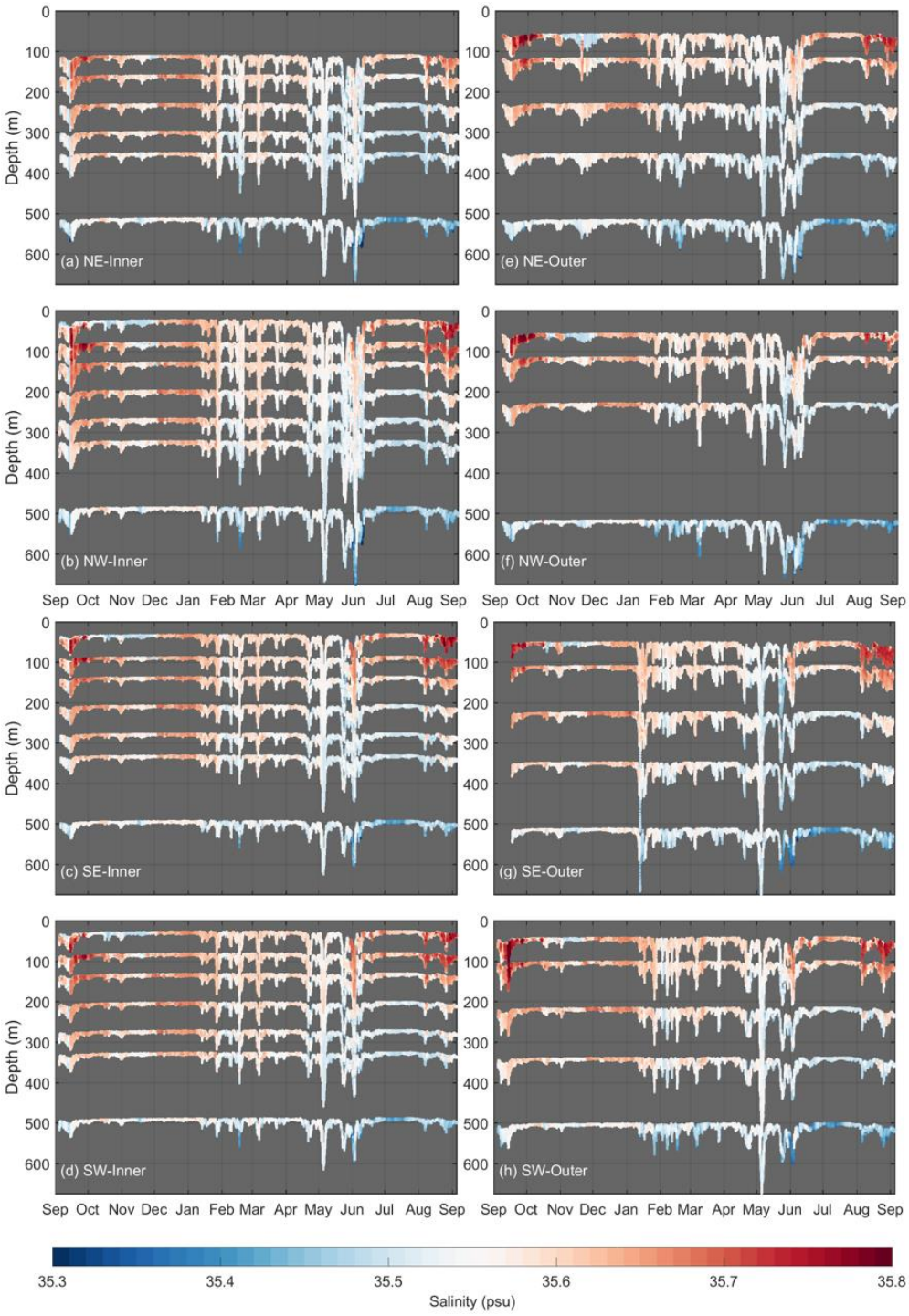


Figure A4: Observation of salinity (psu) as a function of time (months) and depth (m) on sensors on the (a) NE-Inner mooring, (b) NW-Inner mooring, (c) SE-Inner mooring, (d) SW-Inner mooring, (e) NE-Outer mooring, (f) NW-Outer mooring, (g) SE-Outer mooring and (h) SW-Outer mooring.

# References

Adams, K. A., P. Hosegood, J. R. Taylor, J. B. Sallee, S. Bachman, R. Torres, and M. Stamper, 2017: Frontal Circulation and Submesoscale Variability during the Formation of a Southern Ocean Mesoscale Eddy. *J. Phys. Oceanogr.*, **47**, 1737-1753.

Alford, M. H., 2001: Internal swell generation: The spatial distribution of energy flux from the wind to mixed layer near-inertial motions. *J. Phys. Oceanogr.*, **31**, 2359–2368.

Alford, M. H., 2003a: Redistribution of energy available for ocean mixing by long-range propagation of internal waves. *Nature*, **423**, 159-162.

Alford, M. H., 2003b: Improved global maps and 54-year history of wind-work on ocean inertial motions. *Geophys. Res. Lett.*, **30**, 1424-1427.

Alford, M. H., and M. Whitmont, 2007: Seasonal and spatial variability of near-inertial kinetic energy from historical moored velocity records. *J. Phys. Oceanogr.*, **37**, 2022-2037.

Alford, M. H., M. F. Cronin, and J. M. Klymak, 2012: Annual Cycle and Depth Penetration of Wind-Generated Near-Inertial Internal Waves at Ocean Station Papa in the Northeast Pacific. *J. Phys. Oceanogr.*, **42**, 889-909.

Alford, M. H., A. Y. Shcherbina, and M. C. Gregg, 2013: Observations of Near-Inertial Internal Gravity Waves Radiating from a Frontal Jet. *J. Phys. Oceanogr.*, **43**, 1225-1239.

Alford, M. H., and Coauthors, 2015: The formation and fate of internal waves in the South China Sea. *Nature*, **521**, 65–69.

Alford, M. H., J. A. MacKinnon, H. L. Simmons, and J. D. Nash, 2016: Near-Inertial Internal Gravity Waves in the Ocean. *Annu. Rev. Mar. Sci.*, **8**, 95-123.

Allen, J. T., and Coauthors, 2013: Cruise Report: RSS Discovery Cruise 381. 14 Sep. – 03 Oct. 2012: Ocean surface Mixing, Ocean Sub-mesoscale Interaction Study (OSMOSIS), pp. 1-196, Natl. Oceanogr. Centre, Southampton, England.

Bachman, S. D., B. Fox-Kemper, J. R. Taylor, and L. N. Thomas, 2017: Parameterization of Frontal Symmetric Instabilities. I: Theory for Resolved Fronts. *Ocean Modell.*, **109**, 72-95.

Badin, G., A. Tandon, and A. Mahadevan, 2011: Lateral Mixing in the Pycnocline by Baroclinic Mixed Layer Eddies. *J. Phys. Oceanogr.*, **41**, 2080-2101.

Batchelor, G. K., 2000: An Introduction to Fluid Dynamics, 615 pp., Cambridge Univ. Press, Cambridge, U. K.

Beaird, N., I. Fer, P. Rhines, and C. Eriksen, 2012: Dissipation of turbulent kinetic energy inferred from Seagliders: An application to the eastern Nordic Seas overflows. *J. Phys. Oceanogr.*, **42**, 2268-2282.

Belcher, S. E., and Coauthors, 2012: A global perspective on Langmuir turbulence in the ocean surface boundary layer. *Geophys. Res. Lett.*, **39**, L18605.

Bennetts, D. A., and B. J. Hoskins, 1979: Conditional Symmetric Instability - Possible Explanation for Frontal Rainbands. *Quart. J. Roy. Meteor. Soc.*, **105**, 945-962.

Boccaletti, G., R. Ferrari, and B. Fox-Kemper, 2007: Mixed layer instabilities and restratification. *J. Phys. Oceanogr.*, **37**, 2228-2250.

Brannigan, L., D. P. Marshall, A. Naveira-Garabato, and A. J. George Nurser, 2015: The seasonal cycle of submesoscale flows. *Ocean Modell.*, **92**, 69-84.

Brannigan, L., 2016: Intense submesoscale upwelling in anticyclonic eddies. *Geophys. Res. Lett.*, **43**, 3360-3369.

Bryden, H. L., 1980: Geostrophic Vorticity Balance in Midocean. *J. Geophys. Res.*, **85**, 2825-2828.

Buckingham, C. E., and Coauthors, 2016: Seasonality of submesoscale flows in the ocean surface boundary layer. *Geophys. Res. Lett.*, **43**, 2118-2126.

Cairns, J. L., and G. O. Williams, 1976: Internal wave observations from a midwater float, 2. *J. Geophys. Res.*, **81**, 1943–1950.

Callies, J., R. Ferrari, J. M. Klymak, and J. Gula, 2015: Seasonality in submesoscale turbulence. *Nat. Commun.*, **6**, 6862.

Callies, J., G. Flierl, R. Ferrari, and B. Fox-Kemper, 2016: The role of mixed-layer instabilities in submesoscale turbulence. *J. Fluid Mech.*, **788**, 5-41.

Capet, X., J. C. Mcwilliams, M. J. Molemaker, and A. F. Shchepetkin, 2008a: Mesoscale to submesoscale transition in the California current system. Part I: Flow structure, eddy flux, and observational tests. *J. Phys. Oceanogr.*, **38**, 29-43.

Capet, X., J. C. Mcwilliams, M. J. Molemaker, and A. F. Shchepetkin, 2008b: Mesoscale to submesoscale transition in the California current system. Part II: Frontal processes. *J. Phys. Oceanogr.*, **38**, 44-64.

Capet, X., J. C. Mcwilliams, M. J. Molemaker, and A. F. Shchepetkin, 2008c: Mesoscale to submesoscale transition in the California current system. Part III: Energy balance and flux. *J. Phys. Oceanogr.*, **38**, 2256–2269.

Capet, X., G. Roullet, P. Klein, and G. Maze, 2016: Intensification of Upper-Ocean Submesoscale Turbulence through Charney Baroclinic Instability. *J. Phys. Oceanogr.*, **46**, 3365-3384.

Chaigneau, A., O. Pizarro, and W. Rojas, 2008: Global climatology of near-inertial current characteristics and Lagrangian observations. *Geophys. Res. Lett.*, **35**, L13603.

Charney, J. G., and M. E. Stern, 1962: On the stability of internal baroclinic jets in a rotating atmosphere. *J. Atmos. Sci.*, **19 (2)**, 159–172.

Charney, J. G., 1971: Geostrophic Turbulence. *J. Atmos. Sci.*, **28**, 1087-1095.

Chelton, D. B., R. A. de Szoeke, M. G. Schlax, K. E. Naggar, and N.Siwertz, 1998: Geographical variability of the first baroclinic Rossby radius of deformation. *J. Phys. Oceanogr.*, **28**, 433-460.

Chelton, D. B., P. Gaube, M. G. Schlax, J. J. Early, and R. M. Samelson, 2011: The Influence of Nonlinear Mesoscale Eddies on Near-Surface Oceanic Chlorophyll. *Science*, **334**, 328-332.

Czaja, A., and U. Hausmann, 2009: Observations of Entry and Exit of Potential Vorticity at the Sea Surface. *J. Phys. Oceanogr.*, **39**, 2280-2294.

Damerell, G. M., K. J. Heywood, A. F. Thompson, U. Binetti, and J. Kaiser (2016), The vertical structure of upper ocean variability at the Porcupine Abyssal Plain during 2012–2013. *J. Geophys. Res.*, **121**, 3075–3089.

D'Asaro, E. A., 1985: The energy flux from the wind to near-inertial motions in the surface mixed layer. *J. Phys. Oceanogr.*, **15**, 1043–1059.

D'Asaro, E. A., C. E. Eriksen, M. D. Levine, P. Niiler, C. A. Paulson, and P. V. Meurs, 1995: Upper-ocean inertial currents forced by a strong storm. Part I: Data and comparisons with linear theory. *J. Phys. Oceanogr.*, **25**, 2909–2936.

D'Asaro, E., C. Lee, L. Rainville, R. Harcourt, and L. Thomas, 2011: Enhanced turbulence and energy dissipation at ocean fronts. *Science*, **332**, 318–322.

Dee, D. P., and Coauthors, 2011: The ERA-Interim reanalysis: Configuration and performance of the data assimilation system. *Quart. J. Roy. Meteor. Soc.*, **137**, 553–597.

du Plessis, M., S. Swart, I. J. Ansorge, and A. Mahadevan, 2017: Submesoscale processes promote seasonal restratification in the Subantarctic Ocean. *J. Geophys. Res.*, **122**, 2960-2975.

Ferrari, R., and C. Wunsch, 2009: Ocean circulation kinetic energy: Reservoirs, sources, and sinks. *Annu. Rev. Fluid Mech.*, **41**, 253–282.

Ferrari, R., 2011: A frontal challenge for climate models. *Science*, **332**, 316–317.

Fischer, A. S., R. A. Weller, D. L. Rudnick, C. C. Eriksen, C. M. Lee, K. H. Brink, C. A. Fox, and R. R.Leben, 2002: Mesoscale eddies, coastal upwelling, and the upper ocean heat budget in the Arabian Sea. *Deep-Sea Res.*, **49B**, 2231–2264.

Fomin, L. M., 1973: Inertial oscillations in a horizontally inhomogeneous current velocity field. Izv., *Atmos. Oceanic Phys.*, **9**, 37–40.

Fox-Kemper, B., R. Ferrari, and R. Hallberg, 2008: Parameterization of mixed layer eddies. Part I: Theory and diagnosis. *J. Phys. Oceanogr.*, **38**, 1145-1165.

Frajka-Williams, E., C. C. Eriksen, P. B. Rhines, and R. R. Harcourt, 2011: Determining Vertical Water Velocities from Seaglider. *J. Atmos. Oceanic Technol.*, **28**, 1641-1656.

Fu, L.-L., 1981: Observations and models of inertial waves in the deep ocean. *Rev. Geophys. Space Phys.*, **19**, 141–170.

Garrett, C., and W. Munk, 1975: Space-time scales of internal waves: A progress report. *J. Geophys. Res.*, **80**, 291–297.

Garrett, C., 2001: What is the "near-inertial" band and why is it different from the rest of the internal wave spectrum? *J. Phys. Oceanogr.*, **31**, 962–971.

Gaube, P., D. B. Chelton, R. M. Samelson, M. G. Schlax, and L. W. O'Neill, 2015: Satellite Observations of Mesoscale Eddy-Induced Ekman Pumping. *J. Phys. Oceanogr.*, **45**, 104-132.

Gerbi, G. P., J. H. Trowbridge, E. A. Terray, A. J. Plueddemann, and T. Kukulka, 2009: Observations of turbulence in the ocean surface boundary layer: Energetics and transport. *J. Phys. Oceanogr.*, **39**, 1077–1096.

Gill, A. E., J. S. A. Green, and A. J. Simmons, 1974: Energy partition in the large-scale ocean circulation and the production of mid-ocean eddies. *Deep-Sea Res. Oceanogr. Abstr.*, **21**, 499–528.

Gill, A. E., 1982: Atmosphere–Ocean Dynamics. Academic Press, 662 pp.

Gill, A. E., 1984: On the behavior of internal waves in the wake of a storm. *J. Phys. Oceanogr.*, **14**, 1129–1151.

Gonella, J., 1972: A rotary-component method for analysing meteorological and oceanographic vector time series. *Deep-Sea Res.*, **19**, 833–846.

Gula, J., M. J. Molemaker, and J. C. McWilliams, 2014: Submesoscale Cold Filaments in the Gulf Stream. *J. Phys. Oceanogr.*, **44**, 2617-2643.

Gula, J., M. J. Molemaker, and J. C. McWilliams, 2015: Topographic vorticity generation, submesoscale instability and vortex street formation in the Gulf Stream. *Geophys. Res. Lett.*, **42**, 4054–4062.

Gula, J., M. J. Molemaker, and J. C. McWilliams, 2016: Topographic generation of submesoscale centrifugal instability and energy dissipation. *Nat. Commun.*, **7**, 12811.

Haine, T. W. N., and J. Marshall, 1998: Gravitational, symmetric, and baroclinic instability of the ocean mixed layer. *J. Phys. Oceanogr.*, **28**, 634-658.

Hamlington, P. E., L. P. Van Roekel, B. Fox-Kemper, K. Julien, and G. P. Chini, 2014: Langmuir-submesoscale interactions: Descriptive analysis of multiscale frontal spindown simulations, *J. Phys. Oceanogr.*, **44**, 2249–2272.

Haney, S., B. Fox-Kemper, K. Julien, and A. Webb, 2015: Symmetric and geostrophic instabilities in the wave-forced ocean mixed layer, *J. Phys. Oceanogr.*, **45**, 3033–3056.

Haynes, P. and M. McIntyre. 1987. On the evolution of vorticity and potential vorticity in the presence of diabatic heating and frictional or other forces. *J. Atmos. Sci.*, **44**, 828–841.

Holton, J. R., 2004: An Introduction to Dynamical Meteorology. 4th ed. Academic Press, 535 pp.

Hosegood, P. J., M. C. Gregg, and M. H. Alford, 2013: Wind-driven submesoscale subduction at the North Pacific Subtropical Front. *J. Geophys. Res.*, **118**, 5333–5352.

Hoskins, B. J., and F. P. Bretherton, 1972: Atmospheric Frontogenesis Models - Mathematical Formulation and Solution. *J. Atmos. Sci.*, **29**, 11-37.

Hoskins, B. J., 1974, The role of potential vorticity in symmetric stability and instability, *Quart. J. Roy. Meteor. Soc.*, **100**, 480–482.

Hoskins, B. J., I. Draghici, and H. C. Davies, 1978: A new look at the $\omega$-equation. *Quart. J. Roy. Meteor. Soc.*, **104**, 31-38.

Hoskins, B. J., 1982: The Mathematical-Theory of Frontogenesis. *Annu. Rev. Fluid Mech.*, **14**, 131-151.

Hoskins, B. J., M. E. Mcintyre, and A. W. Robertson, 1985: On the Use and Significance of Isentropic Potential Vorticity Maps. *Quart. J. Roy. Meteor. Soc.*, **111**, 877-946.

Huppert, H. E., 1975: Some remarks on the initiation of Taylor columns. *J. Fluid Mech.*, **67**, 397–412.

Jiang, J., Y. Lu, and W. Perrie, 2005: Estimating the energy flux from the wind to ocean inertial motions: The sensitivity to surface wind fields. *Geophys. Res. Lett.*, **32**, L15610.

Jochum, M., B. P. Briegleb, G. Danabasoglu, W. G. Large, N. J. Norton, S. R. Jayne, and F. O. Bryan, 2013: The impact of oceanic near-inertial waves on climate. *J. Climate*, **26**, 2833–2844.

Joyce, T. M., L. N. Thomas, and F. Bahr, 2009: Wintertime observations of Subtropical Mode Water formation within the Gulf Stream. *Geophys. Res. Lett.*, **36**, L02607.

Kilbourne, B. F., and J. B. Girton, 2015: Quantifying High-Frequency Wind Energy Flux into Near-Inertial Motions in the Southeast Pacific. *J. Phys. Oceanogr.*, **45**, 369-386.

Klein, P., B. L. Hua, G. Lapeyre, X. Capet, S. Le Gentil, and H. Sasaki, 2008: Upper ocean turbulence from high-resolution 3D simulations. *J. Phys. Oceanogr.*, **38**, 1748-1763.

Klein, P., and G. Lapeyre, 2009: The Oceanic Vertical Pump Induced by Mesoscale and Submesoscale Turbulence. *Annu. Rev. Mar. Sci.*, **1**, 351-375.

Klein, P., G. Lapeyre, G. Roullet, S. Le Gentil, and H. Sasaki, 2011: Ocean turbulence at meso and submesoscales: connection between surface and interior dynamics. *Geophys. Astro. Fluid*, **105**, 421-437.

Kunze, E., 1985: Near-inertial wave propagation in geostrophic shear. *J. Phys. Oceanogr.*, **15**, 544–565.

Lapeyre, G., P. Klein, and B. L. Hua, 2006: Oceanic restratification forced by surface frontogenesis. *J. Phys. Oceanogr.*, **36**, 1577-1590.

Large, W. G., and S. Pond, 1981: Open ocean momentum flux measurements in moderate to strong winds. *J. Phys. Oceanogr.*, **11**, 324–336.

Large, W. G., J. C. McWilliams, and S. C. Doney, 1994: Oceanic Vertical Mixing - A Review and a Model with a Nonlocal Boundary-Layer Parameterization. *Rev. Geophys.*, **32**, 363–403.

Large, W. G., G. Danabasoglu, S. C. Doney, and J. C. McWilliams, 1997: Sensitivity to surface forcing and boundary layer mixing in a global ocean model: Annual-mean climatology. *J. Phys. Oceanogr.*, **27**, 2418-2447.

Leaman, K. D., and T. B. Sanford, 1975: Vertical energy propagation of inertial waves: A vector spectral analysis of velocity profiles. *J. Geophys. Res.*, **80**, 1975–1978.

Ledwell, J. R., A. J. Watson, and C. Law, 1993: Evidence for slow mixing across pycoline from open-ocean tracer experiment. *Nature*, **364**, 701–703.

Lévy, M., R. Ferrari, P. J. S. Franks, A. P. Martin, and P. Riviere, 2012: Bringing physics to life at the submesoscale. *Geophys. Res. Lett.*, **39**, L14602.

Lévy, M., and A. P. Martin, 2013: The influence of mesoscale and submesoscale heterogeneity on ocean biogeochemical reactions. *Global Biogeochem. Cycles*, **27**, 1139-1150.

Lindstrom, S. S., and D. R. Watts, 1994: Vertical Motion in the Gulf-Stream near 68-Degrees-W. *J. Phys. Oceanogr.*, **24**, 2321-2333.

Mahadevan, A., 2006: Modeling vertical motion at ocean fronts: Are nonhydrostatic effects relevant at submesoscales? *Ocean Modell.*, **14**, 222–240.

Mahadevan, A., and A. Tandon, 2006: An analysis of mechanisms for submesoscale vertical motion at ocean fronts. *Ocean Modell.*, **14**, 241-256.

Mahadevan, A., L. N. Thomas, and A. Tandon, 2008: Comment on "eddy/wind interactions stimulate extraordinary mid-ocean plankton blooms". *Science*, **320**, 448.

Mahadevan, A., 2016: The Impact of Submesoscale Physics on Primary Productivity of Plankton. *Annu. Rev. Mar. Sci.*, **8**, 161-184.

Marshall, J. C., and A. J. G. Nurser, 1992: Fluid dynamics of oceanic thermocline ventilation. *J. Phys. Oceanogr.*, **22**, 583–595.

Martin, A. P., and K. J. Richards, 2001: Mechanisms for vertical nutrient transport within a North Atlantic mesoscale eddy. *Deep-Sea Res. II*, **48**, 757-773.

Maze, G., and J. Marshall, 2011: Diagnosing the Observed Seasonal Cycle of Atlantic Subtropical Mode Water Using Potential Vorticity and Its Attendant Theorems. *J. Phys. Oceanogr.*, **41**, 1986-1999.

Maze, G., J. Deshayes, J. Marshall, A. M. Treguier, A. Chronis, and L. Vollmer, 2013: Surface vertical PV fluxes and subtropical mode water formation in an eddy-resolving numerical simulation. *Deep-Sea Res. II*, **91**, 128-138.

Mazzini, P. L. F., and J. A. Barth, 2013: A comparison of mechanisms generating vertical transport in the Brazilian coastal upwelling regions. *J. Geophys. Res.*, **118**, 5977-5993.

McDougall, T. J. and P. M. Barker, 2011: Getting started with TEOS-10 and the Gibbs Seawater (GSW) Oceanographic Toolbox, 28pp., SCOR/IAPSO WG127, ISBN 978-0-646-55621-5.

Mcdowell, S., P. Rhines, and T. Keffer, 1982: North-Atlantic Potential Vorticity and Its Relation to the General-Circulation. *J. Phys. Oceanogr.*, **12**, 1417-1436.

McGillicuddy, D. J., and Coauthors, 2007: Eddy/wind interactions stimulate extraordinary mid-ocean plankton blooms. *Science*, **316**, 1021-1026.

Mcintyre, M. E., 2015a: Balanced flow. *Encyclopedia of Atmospheric Sciences*, **2**, 298-303.

Mcintyre, M. E., 2015b: Potential Vorticity. *Encyclopedia of Atmospheric Sciences*, 2, 375-383.

McWilliams J. C., 1985: Submesoscale, coherent vortices in the ocean. Rev. Geophys., **23**, 165–182.

McWilliams, J. C., 2008: Fluid dynamics at the margin of rotational control. *Environ. Fluid Mech.*, **8**, 441–449.

McWilliams, J. C., F. Colas, and M. J. Molemaker, 2009: Cold filamentary intensification and oceanic surface convergence lines. *Geophys. Res. Lett.*, **36**, L18602.

McWilliams, J. C., J. Gula, M. J. Molemaker, L. Renault, and A. F. Shchepetkin, 2015: Filament frontogenesis by boundary layer turbulence. *J. Phys. Oceanogr.*, **45**, 1988–2005.

McWilliams, J. C., 2016: Submesoscale currents in the ocean, *Philos. Trans. R. Soc. London, Ser. A*, **472**, 20160117.

Meinen, C. S., 2008: Accuracy in mooring motion temperature corrections. *J. Atmos. Oceanic Technol.*, **25**, 2293-2303.

Mensa, J. A., Z. Garraffo, A. Griffa, T. M. Ozgokmen, A. Haza, and M. Veneziani, 2013: Seasonality of the submesoscale dynamics in the Gulf Stream region. *Ocean Dyn.*, **63**, 923-941.

Molemaker, M. J., J. C. McWilliams, and X. Capet, 2010: Balanced and unbalanced routes to dissipation in an equilibrated Eady flow. *J. Fluid Mech.*, **654**, 35-63.

Mooers, C. N. K., 1973: A technique for the cross-spectrum analysis of complex valued time series with emphasis on properties of polarized components and rotational invariants. *Deep-Sea Res.*, **20**, 1129–1141.

Mooers, C. N. K., 1975: Several effects of a baroclinic current on the cross-stream propagation of inertial-internal waves. *Geophys. Fluid Dyn.*, **6**, 245–275.

Murphy, J. M., D. M. H. Sexton, D. N. Barnett, G. S. Jones, M. J. Webb, and D. A. Stainforth, 2004: Quantification of modelling uncertainties in a large ensemble of climate change simulations. *Nature*, **430**, 768-772.

Naveira-Garabato, A. C., J. T. Allen, H. Leach, V. H. Strass, and R. T. Pollard, 2001: Mesoscale subduction at the Antarctic Polar Front driven by baroclinic instability. *J. Phys. Oceanogr.*, **31**, 2087-2107.

Naveira Garabato, A. C., and Coauthors, 2017: Vigorous lateral export of the meltwater outflow from beneath an Antarctic ice shelf. *Nature*, **542**, 219–222.

Olsina, O., N. Wienders, and W. K. Dewar, 2013: An estimate of the climatology and variability of Eighteen Degree Water potential vorticity forcing. *Deep-Sea Res. II*, **91**, 84-95.

Omand, M. M., E. A. D'Asaro, C. M. Lee, M. J. Perry, N. Briggs, I. Cetini, and A. Mahadevan, 2015: Eddy-driven subduction exports particulate organic carbon from the spring bloom. *Science*, **348**, 222-223.

Painter, S. C., R. E. Pidcock, and J. T. Allen, 2010: A mesoscale eddy driving spatial and temporal heterogeneity in the productivity of the euphotic zone of the northeast Atlantic. *Deep-Sea Res. II*, **57**, 1281-1292.

Park, J. J., K. Kim, and B. A. King, 2005: Global statistics of inertial motions. *Geophys. Res. Lett.*, **32**, L14612.

Pascual, A., S. Ruiz, B. Buongiorno Nardelli, S. Guinehut, D. Iudicone, and J. Tintoré, 2015: Net primary production in the Gulf Stream sustained by quasi-geostrophic vertical exchanges. *Geophys. Res. Lett.*, **42**, 441–449.

Pearson, B. C., A. L. M. Grant, J. A. Polton, and S. E. Belcher, 2015: Langmuir Turbulence and Surface Heating in the Ocean Surface Boundary Layer. *J. Phys. Oceanogr.*, **45**, 2897-2911.

Phillips, H. E., and S. R. Rintoul, 2000: Eddy variability and energetics from direct current measurements in the Antarctic Circumpolar Current south of Australia. *J. Phys. Oceanogr.*, **30**, 3050-3076.

Plueddemann, A. J., and J. T. Farrar, 2006: Observations and models of the energy flux from the wind to mixed layer inertial currents. *Deep-Sea Res.*, **53**, 5–30.

Pollard, R. T., 1970: Surface waves with rotation: An exact solution. *J. Geophys. Res.*, **75**, 5895–5898.

Pollard, R. T., and R. C. Millard, 1970: Comparison between observed and simulated wind-generated inertial oscillations. *Deep-Sea Res.*, **17**, 153–175.

Pollard, R. T., and L. A. Regier, 1992: Vorticity and Vertical Circulation at an Ocean Front. *J. Phys. Oceanogr.*, **22**, 609-625.

Polton, J. A., and D. P. Marshall, 2007: Overturning cells in the Southern Ocean and subtropical gyres. *Ocean Sci.*, **3**, 17-30.

Polzin, K. L., 2010: Mesoscale eddy–internal wave coupling. Part II: Energetics and results from PolyMode. *J. Phys. Oceanogr.*, **40**, 789–801.

Polzin, K. L., and Y. V. Lvov, 2011: Toward regional characterizations of the oceanic internal wavefield. *Rev. Geophys.*, **49**, RG4003.

Pope, V. D., M. L. Gallani, P. R. Rowntree, and R. A. Stratton, 1999: The impact of new physical parametrizations in the Hadley Centre climate model HadAM3. *Climate Dyn.*, **16**, 123-146.

Qiu, B., S. Chen, P. Klein, H. Sasaki, and Y. Sasai, 2014: Seasonal mesoscale and submesoscale eddy variability along the North Pacific Subtropical Countercurrent. *J. Phys. Oceanogr.*, **44**, 3079–3098.

Qiu, B., T. Nakano, S. M. Chen, and P. Klein, 2017: Submesoscale transition from geostrophic flows to internal waves in the northwestern Pacific upper ocean. *Nat. Commun.*, **8**, 14055.

Ramachandran, S., A. Tandon, and A. Mahadevan, 2014: Enhancement in vertical fluxes at a front by mesoscale-submesoscale coupling. *J. Geophys. Res.*, **119**, 8495-8511.

Riedel, K. S., and A. Sidorenko, 1995: Minimum bias multiple taper spectral estimation. *IEEE Trans. Signal Process.*, **43**, 188–195.

Rivas, D., A. Badan, J. Sheinbaum, J. Ochoa, J. Candela, 2008: Vertical velocity and vertical heat flux observed within loop current eddies in the central Gulf of Mexico, *J. Phys. Oceanogr.*, **38**, 2461-2481.

Rocha, C. B., S. T. Gille, T. K. Chereskin, and D. Menemenlis, 2016: Seasonality of submesoscale dynamics in the Kuroshio Extension. *Geophys. Res. Lett.*, **43**, 11304-11311.

Rossby, H. T., and T. B. Sanford, 1976: A study of velocity profiles through the thermocline. *J. Phys. Oceanogr.*, **6**, 766–774.

Rosso, I., A. M. Hogg, P. G. Strutton, A. E. Kiss, R. Matear, A. Klocker, and E. van Sebille, 2014: Vertical transport in the ocean due to sub-mesoscale structures: Impacts in the Kerguelen region. *Ocean Modell.*, **80**, 10-23.

Rosso, I., A. M. Hogg, A. E. Kiss, and B. Gayen, 2015: Topographic influence on submesoscale dynamics in the Southern Ocean. *Geophys. Res. Lett.*, **42**, 1139-1147.

Roullet, G., J. C. McWilliams, X. Capet, and M. J. Molemaker, 2012: Properties of steady geostrophic turbulence with isopycnal outcropping. *J. Phys. Oceanogr.*, **42**, 18–38.

Rudnick, D. L., 1996: Intensive surveys of the azores front .2. Inferring the geostrophic and vertical velocity fields. *J. Geophys. Res.*, **101**, 16291-16303.

Sallée, J. B., E. Shuckburgh, N. Bruneau, A. J. S. Meijers, T. J. Bracegirdle, and Z. Wang, 2013: Assessment of Southern Ocean mixed-layer depths in CMIP5 models: Historical bias and forcing response. *J. Geophys. Res.*, **118**, 1845-1862.

Sasaki, H., P. Klein, B. Qiu, and Y. Sasai, 2014: Impact of oceanic-scale interactions on the seasonal modulation of ocean dynamics by the atmosphere. *Nat. Commun.*, **5**, 5636.

Sasaki, H., Klein, P., Sasai, Y., Qiu, B, 2017: Regionality and seasonality of submesoscale and mesoscale turbulence in the North Pacific Ocean. *Ocean Dyn.*, **67**, 1195–1216.

Sévellec, F., A. C. Naveira Garabato, J. A. Brearley, and K. L. Sheen, 2015: Vertical Flow in the Southern Ocean Estimated from Individual Moorings. *J. Phys. Oceanogr.*, **45**, 2209-2220.

Shcherbina, A. Y., and Coauthors, 2015: The LatMix summer campaign: Submesoscale stirring in the upper ocean. *Bull. Amer. Meteor. Soc.*, **96**, 1257–1279.

Silverthorne, K. E., and J. M. Toole, 2009: Seasonal kinetic energy variability of near-inertial motions. *J. Phys. Oceanogr.*, **39**, 1035–1049.

Smith, K. M., P. E. Hamlington, and B. Fox-Kemper, 2016: Effects of submesoscale turbulence on ocean tracers. *J. Geophys. Res.*, **121**, 908-933.

Spall, M. A., 1995: Frontogenesis, Subduction, and Cross-Front Exchange at Upper Ocean Fronts. *J. Geophys. Res.*, **100**, 2543-2557.

Spall, M. A., R. A. Weller, and P. W. Furey, 2000: Modeling the three-dimensional upper ocean heat budget and subduction rate during the Subduction Experiment. *J. Geophys. Res.*, **105**, 26151-26166.

Stone, P. H., 1966: On Non-Geostrophic Baroclinic Stability. *J. Atmos. Sci.*, **23**, 390-400.

Stone, P. H., 1970: On Non-Geostrophic Baroclinic Stability: Part II. *J. Atmos. Sci.*, **27**, 721-726.

Sun, L., Q. A. Zheng, D. X. Wang, J. Y. Hu, C. K. Tai, and Z. Y. Sun, 2011: A case study of near-inertial oscillation in the South China Sea using mooring observations and satellite altimeter data. *J. Oceanogr.*, **67**, 677-687.

Sun, O. M., and R. Pinkel, 2012: Energy transfer from high-shear, low-frequency internal waves to high-frequency waves near Kaena Ridge, Hawaii. *J. Phys. Oceanogr.*, **42**, 1524–1547.

Taylor, J. R., and R. Ferrari, 2009: The role of secondary shear instabilities in the equilibration of symmetric instability. *J. Fluid. Mech.*, **622**, 103-113.

Taylor, J. R., and R. Ferrari, 2010: Buoyancy and Wind-Driven Convection at Mixed Layer Density Fronts. *J. Phys. Oceanogr.*, **40**, 1222-1242.

Taylor, J. R., and R. Ferrari, 2011: Ocean fronts trigger high latitude phytoplankton blooms. *Geophys. Res. Lett.*, **38**, L23601.

Thomas, L. N., and P. B. Rhines, 2002: Nonlinear stratified spin-up. *J. Fluid Mech.*, **473**, 211-244.

Thomas, L. N., 2005: Destruction of potential vorticity by winds. *J. Phys. Oceanogr.*, **35**, 2457-2466.

Thomas, L. N., and C. M. Lee, 2005: Intensification of ocean fronts by down-front winds. *J. Phys. Oceanogr.*, **35**, 1086-1102.

Thomas, L. N., 2008: Formation of intrathermocline eddies at ocean fronts by wind-driven destruction of potential vorticity. *Dyn. Atmos. Oceans.*, **45**, 252-273.

Thomas, L. N., and R. Ferrari, 2008: Friction, Frontogenesis, and the Stratification of the Surface Mixed Layer. *J. Phys. Oceanogr.*, **38**, 2501-2518.

Thomas, L. N., A. Tandon, and A. Mahadevan, 2008: Submesoscale Processes and Dynamics. *Eddy Resolving Ocean Modeling, M. W. Hecht and H. Hasumi, Eds., Amer. Geophys. Union*, 17-38.

Thomas, L. N., and T. M. Joyce, 2010: Subduction on the northern and southern flanks of the Gulf Stream. *J. Phys. Oceanogr.*, **40**, 429-438.

Thomas, and J. R. Taylor, 2010: Reduction of the usable wind-work on the general circulation by forced symmetric instability. *Geophys. Res. Lett.*, **37**, L18606.

Thomas, L. N., C. Lee, and Y. Yoshikawa, 2010: The subpolar Front of the Japan/East Sea. Part II: Inverse method for determining the frontal vertical circulation. *J. Phys. Oceanogr.*, **40**, 3–25.

Thomas, L. N., J. R. Taylor, R. Ferrari, and T. M. Joyce, 2013: Symmetric instability in the Gulf Stream. *Deep-Sea Res. II*, **91**, 96-110.

Thomas, L. N., J. R. Taylor, E. A. D'Asaro, C. M. Lee, J. M. Klymak, and A. Shcherbina, 2016: Symmetric instability, inertial oscillations, and turbulence at the Gulf Stream front, *J. Phys. Oceanogr.*, **46**, 197–217.

Thomas, L. N., 2017. On the modifications of near-inertial waves at fronts: Implications for energy transfer across scales, *Ocean Dyn.*, **67**, 1335-1350.

Thompson, A. F., A. Lazar, C. Buckingham, A. C. N. Garabato, G. M. Damerell, and K. J. Heywood, 2016: Open-Ocean Submesoscale Motions: A Full Seasonal Cycle of Mixed Layer Instabilities from Gliders. *J. Phys. Oceanogr.*, **46**, 1285-1307.

Wagner, G. L., and W. R. Young, 2016: A three-component model for the coupled evolution of near-inertial waves, quasi-geostrophic flow and the near-inertial second harmonic. *J. Fluid Mech.*, **802**, 806–837.

Wang, D. P., 1993: Model of Frontogenesis - Subduction and Upwelling. *J. Mar. Res.*, **51**, 497-513.

Wang, W., and R. X. Huang, 2004: Wind energy input to the Ekman layer. *J. Phys. Oceanogr.*, **34**, 1267-1275.

Watanabe, M., and T. Hibiya, 2002: Global estimates of the wind-induced energy flux to inertial motions in the surface mixed layer. *Geophys. Res. Lett.*, **29**, 1239.

Weller, R. A., A. S. Fischer, D. L. Rudnick, C. C. Eriksen, T. D. Dickey, J. Marra, C. A. Fox, and R. R.Leben, 2002: Moored observations of upper ocean response to the monsoon in the Arabian Sea during 1994–1995. *Deep-Sea Res.*, **49B**, 2195–2230.

White, W. B., 1972: Dopper shift in the frequency of inertial waves observed in moored spectra. *Deep-Sea Res.*, **19**, 595–600.

Whitt, D. B., and L. N. Thomas, 2015: Resonant generation and energetics of wind-forced near-inertial motions in a geostrophic flow. *J. Phys. Oceanogr.*, **45**, 181–208.

Wunsch, C., and R. Ferrari, 2004: Vertical mixing, energy and the general circulation of the oceans. *Annu. Rev. Fluid Mech.*, **36**, 281–314.

Wyrtki, K., L. Magaard, and J. Hager, 1976: Eddy energy in the oceans. *J. Geophys. Res.*, **81**, 2641-2646.

Yoshikawa, Y., K. Akitomo, and T. Awaji, 2001: Formation process of intermediate water in baroclinic current under cooling. *J. Geophys. Res.*, **106**, 1033-1051.

Young, W. R., and M. BenJelloul, 1997: Propagation of near-inertial oscillations through a geostrophic flow. *J. Mar. Res.*, **55**, 735-766.

Zhai, X., R. J. Greatbatch, and J. Zhao, 2005: Enhanced vertical propagation of storm-induced near-inertial energy in an eddying ocean channel model. *Geophys. Res. Lett.*, **32**, L18602.

Zhai, X. M., R. J. Greatbatch, and J. D. Kohlmann, 2008: On the seasonal variability of eddy kinetic energy in the Gulf Stream region. *Geophys. Res. Lett.*, **35**, L24609.

Zhai, X., 2015: Latitudinal dependence of wind-induced near-inertial energy. *J. Phys. Oceanogr.*, **45**, 3025-3032.

Zhang, Z. W., J. W. Tian, B. Qiu, W. Zhao, P. Chang, D. X. Wu, and X. Q. Wan, 2016: Observed 3D Structure, Generation, and Dissipation of Oceanic Mesoscale Eddies in the South China Sea. *Sci. Rep.*, **6**, 24349.

Zhong, Y. S., and A. Bracco, 2013: Submesoscale impacts on horizontal and vertical transport in the Gulf of Mexico. *J. Geophys. Res.*, **118**, 5651-5668.